University of New Hampshire
University of New Hampshire Scholars' Repository

Doctoral Dissertations | Student Scholarship

Spring 1967

ELECTRON DENSITY MEASUREMENTS IN THE LOWER IONOSPHERE BY A ROCKET BORNE RADIO PROPAGATION METHOD

LEE EDWARD LARSON

Follow this and additional works at: https://scholars.unh.edu/dissertation

Recommended Citation
LARSON, LEE EDWARD, "ELECTRON DENSITY MEASUREMENTS IN THE LOWER IONOSPHERE BY A ROCKET BORNE RADIO PROPAGATION METHOD" (1967). *Doctoral Dissertations*. 855.
https://scholars.unh.edu/dissertation/855

This Dissertation is brought to you for free and open access by the Student Scholarship at University of New Hampshire Scholars' Repository. It has been accepted for inclusion in Doctoral Dissertations by an authorized administrator of University of New Hampshire Scholars' Repository. For more information, please contact nicole.hentz@unh.edu.

This dissertation has been
microfilmed exactly as received 67-15,798

LARSON, Lee Edward, 1937-
ELECTRON DENSITY MEASUREMENTS IN THE LOWER IONOSPHERE BY A ROCKET BORNE RADIO PROPAGATION METHOD.

University of New Hampshire, Ph.D., 1967
Geophysics

University Microfilms, Inc., Ann Arbor, Michigan

ELECTRON DENSITY MEASUREMENTS IN THE LOWER IONOSPHERE BY A ROCKET BORNE RADIO PROPAGATION METHOD

By

LEE EDWARD LARSON

B.S., Bates College 1959

M.A., Dartmouth College 1961

A THESIS

Submitted to the University of New Hampshire

In Partial Fulfillment of

The Requirements for the Degree of

Doctor of Philosophy

Graduate School

Department of Physics

April, 1967

This thesis has been examined and approved.

Robert E Houston

Harry H. Hall

Edward L. Tinsley

Robert W Lambert

John Dowling, Jr.

May 5, 1967

Date

ACKNOWLEDGMENTS

The author wishes to express his sincere thanks to his adviser and good friend Dr. Robert E. Houston, Jr. for suggesting this study and providing guidance throughout its development.

Thanks are also due to Dr. J. A. Lockwood, for discussions concerning payload development and for use of the high energy charged particle data, and to Mr. L. A. Friling who was in charge of payload construction.

Computer time was provided by the University of New Hampshire and Denison University Computer Centers. Machine work was done by Mr. K. Flanders, drawings were made by Mr. H. Scheibel, and typing was done by Mrs. M. Richards and Mrs. J. Wallingford.

This work was supported by the National Aeronautics and Space Administration under Grant NASr-164.

TABLE OF CONTENTS

LIST OF TABLES

LIST OF FIGURES

CHAPTER I

INTRODUCTION

The ionosphere is the weakly ionized portion of the earth's atmosphere that extends from about 50 to over 1000 km. The primary radiation source causing the ionization is the sun, but galactic cosmic radiation is thought at present to be producing ions in the lowest part. For historical reasons, the ionosphere was divided into regions (Ratcliffe and Weekes, 1960). Before direct measurements were possible, data from ground-based ionosondes indicated that there were distinct layers of electrons in different regions, and these were named, starting at the lowest altitude, the D, E, and F layers. Results from rocket experiments show that distinct layers do not exist but that there are regions where the density of electrons changes little over a range of height; these regions are still referred to as the D, E, and F regions. The part of the ionosphere from 50 to 85 km is the D region, from 85 to 160 km the E region, and the F region is that part above 160 km.

This experiment is concerned with the D and lower E regions (50 to 100 km). The ionosphere has the following distinctive characteristics over this range of altitudes. The density of the neutral particles is fairly high (10^{16} to 10^{13} particles/cm^3) (U.S. Standard Atmosphere, 1962) which means that the collision frequency is large. Because this region is shielded from much of the sun's radiation by the atmosphere above it, and because the neutral particle density is great leading to a high rate of removal of ionization, the electron density is relatively low (a few to 10^5 electrons/cm^3) as compared with upper regions of the ionosphere.

Below 90 km mixing processes keep the relative composition of the atmosphere about the same as it is at the ground (U.S. Standard Atmosphere, 1962).

Comparatively few data from this region of the ionosphere are available. Fairly sophisticated ground-based equipment can provide some information about electron density but the data are subject to some question and hard to interpret because of the low density of electrons and high collision frequency (Ratcliffe and Weekes, 1960). This region is between the altitude which can be reached for direct measurements by balloons and satellites. Therefore at present sounding rockets provide the only means for in situ measurements. These, however, are not ideal, as they spend only a very short time (typically a maximum of 30 sec. for rockets used in this experiment) in the region of interest.

The type of experiment most useful in providing a test of current theoretical ionospheric models is one which measures simultaneously as a function of altitude the electron density and the flux of the ionizing radiation. The wavelength ranges thought to be important are 2 to 12 A. X-rays, 12 to 100 A. X-rays, 1216 A. (Lyman alpha radiation), extreme ultraviolet in the 911 to 1026 A. range and cosmic radiation (Bourdeau, 1962-63; Poppoff, Whitten and Edmonds, 1964). In this experiment detectors were flown on Nike-Apache and Nike-Tomahawk rockets to measure fluxes in the 2 to 12 A. and 1216 A. ranges. No simple detector is available which will measure the extreme ultraviolet fluxes, and reliable 12 to 100 A. detectors had not been perfected when the apparatus was built. Another experimenter on our payload measured the flux of charged particles with energies greater than 20 Mev. for protons and greater than .5 Mev. for electrons (Lockwood, 1966). These data were taken as a measure of the cosmic ray flux.

Direct electron density measurements in the D region are difficult to make, especially at the heights where the number falls below 500 electrons/cm^3. A Langmuir probe or some other form of plasma probe can be used to make this measurement. These are attractive, because they need no ground support equipment and provide a fairly detailed record of electron density. However, recent measurements show the data from probes to be subject to question below 80 km (Salah and Bowhill, 1966). The high speed of the rocket and the large number of neutral particles will likely change the plasma sheath around the probe, and therefore limit the accuracy of the theory used to derive the electron density (Heikkila, 1965). Bourdeau (1962-63) points up other problems in interpreting probe data. Two low frequency (1.005 MHz and 3.385 MHz) Faraday rotation radio propagation experiments were included in our payload to measure the electron density. Frequencies under 3 MHz have seldom been used. The sensitivity of this type of experiment is about proportional to one over the frequency of the wave squared, but the lower the frequency of the wave the more rapidly it is attenuated as it traverses the ionosphere. For conditions normally found in the ionosphere, the 3.385 MHz experiment is sensitive to a minimum of 200 to 500 electrons/cm^3, and the 1.005 MHz experiment extends the measurements down to the 20 to 50 electrons/cm^3 range. The 3.385 MHz experiment is necessary because the 1.005 MHz signal is completely absorbed below the upper part of the region of interest. These experiments require fairly bulky ground-based equipment, and since the data must be averaged over heights of about 1 km, they do not provide a finely detailed record of the electron density. The main attraction of this method is the lack of theoretical problems such as exist in the interpretation of probe data.

The central purpose of this experiment is to make reliable direct electron density measurements in the D and lower E regions using radio propagation techniques. In addition, using the radiation fluxes measured, some indication is given of how well the present ionospheric models match the observed electron densities.

CHAPTER II

THEORY OF IONOSPHERIC FORMATION

1. General Properties

When ionizing radiation from the sun penetrates the atmosphere, it encounters a greater and greater density of gas as it travels deeper into the atmosphere, and therefore produces a higher and higher number of free electrons. As it produces electrons, it gets absorbed at a greater and greater rate; when the rate of radiation absorption surpasses the rate of increase of the atmospheric density, then the production of electrons decreases at points farther down in the atmosphere. The electrons formed eventually undergo a loss process. These two basic concepts determine the distribution of electrons in the ionosphere. The rate of change of the electron density is

$$\frac{dN_e}{dt} = q - L \qquad (1)$$

N_e = electron density
q = rate of production
L = rate of loss

This chapter will serve to make these basic ideas more quantitative, and will discuss specific physical processes thought to be important in the D and lower E regions.

2. Electron Production

The most commonly used equation for electron production was first developed by Chapman (1931). The following derivation of this equation is based on a discussion by Davies (1965). Assume

(a) the ionizing radiation is monochromatic.

(b) a horizontally stratified atmosphere.

(c) only one kind of gas being ionized.

At the top of the atmosphere the parallel flux of monochromatic radiation is S_∞ ; it is incident at zenith angle χ (angle from the zenith to the sun). Let S be the flux at altitude h, and S + dS the flux at h + dh. Then, in a cylinder of unit cross-section, the energy absorbed is

$$dS = S \sigma_a N_a dh \sec \chi \qquad (2)$$

where σ_a is the total absorption cross-section of the molecules and N_a is the number of absorbing molecules per unit volume. Integrate

$$\int_{S_\infty}^{S} \frac{dS}{S} = \sec \chi \int_{\infty}^{h} N_a \sigma_a \, dh$$

$$S = S_\infty \exp (- \tau \sec \chi) \qquad (3)$$

$\tau = -\int_{\infty}^{h} N_a \sigma_a \, dh$ is the optical depth of the atmosphere down to altitude h. The energy absorbed per unit volume is the energy absorbed per unit length in the cylinder. From (2)

$$\frac{dS}{dh \sec \chi} = N_a \sigma_a S \, .$$

If η is the ionization efficiency (number of ion pairs produced per unit energy absorbed), then the number of ion pairs produced per volume per second is

$$q(\chi,h) = N_i \sigma_i \eta S \tag{4}$$

or, using (3),

$$q(\chi,h) = N_i \sigma_i \eta S_\infty \exp(-\tau \sec \chi) \tag{5}$$

where N_i = number density of the constituent being ionized and σ_i is the absorption cross-section of this constituent.

Look more closely at τ.

$$\tau = -\sigma_a \int_\infty^h N_a \, dh$$

The pressure of the gas is

$$dp = -\rho g \, dh$$

$$dp = -N m g \, dh.$$

If the dependence of g on altitude is ignored,

$$\tau = \frac{\sigma_a}{mg} \int dp$$

$$\tau = \frac{\sigma_a p}{mg} \tag{5a}$$

But $p = N_a kT$.

$$\tau = \frac{\sigma_a N_a kT}{mg}$$

Define $\frac{kT}{mg} = H$ = scale height. Then

$$\tau = \sigma_a N_a H. \tag{6}$$

This relates τ to better known quantities. If the value of g at the earth's surface is used, the calculation underestimates τ; elementary considerations show that the error is less than 3 per cent under 100 km (Van Zandt and Knecht, 1964).

In practice, if the radiation flux as a function of altitude is known, (4) can be used to calculate the rate of production. Otherwise (5) is the working equation. One type of complicated situation arises when the absorbing gas is not the one being ionized (Ratcliffe and Weekes, 1960). For example, in the D region, the Lyman alpha line is absorbed mainly by O_2, but is ionizing only the trace constituent NO. Therefore the optical depth τ is dependent on the O_2 absorption cross-section and density, whereas the amount of ionization depends on the ionization cross-section and density of NO. This example shows that it is extremely useful to measure the flux of important ionizing radiation as a function of altitude. About half the variables needed to calculate the production functions are eliminated by this measurement, which allows (4) to be used for the calculations.

The earth's atmospheric layers are not flat, but spherical due to the curvature of the earth. To take this factor into account, sec χ in the above equations is replaced by Ch (χ), the Chapman angle function, which has been tabulated by Wilkes (1954). For $\chi < 75^{\circ}$, which is the case for all of this work, negligible error is made by retaining sec χ in the equations (Ratcliffe and Weekes, 1960).

If several ionizing processes are occurring simultaneously, q for each process can be calculated, and these are added to give the total rate of production.

3. Electron Losses

Electrons are lost from the ionosphere by two main processes. (a) They reunite with positive ions. (b) They attach to neutral molecules to form negative ions. Electrons are also lost from a given volume by ionic drift and diffusion processes; these will be neglected as they are unimportant below 150 km (Whitten and Poppoff, 1965). Let the number density of electrons, positive ions, negative ions and neutral particles be N_e, N_A, N^-, and N respectively. Then, the rate of electron removal by recombination is

$$\frac{d\,N_e}{dt} = -\alpha_D\, N_e\, N_A\,.$$

α_D is the election-ion recombination coefficient. If not many negative ions are formed, and we assume electrical neutrality, $N_e \approx N_A$, and

$$\frac{d\,N_e}{dt} = -\alpha_D\, N_e^{\,2}. \tag{7}$$

The rate of electron loss by attachment is

$$\frac{d\,N_e}{dt} = -b\, N_e\, N.$$

If $N >> N_e$, then N changes very little when electrons are produced. Letting $b\,N = \beta$,

$$\frac{d\,N_e}{dt} = -\beta\, N_e \tag{8}$$

where β is the attachment coefficient. Therefore, the rate of change of

electrons is

$$\frac{d N_e}{dt} = q - \alpha_D N_e^2 \tag{9a}$$

when recombination is the dominant loss process or

$$\frac{d N_e}{dt} = q - \beta N_e \tag{9b}$$

when the attachment process is most important. If we assume that the number of electrons is changing slowly with time $\frac{d N_e}{dt} \approx 0$ (quasi-equilibrium) then

$$N_e = \sqrt{\frac{q}{\alpha_D}} \tag{10a}$$

$$N_e = \frac{q}{\beta} \tag{10b}$$

depending on the dominating loss process.

Electrons are detached from negative ions by two processes; collisional detachment and photodetachment. The processes effectively produce electrons, and for them,

$$\frac{d N_e}{dt} = + \gamma N^- N \qquad \frac{d N_e}{dt} = + \rho N^-$$

where γ and ρ are the collisional detachment and photodetachment coefficients. If all these effects are included we can write

$$\frac{d N_e}{dt} = q - \alpha_D N_e N_A - \beta N_e + \gamma N^- N + \rho N^- \tag{11}$$

To simplify this equation, we proceed as follows. The rate of change of negative ion density is

$$\frac{d N^-}{dt} = - \alpha_i N^- N_A + \beta N_e - \gamma N^- N - \rho N^- \qquad (12)$$

where α_i is the ion-ion recombination coefficient. We assume the ionosphere is electrically neutral ($N_A = N_e + N^-$) and define $N^-/N_e = \lambda$. Solve (12) for $\gamma N^- N$ and ρN^- and insert it into (11).

$$\frac{d N_e}{dt} = q - \alpha_D N_e N_A - \alpha_i N^- N_A - \frac{d N^-}{dt}$$

$$\frac{d N_e}{dt} = q - (\alpha_D - \lambda \alpha_i) N_e N_A - \frac{d N^-}{dt}$$

since $\frac{d N^-}{dt} = \lambda \frac{d N_e}{dt} + N_e \frac{d \lambda}{dt}$

$$(1 + \lambda) \frac{d N_e}{dt} = q - (\alpha_D + \lambda \alpha_i) N_e N_A - N_e \frac{d \lambda}{dt}$$

$$\frac{d N_e}{dt} = \frac{q}{1 + \lambda} - (\alpha_D + \lambda \alpha_i) N_e^2 - \frac{N_e}{1 + \lambda} \frac{d \lambda}{dt}$$

If $\frac{d \lambda}{dt} \to 0$, then

$$\frac{d N_e}{dt} = q_{eff} - \alpha_{eff} N_e^2 \qquad (13)$$

which is of the same form as (9a) suggesting that the net effect of the electron loss processes is to appear as recombination. Then, for calculating the electron density under quasi-equilibrium conditions,

$$N_e = \sqrt{\frac{q_{eff}}{\alpha_{eff}}} \qquad \text{or}$$

$$N_e = \sqrt{\frac{q}{(1 + \lambda) (\alpha_D + \lambda \alpha_i)}} \qquad (14)$$

This is the working equation for calculating the electron density in the lower ionosphere. Recall that q is calculated using (4) or (5). It should be noted that if $\lambda \to 0$ that (14) is identical to (10a). Values of α_{eff} in the D region are not well known; in fact the order of magnitude is still subject to some debate (Aikin and Kane, 1964; Poppoff, Whitten and Edmonds, 1964; Donahue, 1966). It is the net effect of all the recombination coefficients of all the gases involved, and is very difficult to measure (Whitten, et al, 1965a). α_D is also temperature dependent, but the nature of this dependence is subject to question and is given by Whitten and Poppoff (1965) as T^{-n} where $1/2 \leq n \leq 3/2$. Calculations done in this paper will follow Donahue (1966) and assume a $T^{-3/2}$ dependence. It is generally concluded that λ approaches zero at altitudes above 75 km, but its value as a function of altitude in the lower D region is at present somewhat uncertain. Representative recent values (Reid, 1964; Sagalyn and Smiddy, 1964; Nicolet and Aikin, 1960; Poppoff, Whitten and Edmonds, 1964) set λ between 5 and 12 at 60 km, 1.5 and 8 at 65 km, .6 and 3 at 70 km, and .1 and .7 at 75 km.

In summary, the wavelengths of light that arrive at a given depth in the atmosphere depend on the absorption cross-section and density of molecules above this altitude. Then, the intensity of radiation present coupled with the density of each type of molecule, its absorption cross-section and ionization efficiency determine the production rate at each height for each molecular species. Ions are continually destroyed, and the balance between the production and recombination rates determines the final electron density as expressed by (14).

4. Chapman Layer

An early successful model for the formation of an ionospheric layer is due to Chapman (1931). The development here again follows Davies (1965). We use the results from part 2 of this chapter, and in addition require:

(d) one kind of gas present.

(e) an isothermal atmosphere.

Then, (5) and (6) become

$$q\ (\chi,\ h) = N\ \sigma\ S_\infty \exp\ (-\ \tau \sec\ \chi)$$

$$\tau = \sigma N\ H$$

where H is constant. From the second of these,

$$N = \frac{\tau}{\sigma H}\ .$$

Therefore,

$$q\ (\chi,\ h) = \frac{\tau\ \eta\ S_\infty}{H\ e} \exp\ (1\ -\ \tau \sec\ \chi)$$

where e = base of natural logarithms.

Some interesting conclusions may be drawn by making the following substitutions.

Define $z = -\ln \tau$ so $\tau = \exp\ (-z)$.

The last expression becomes

$$q\ (\chi,\ z) = \frac{S_\infty}{H\ e} \exp\ [1\ -\ z\ -\ \sec\ \chi \exp\ (-z)]$$

$$q\ (\chi,\ z) = q_o \exp\ [1\ -\ z\ -\ \sec\ \chi \exp\ (-z)]$$

where $q_o = \frac{\eta S_\infty}{H e}$. q_o physically is the rate of production for an overhead sun (sec χ = 1) when z = 0. z is a normalized height which is zero at the altitude of maximum production when the sun is overhead. Rewrite this expression when χ = 0:

$$q\ (0,\ z) = q_o \exp\ [1 - z - \exp\ (-z)]$$

Replace z by $z' - \ln \sec \chi$.

$$q(0,\ z' - \ln \sec \chi) = q_o \exp\ [1 - z' + \ln \sec \chi - \exp\ (-z' + \ln \sec \chi)]$$

$$q\ (0,\ z) = q_o \sec \chi \exp\ [1 - z' - \sec \chi \exp\ (-z')]$$

$$q\ (0,\ z) = \sec \chi\ q\ (\chi,\ z')$$

Note that q (χ, z') has the same shape as q (0, z); it is moved up in altitude by an amount ln sec χ, and is smaller by an amount cos χ. The height of maximum production occurs when

$$z' - \ln \sec \chi = 0$$

$$z_m = \ln \sec \chi.$$

The maximum rate of production is found by putting this value into the equation for q (χ, z).

$$q_m\ (\chi,\ z) = q_o \exp\ [1 - \ln \sec \chi - \sec \chi \exp\ (-\ln \sec \chi)]$$

$$q_m = q_o \cos \chi$$

This shows that the altitude of maximum production is independent of the magnitude of the incoming flux, and that q_m depends only on

the factors making up q_o and the zenith angle.

q (χ, z) is now inserted into (14) to find the electron density distribution under quasi-equilibrium conditions. If λ is small,

$$N_e = \frac{q_o}{\alpha}^{1/2} \exp 1/2 \left[1 - z - \sec \chi \exp (-z)\right] \tag{15}$$

Since the maximum rate of production is $q_o \cos \chi$,

$$(N_e)_{MAX} = \frac{q_o}{\alpha}^{1/2} (\cos \chi)^{1/2} \tag{16}$$

It should be noted that the maximum electron densities in the E and F layers do, in fact, tend to depend on $(\cos \chi)^{1/2}$. Using (15), we see that near the bottom of the layer where z is negative making the third term in the exponent important, the electron density depends strongly on the zenith angle. Near the top of the layer, where z is positive, the second term in the exponent is dominant except near sunrise and sunset; therefore, except at these times the electron density at these altitudes stays relatively constant.

This derivation is the basis for nearly all theoretical models being developed today. Houston (1957) shows how all the assumptions needed in this derivation can be eliminated.

5. D Region

This section is an attempt to summarize present knowledge concerning physical processes which are important in the daytime D region at mid-latitudes. The wavelengths and respective intensities of flux that penetrate the atmosphere to this level, the resulting ion species formed, and the relative importance of the mechanisms by which

electrons disappear will be discussed.

It should be emphasized that this section and the next are concerned mostly with an undisturbed ionosphere. The only disturbances discussed are those which pertain to our present work.

From 3000 to 1 A. there are only three spectral regions that penetrate to the D region; 1-12A., narrow bands about 1216, 1187, 1167, 1157, 1143 and 1108 A., and 1800-3000 A. The radiation from 1026.5 A. (first ionization potential of O_2) to 1800 A. is absorbed above 85 km by O_2, which has a relatively high absorption cross-section (10^{-19} cm^2) except at the "windows" noted above where the cross-section drops markedly. The ionizing radiations of N_2 and O_2 (12 to 1026.5 A) are absorbed by the combination of high cross-sections and large concentrations of these gases in the upper ionospheric regions.

The radiation from 1800-3000 A. penetrates the D region and is absorbed below 40 km by O_3. The only constituents which have threshold wavelengths low enough to be ionized by this band are the alkali metals sodium ($\lambda \leq$ 2410A.), calcium ($\lambda \leq$ 2060A.) and potassium ($\lambda \leq$ 2860 A.). It is felt that the concentration of these elements in the D region is very small and consequently the density of electrons which results from their ionization is negligible (Reid, 1964).

Therefore, any ions due to solar radiation are formed by fluxes from 1 to 12 A. and in the windows from 1108 to 1216 A. The following flux levels are all from Friedman (1963) unless otherwise noted. The flux in the 1 to 12 A. X-ray region depends strongly on the condition of the sun. At the top of the atmosphere for a quiet sun, there are 10^{-8} erg/cm^2 sec. in a 2 A. bandwidth about 2 A., increasing to 10^{-4} erg/cm^2 sec. about 12 A. However, when the sun is highly disturbed

(class 2+ flare), these levels can rise by a factor as high as 10^5 and they change by a factor of 10^2 between solar minimum and maximum. The radiation at only one of the windows is intense enough to be important. The window at 1216A. very nearly coincides with the intense hydrogen Lyman α line. At the top of the atmosphere its intensity is between 4.4 and 5.1 erg/cm^{2}sec. (Friedman, 1963; Hinterreger, Hall, Schmidtke, 1965) and it is found that this value is nearly independent of solar activity.

The only atmospheric constituent which can be ionized by Lyman α is the trace molecule NO. It is formed in the ionosphere principally by the reaction

$$N + O_2 \rightarrow NO + O$$

and is destroyed by

$$N + NO \rightarrow N_2 + O$$

The concentration of NO at D region heights was measured most recently by Barth (1966) who gives $n(NO) = 4 \times 10^7$ molecules/cm^3. Because of the difficulty of the measurement and some of the assumptions made, and because this result is an order of magnitude larger than was expected by most experimenters it is subject to some question at this time (Whitten and Poppoff, 1965). Also Aikin, Kane, and Troim (1964) point out that the NO concentration should be proportional to the ratio of the reaction rates for the formation and destruction processes above. There is a discrepancy of 10^2 between a laboratory measurement of this ratio and the ratio derived using Barth's measurement for the concentration of NO. It will be shown in this work that using a concentration which is a factor of 2.5 less than Barth's result yields a value for the electron density

which agrees with experiment. The absorption cross-section and ionization efficiency for Lyman α acting on NO have been measured by Watanabe (1954) and have respective values of 2.4×10^{-18} cm^2 and .81. This large cross-section and the high intensity of ionizing radiation mean that a relatively high percentage of the NO present will be ionized and the process is sifficient to account for the bulk of the quiet D region (Nicolet and Aikin, 1960). It should be noted that the absorption of Lyman α is mainly due to its interaction with O_2; the concentration of NO is so low that it does not produce a measurable attenuation of the radiation.

The 1 to 12 A. X-rays have about the same ionization cross-sections for all of the major atmospheric constituents, and its value ranges from 2×10^{-21} cm^2 at 2 A. to 7.5×10^{-20} cm^2 at 12 A. (Hinterreger, Hall, Schmidtke, 1965). With quiet sun flux levels most workers feel that ion production by the X-rays is unimportant (Reid, 1964; Bourdeau, 1962-63) but calculations have been made by Poppoff, Whitten and Edmonds (1964) which show they may be important even at quiet sun times. It is generally believed that the great increase in electron production of the D region at mid-latitudes during a solar flare is caused by the enhancement of this short wavelength X-ray flux which takes place under these conditions. At these times the X-ray flux may be important in producing electrons at altitudes well below 70 km.

A non solar radiation source, galactic cosmic radiation, is thought to produce electrons in the lowest D region, below 70 km. Moler (1960), Nicolet and Aikin (1960) and Webber (1962) have made calculations which show that the production is proportional to the

neutral particle density. Since the cosmic ray flux does not vary more than a factor of two between solar minimum and maximum, the electron production due to it is fairly constant.

It is seen from (14) that if λ is known, then to determine the value for the effective recombination coefficient we need to know α_D and α_i, the dissociation and ion-ion recombination coefficients. In the D region the value of α_D for NO^+ is most important if this is the dominant positive ion. Recent literature reports values ranging from 4×10^{-8} cm^3/sec. (Aikin and Kane, 1964) to 1.6×10^{-6} cm^3/sec. (Gunton and Shaw, 1965) for temperatures present in the D region. Donahue (1966) summarizes the values of α_D for NO^+ measured by several experimenters; he concludes that the value of Gunton and Shaw is most nearly correct, and this value will be adopted here. Under disturbed sun conditions, concentrations of O_2^+ and N_2^+ will be large enough to be important. Measured values show that $\alpha_D\ (N_2+) \approx \alpha_D\ (O_2+) \approx 1$ to 3×10^{-7} cm^3/sec. (Whitten and Poppoff, 1965). O_2^- is the dominant negative ion in the D region; Whitten and Poppoff (1965) report a value of α_i for this ion measured by Van Lint and Wyatt as $\alpha_i\ (O_2^-) = 4 \times 10^{-9}$ cm^3/sec. If this value is assumed, it is seen that ion-ion recombination is unimportant above 60 km.

Representative values of the quiet sun daytime electron density for the D and lower E regions are shown in Figure 1. Of course many factors determine this profile and it can vary widely from that shown. To summarize present thinking, the electrons present below 70 km are caused by galactic cosmic radiation during quiet sun times. Above 70 km under quiet sun conditions most of the electrons are caused by hydrogen Lyman α radiation acting on nitric oxide. The importance of 1 to 12 A.

X-rays during quiet sun times is still open to debate, however. Under disturbed sun conditions, when the electron density and X-ray flux increase sharply and the Lyman α flux stays relatively constant, these X-rays take over as the more important ionizing source; also at this time they produce electrons in a region extending well below 70 km.

Before more decisive conclusions about the formation of the D region can be drawn, more measurements need to be made. To increase the confidence in future computations the nitric oxide concentration and dissociation recombination coefficient need to be better known. Then experiments such as the one reported here, which measure simultaneously the Lyman α and 1-12 A. fluxes and the low values of electron density, could help to give more definitive answers.

6. E Region

The radiation bands absorbed in the E region are 12 to 100 A. X-rays and ultraviolet light in the range 911 to 1027 A. As it is in the D region, the intensity of the ultraviolet radiation is nearly independent of solar activity. There are two important ultraviolet lines present, C_{III}(977 A.) and Lyman β (1025.7 A.) with fluxes of .05 to .08 erg/cm^2 sec. and .045 to .06 erg/cm^2 sec. respectively (Friedman, 1963; Hinterreger, Hall, Schmidtke, 1964). In the continuum from 911 to 980 A., the flux is .048 to .082 erg/cm^2 sec., excluding the C_{III} line. In the 12 to 100 A. X-ray band the flux is .51 erg/cm^2 sec. at quiet sun times (Hinterreger, Hall, Schmidtke, 1964). During solar flares the flux increases to a maximum of about seven or eight times the quiet sun levels (Friedman, 1963).

The major constituents present in the E region are N_2, O_2, and O. Oxygen molecules are dissociated into atomic oxygen by the Schumann

continuum (1350 to 1800 A.). Results by Schaefer and Nichols (1964) show the concentration of O to be small under 117 km. O_2 is the only constituent which can be ionized by the ultraviolet radiation present here; Hinterreger, Hall, Schmidtke (1964) give the absorption cross section as 1.6×10^{-18} to 7.4×10^{-18} cm^2 with an ionization efficiency of about 55 to 65 percent. All constituents are ionized by the X-rays, and the absorption cross-section, which has roughly the same value for all three, has a value the order of $.1 \times 10^{-18}$ to 1×10^{-18} cm^2. Since the concentration of O is small in the lower E region, the contribution due to this constituent at these altitudes is not important.

Mass spectrometer measurements show that the dominant ions in the E region are O_2^+ and NO^+ (Aikin and Bauer, 1965). This is surprising since calculations show that a large number of N_2 molecules should be ionized. It is thought now that besides the dissociation loss process, the N_2^+ ions are lost by these reactions (Aikin and Bauer, 1965; Bourdeau, Aikin and Donley, 1966).

$$N_2^+ + O_2 \rightarrow O_2^+ + N_2$$

$$N_2^+ + O \rightarrow N_2 + O^+$$

$$N_2^+ + O \rightarrow NO^+ + N$$

Also, the concentrations of O_2^+ and NO^+ may be enhanced by

$$O^+ + N_2 \rightarrow NO^+ + N$$

$$O^+ + O_2 \rightarrow O_2^+ + O$$

$$O_2^+ + N_2 \rightarrow NO^+ + NO$$

The importance of these reactions has not been completely determined. Bourdeau, Aikin and Donley (1966), on the basis of some measured reaction rates, and assuming that electrons are lost mainly by dissociative recombination of NO^+ and O_2^+, develop a model for solar minimum which agrees with the experimental measurement of the O_2^+ and NO^+ concentrations.

The E region is formed by two complementary processes. The first is the ionization of all constituents by the soft X-rays. In the second, O_2 is ionized by Lyman β, C_{III}, and the continuum from 911 to 980 A. In addition there may be a contribution by the Lyman continuum (850 to 911 A.) acting on molecular and atomic oxygen. The relative importance of X-rays vs. ultraviolet radiation in forming this region has not been resolved. Houston (1957) has made calculations which imply that the X-rays are primarily responsible for ionizing the bulk of the E region, and that the shape of the lower edge is dependent on Lyman β. Recent calculations by Bourdeau, Aikin and Donley (1966) reach the same conclusions above 93 km, but show that the contribution in the 88 to 93 km region due to 33.7 A. X radiation may be important.

The concentrations of the constituents, reaction rates for the processes noted above, and recombination coefficients need to be better known. It would then be desirable to measure simultaneously as a function of altitude the electron density, 12 to 100 A. flux, and appropriate ultraviolet flux. Unfortunately the flux measurements are hard to make. No simple detector for ultraviolet light with a wavelength shorter than 1050 A. has been developed, and X-ray detectors in the 12 to 100 A. range exist, but have a lifetime of only a week or two, which makes their use very difficult.

Variations in the electron densities during solar flares are caused by the increased X-ray flux. The enhancement of this region is not nearly as large as that of the D region; it is not common for the electron density in the E region to increase more than a factor of 2.5 or 3 as the result of a solar flare.

CHAPTER III

INSTRUMENTATION

1. Electron Density Experiment

All electron density measurements made by radio propagation techniques rely on observing changes in a radio wave as it passes through the ionosphere. If a plane polarized wave traverses a portion of the ionosphere, its plane of polarization changes and the wave is attenuated by amounts which depend on the wave frequency, the number density of electrons, the electron collision frequency and electron gyrofrequency. Several ways of recording and employing these two changes have been used to determine electron density (Salah and Bowhill, 1966; Aikin, Kane, Troim, 1964; Jackson and Seddon, 1958). Our method, which is similar to that of Aikin, Kane, and Troim, consisted of two ground-based transmitters operating at 1.005 and 3.385 MHz which sent signals to receivers located in the payload. As the rocket penetrated the ionosphere, the receivers recorded the continual change in the plane of polarization of the signal.

a. Transmitters. The 3.385 MHz transmitter consisted of a Gates HFL-1000 linear amplifier driven by a specially designed exciter (Figure 2). The antenna was a standard half-wave linear dipole and the power output was 1000 watts. The 1.005 MHz transmitter was made up of a Heathkit Warrior linear amplifier and a Millen 90801 exciter, both modified to operate at this low frequency. Since a half-wave linear dipole at this frequency is an unwieldy 468 feet in length, 6 loading coils were installed in a 120 foot long antenna and tuned so that the antenna resonated at the proper frequency. This operation greatly

reduced the impedance of the antenna; to match it to the transmitter, the coaxial cable from the transmitter to the antenna was made (2 n-1)/4 wavelengths in length so that it would act as a matching transformer (Radio Amateur's Handbook, 1966). This unit was capable of a power output of 400 watts. Both transmitters broadcasted a CW (unmodulated) signal whose frequency was crystal controlled.

b. Receiver Design. The 1.005 and 3.385 MHz receivers, which were designed by F. Szachta (1965), were identical except for the antenna wiring, the local oscillator crystal and a capacitor in the R. F. tuning section. The qualities essential in a receiver for this work are reliability, selectivity, stability, sensitivity, and compactness. A block diagram is shown in Figure 3. Figures 4A and 4B illustrate the complete circuit diagram and Figure 5 is a photograph of a completed unit (less the antenna).

The antenna was formed on a cylindrical ferrite rod 5/8 by 5 1/2 inches. The tuning network consisted of a coil of heavy wire wound on the rod in parallel with two capacitors whose values were selected so that the antenna would resonate at the proper frequency. One of these capacitors had a fixed value and the other was a variable trimmer which allowed small adjustments in the resonant frequency. Coupling to the R. F. stage was accomplished by a second coil wound around the rod. The antennas for both receivers were then mounted at right angles two inches apart on a single fiberglass deck plate, and the entire unit was encapsulated (Eccofoam F.P.; Emerson and Cuming, Inc.; Canton, Massachusetts) to add strength and to keep wires from flexing or moving.

The R. F. amplifier was a standard common emitter class A tuned amplifier. The local oscillator and mixer were combined to save one stage. A crystal controlled Colpitts oscillator was used to provide

frequency stability, and its circuit parameters were chosen so that it would oscillate equally well at either frequency with just a change of crystal. To insure that no self-oscillations at the I.F. frequency would develop, a crystal filter was installed in the base circuit which effectively grounded it at the I.F. frequency. Another identical crystal filter was placed in parallel with the emitter circuit of the oscillator-mixer. This added the desirable quality of an increase in the gain of the stage at this one frequency only.

The three I.F. sections were identical, and each used a transfilter for the frequency selection element. The transfilter, which takes the place of the more commonly used I.F. transformer, is a ceramic disk with three contacts which is designed to match a high input impedance and low output impedance, and to have narrow band-pass characteristics (about 3 KHz here). It has a Q of 140 as used in this circuit (Szachta, 1965). The resonant frequency of a transfilter is not adjustable, which is a desirable feature as there is no setting to be altered by vibrations during flight. However, this feature led to a problem. It was found that the capacitive component in the input and output impedances to the transfilter and inter-electrode capacitance altered the resonant frequency by as much as 3 KHz. Therefore the frequency of best response for each completed receiver had to be measured and a corresponding transmitting crystal was used during the flight. This frequency calibration of the receivers is fully described in the next section. In each I.F. stage a crystal filter was installed in the emitter circuit, which improved the gain at the I.F. frequency in the same way that it did in the oscillator-mixer.

Detection was done by a germanium diode, and the resulting signal was sent to the audio amplifier. The modulation of the input is due

primarily to the spin of the rocket about its longitudinal axis, with a small perturbation added by the effect of the ionosphere. Since the spin rate of the rocket is normally between 3 and 10 cycles/sec., the audio amplifier was designed to operate at frequencies in this low range. A zener diode across the output limited the output voltage to 5 Volts (a telemetry requirement).

The automatic gain control (A.G.C.) was included so that the sensitivity of the receiver was adjusted as the signal strength changed. This prevented the receiver from overloading when the signal was strong and assured adequate sensitivity when the signal was weak. The circuit consisted of a feedback network which changed the biassing of the R.F. and the first I.F. stages such that their gain was reduced when a large input signal to the receiver was present. The time constant of the A.G.C. circuit should be long compared to the period of the slowest modulation expected so that a modulated signal is not "misinterpreted" as a signal strength change. The time constant of this A.G.C. circuit was about two seconds which satisfied the requirement.

The completed receivers had a bandwidth of 2.2 KHz and the center frequency was stable within 60 Hz during a 1 hour test (Szachta, 1965). Also, the center frequency was found to vary less than 300 Hz over a temperature range of -10 to +50 degrees Centigrade. To test the sensitivity, the following method was employed since no calibrated antenna was available. A one turn link loosely coupled to the antenna and connected to the R.F. signal generator was used to provide an input. A 1 microvolt signal from the generator resulted in an output signal which was easily distinguished from the background noise, and with a 5 microvolt input signal, the output was close to its maximum value of 5 volts.

c. Receiver Construction, Testing and Calibration. The layout, building, packaging and testing of the receivers was done primarily by the author. A printed circuit layout was used to add reliability to the finished receivers and to facilitate construction. The use of circuit boards with both sides copper plated allowed a grounded conducting sheet to be placed between the circuit and the components as insurance against oscillations. Receivers were all encapsulated with Eccofoam before flight so that components would be held firmly in position.

A test of a receiver's sensitivity was the only one needed to assure that it was operating properly. Tests were performed using the one turn link described in the last section and an R.F. signal which was amplitude modulated at 7 cycles/sec. to simulate the flight signal. On each receiver, after the R.F. coil and antenna trimmer were adjusted properly, a 1 microvolt input signal was easily seen at the output above the background noise. The operation of the A.G.C. was verified by increasing the input signal to 10 millivolts and finding no appreciable distortion in the output.

No calibration of the receivers was needed. This is because the receiver signal is maximum when its dipole antenna is exactly lined up with the plane of polarization of the wave; the angular positions of the antenna at maximum signal with respect to an arbitrary reference point are the only data needed.

Because the receivers had a very narrow bandwidth and an uncertain center frequency, the frequency broadcast by the transmitter during flight had to be carefully chosen. The frequency of best response for each receiver was measured, and the transmitter frequency was matched to this value within .5 KHz. For this measurement the receiver input signal

was provided by a modulated variable frequency R.F. signal generator connected to a frequency counter. The frequency of the oscillator was altered until the receiver signal maximized and then the center frequency was recorded from the counter.

2. Ultraviolet Flux Measurements

The ultraviolet flux was measured with a photoionization chamber which is an instrument made up of a ceramic cylinder that has a transparent window on one end and is filled with a gas which can be ionized by the radiation of interest. The ions formed in the chamber were swept out by a modest voltage applied between a center electrode and a conducting coating on the cylindrical wall. The resulting current was sent to circuitry which transformed this signal into one suitable for transmission to the ground by the telemetry system. The ionization chambers and the electronics will be discussed separately.

a. Electronics. The current from an ion chamber ranges up to 5×10^{-9} amperes, depends on the design and efficiency of the chamber, and is proportional to the radiation flux. To measure small flux levels it was desirable to have the electronics sensitive to currents as small as 10^{-11} amperes. These values set the input requirements for the circuitry. The output ranged from 0 to +5 Volts to match the requirements imposed by the telemetry system. Simplified and complete circuit diagrams of the electronics are illustrated in Figures 6 and 7 respectively and Figure 8 is a photograph of this instrumentation.

The description of this circuitry, which was designed by the author, follows Malmstadt, Enke, and Toren (1963). The first stage is known as a transresistor and is made up of a very high input impedance

operational amplifier with a feedback resistor R_1 as shown in Figure 6. If the gain of the amplifier is A,

$$e_{out\ 1} = -A\ e_{in\ 1} \quad .$$

Also, $$i_1 = \frac{e_{in\ 1} - e_{out\ 1}}{R_1}$$

$$i_1 = \frac{-e_{out\ 1}\ (1 + A)}{R_1\ A} \quad .$$

If the input impedance of the amplifier is much larger than the feedback resistance, then $i_{in} \approx i_1$; if $A >> 1$,

$$e_{out\ 1} = i_{in}\ R_1 \ . \tag{17}$$

The input impedance of this first stage is

$$R_{in} = \frac{e_{in\ 1}}{i_{in}} = \frac{e_{in\ 1}\ R_1\ A}{e_{out\ 1}(1 + A)} = \frac{R_1}{1 + A} \quad .$$

$$R_{in} \approx \frac{R_1}{A} \text{ if } A >> 1.$$

Then the voltage developed across the input is

$$e_{in\ 1} = \frac{i_{in}\ R_1}{A} \quad .$$

This type of circuit is good for current measuring applications for the following reason. The input impedance is much smaller than either the feedback resistance or the amplifier input impedance. As a result, the voltage developed across the input is very low; this is required so

that the circuit being used does not have much effect on the magnitude of the current being measured. With a maximum input of 5×10^{-9} amperes, the voltage across the input of the transresistor stage built was the order of 10^{-4} volts.

As is seen by (17) the output voltage is just the product of the input current and the feedback resistance, and is inverted. The input was positive and therefore the output of the first stage was negative. Since the telemetry system accepted only a positive voltage, a unity gain phase inverter was used as the next stage. The output of this stage went to the telemetry and also to the third stage which was a gain of 26 voltage amplifier.

In the final circuit R_1 was a 5 percent resistor with a value of 10^9 ohms. With the input current equal to 10^{-11} amperes, the high gain output was .26 Volts; the maximum output level of 5 Volts was reached when the current input was $.2 \times 10^{-9}$ amperes. For currents between $.2 \times 10^{-9}$ and 5×10^{-9} amperes, the low gain output ranged between .2 and 5 Volts. Therefore it is seen that by making R_1 this value, and by including the gain of 26 amplifier as a third stage, currents at any point in the desired range could be measured with reasonable accuracy.

For an operational amplifier whose input impedance was greater than 10^9 ohms, a Philbrick PP25A was selected. It uses field effect transistors at the input, has an input impedance of 10^{11} ohms and a minimum gain of 8×10^4. Since the requirements of the second and third stages were less stringent, the less expensive Philbrick PP65AU amplifiers were adequate.

Frequency response of this electronics presented no problem. Since the ion chambers provided an input current only while they were pointed at the sun, and the rocket spun at a three to ten cycle/sec

rate, the input was much like a half-wave rectified A.C. signal at this frequency. Response at high frequencies was not needed, and to limit it and thereby make the circuit less susceptible to high frequency oscillations a capacitor was placed in parallel with each feedback resistor.

The only other pertinent additions to the basic circuit were crossed diodes across the input of each operational amplifier to protect it against overloads (Philbrick Researches Engineering Staff, 1966), 5 Volt zener diodes across the low and high gain outputs to limit the outputs to this value and a calibration system to be described below.

b. Calibration and Construction of Electronics. For the ultraviolet deck, the validity of the results was determined by how well the magnitude of the output voltage was known. To calibrate the entire system including tememetry and to check its performance, a known current source was connected to the electronics input for a short time during the early part of the flight and the resulting outputs were recorded. This calibration current was generated by using a relay to connect a regulated D.C. potential of 5 Volts across one end of a 10^9 ohm resistor and by connecting the other end of the resistor to the transresistor input. The low gain output then should have read 5 Volts while the relay was energized. During calibration the high gain output was disconnected from the telemetry by the relay and the 5 Volt calibration source was substituted in its place. This gave a check on the voltage used and calibrated this channel of the telemetry system. A check on calibration of the high gain channel was made from the data by comparing it with the low gain channel during the times when the readings from both channels were valid.

Printed circuit construction was also used for this experiment. To save space, the electronics was split into two sections, one on either side of the ion chamber housing, as shown in Figure 8. The small can in the foreground contained the transresistor and the larger can housed the phase inverter, high gain amplifier and the calibration system. All parts of this unit were "foamed" before flight.

c. Ionization Chambers. The ionization chambers used here are sensitive to a narrow wavelength band in the ultraviolet region and give an output current which is directly proportional to the intensity of the radiation in this band. A sample chamber is pictured in the foreground of Figure 9.

The bandwidth is determined by selecting a window whose transmission properties provide the low wavelength cutoff and using a filling gas which is not ionized by a wavelength longer than the desired upper cutoff. Friedman (1960) lists a large number of possible windows and gases and their respective characteristics.

One type of ion chamber used in this experiment has a LiF window and a filling gas of NO which gives it a spectral response of 1050 to 1350 A. Since about 80 per cent of the flux over its response range is Lyman α radiation (Hinterreger, Hall, Schmidtke, 1965), this chamber is effectively a detector for this one line. Thus its detailed response is not important. The other type of chamber has a response of 1350 to 1550 A. shown in Figure 10. Its lower and upper band edges are determined by the BaF_2 window and $(C_2H_5)_2S$ filling gas. It measures a portion of the Schumann continuum radiation which is responsible for dissociating O_2.

Excellent papers by Stober (1962) and Stober, Scolnik, Hennes (1963) describe techniques for construction and absolute calibration of

these chambers, and list their characteristics. The cylindrical chamber is made of ceramic and is gold plated on the inside to form a conducting wall. A collecting wire is installed on the axis of the cylinder, and the window is fastened in place with epoxy. A copper filling tube which is installed at the back of the chamber also provides the electrical connection to the conducting wall of the cylinder.

To operate the chamber a small voltage (20 to 50 volts) was applied between the wall and the center electrode. The center electrode was made negative with respect to the wall so that any photoelectrons emitted from the cylinder would return and not add their effect to that of the ion current. Positive ions therefore were attracted to the center electrode making the output current positive. The two ion chambers flown on each payload were placed opposite one another and were connected to the input of the same electronics. There was no interference between the two chambers since a signal is developed by them only while they point at the sun.

If the sun's rays do not lie along the axis of the ion chamber the signal is attenuated by a $\cos^2 \psi$ factor (for small ψ), where ψ is the angle between the ray direction and the ion chamber axis. One cosine factor comes about because the effective thickness of the window increases by this amount, and the second because the window area the chamber presents normal to the sun-payload line is reduced. Angle ψ was measured with a solar aspect sensor (described in Section 4 of this chapter) and all ion chamber readings were corrected to normal incidence.

The Lyman α ion chambers had to be stored in a desiccator because LiF tends to slowly (over a period of several days) deliquesce and as a result becomes opaque in the vacuum ultraviolet range

(Patterson and Vaughn, 1963). In practice all the ion chambers and ultraviolet experiment electronics were kept in a dry atmosphere as a precaution against leakage currents which might have developed along input leads under humid conditions.

Constructing reliable ion chambers of this type requires meticulous care and a large amount of specialized apparatus (Stober, 1962). They are available commercially, and the chambers used for our work were supplied by Melpar, Inc.

d. Ionization Chamber Calibration. Figure 11 shows a schematic of the system used to determine the relative sensitivity of the ion chambers. This system consisted of two cylindrical chambers A and B separated by a lithium flouride window W. With valve V_1 closed and V_2 open, chamber A was evacuated. Then it was filled with a mixture of hydrogen and helium by closing V_2 and opening V_1 for a short time. The gas was excited by a large D.C. voltage applied between two electrodes in A, making a useful radiation source in the vacuum ultraviolet range, and causing light above 1050 A. to be transmitted through the LiF window into B. An ion chamber was sealed against flange F with an "O" ring and connected in the circuit shown at the bottom of Figure 11. Then V_3 was opened and B was evacuated, removing the air molecules that had been absorbing the vacuum ultraviolet radiation. When the maximum reading was attained, another ion chamber was substituted and the process was repeated. By measuring the currents from several ion chambers in succession, a relative measure of their efficiencies was determined.

There were three purposes in making these tests.

(1) We wished to select the most sensitive ion chambers for flight use; which these were could be quickly determined.

(2) If the ion chambers were given two tests a period of several weeks apart, any large change in the relative sensitivity of a chamber could be detected. A change in the sensitivity usually indicated a defect such as leaking of the filling gas or degradation of the window. With reliable ion chambers the relative readings could be reproduced to within 5 percent over a period of several weeks.

(3) A check of a completed unit, including the ion chambers and electronics could be made with this system prior to flight.

Absolute calibration of the ion chambers was not required. The flux of Lyman α radiation from the sun varies by no more than a few percent and its magnitude is well known (Friedman, 1963). Therefore by noting the current from the 1216 A. ion chambers above the absorbing atmosphere, an in-flight calibration was made. The 1450 A. data was not used in any way which required the absolute value of the flux to be known.

3. X-ray Experiment

The detector used for this experiment was an Amperex 501N Geiger tube, pictured in Figure 9. Its thin mica window and argon filling gave it a response of 2 to 12 A. as shown in Figure 12. A relative measure of the efficiency of these tubes was made by placing each in turn at a given distance from a radioactive source and recording the counting rate. No absolute calibration was attempted.

One problem which must be dealt with carefully when working with high voltage in space is to be sure that no breakdown or corona occurs when the unit is subjected to the vacuum present during flight.

Commercially built power supplies (Venus Scientific Co.) were used, the Geiger unit was potted with RTV high voltage encapsulating material, and the entire unit was tested in a laboratory vacuum system prior to flight. Figure 13 is a photograph of a Geiger tube and its power supply ready for mounting in the payload.

Each Geiger tube was operated near the center of its plateau. The case of a tube was connected to ground through a resistor as shown in the circuit diagram (Figure 14). When the tube fired, the current drawn raised the potential of the case momentarily, providing a positive output pulse. This signal was then sent to a switch. The switch, normally biassed in the off mode, was turned on by this signal, thereby generating a large fast-rising negative pulse. This pulse was sufficient to drive the commercially made flip-flop circuit, which was used to scale the number of pulses by a factor of two. The output from the flip-flop was sent to the last stage, a monostable multivibrator, which effectively shaped the pulse into a form suitable for the telemetry system.

D. Associated Experiments

Three additional experiments were included to provide supplementary information needed for the interpretation of the primary data.

The solar aspect sensor, supplied by GCA Corporation, gave a measure of the angle between the direction of the sun's rays and the payload axis. The opaque glass front of the unit has a clear diamond-shaped pattern inscribed on it (Figure 13) and a second opaque plate with a pinhole at its center is fixed parallel to and a short distance behind the front plate. Behind the pinhole is a sun-sensitive switch. As the

payload spins on its axis, sunlight can only activate the switch, thereby giving an output signal, when a line from the pinhole to the sun passes through a clear portion of the front window. In general this happens twice per revolution, once on either side of the diamond pattern, and the time between the output signals can be seen to depend on the angle between the sun and the payload axis. The time between these signals and the spin period are all that are needed to find the sun-payload axis angle from the manufacturer's calibration graph (McKinnon and Smith, 1964). It should be noted that a vertical line is scribed inside the diamond pattern on the lower half of the front. Then, when the sun is below the normal to the payload axis, three signals are given per revolution, removing the ambiquity which existed as to the sun's position. These data were used in correcting the ion chamber measurements to normal incidence.

The magnetic aspect sensor (Schonstedt Model RAM-5) gave an output signal which was proportional to the component of the earth's magnetic field which lay along the axis of the sensor. The sensor was mounted normal to the axis of the payload, and since in no case did the direction of the field coincide with the payload axis, the sensor output was a sine wave at the payload spin frequency. These spin results were used in reducing the data from the electron density experiment.

A pressure sensitive baroswitch, calibrated to close at 70,000 feet, was included. During the flights where radar tracking failed, a height trajectory was derived from the switching points during ascent and descent (Maynard, 1966).

5. The Payload-General Information

In addition to the instrument tests already described, temperature and vibration tests were performed on all units. During the early portions of a flight, the accelerations of the payload can be as high as 20 to 50 g, accompanied by severe vibrations. Therefore the instruments were required to survive the following mechanical tests to be certain that they were structurally ready for flight. First, each instrument was given a "bench" test, where the finished unit is slammed against a work bench several times while it is operating. Second, the entire payloads were given a suitable shake test by the Goddard Space Flight Center. It has been our observation that an instrument which could survive these two tests seldom failed during flight for mechanical reasons. Temperature changes inside the payload during flight were not really a problem, because a flight lasted for only a relatively short time. However, all instruments were cycled between -10 and +50°C. while they were operating to assure that no normal temperature changes would affect their operation. It was also felt that this test was likely to show up defective workmanship or electronic components.

Electric power at +28 and -14 Volts was supplied by a battery of silver cells. At each instrument, the voltage was regulated and filtered by a network seen in the circuit diagrams to allow for changes in battery potential during flight and to isolate instruments from one another.

The telemetry transmitter was a Vector FM-FM unit operating at 240 MHz with a power output of 1/4 or 1/2 watt depending on the flight. Eleven subcarrier channels were used, seven by our experiments and the remainder by the other experiment on the payload.

During takeoff, the X-ray Geiger tube, the ultraviolet ion chambers and the solar aspect sensor were covered with protective doors. These doors were released at approximately 40 km by a timer signal. The timer also actuated the relay in the ultraviolet experiment early in the flight to provide a calibration, and was used to provide a nosecone blow-off signal near apogee as required by the other experiment.

The payload covering was made of aluminum. In order that the 1 and 3 MHz transmitter signals could get to the rocket-borne receiving antennas, the section of the covering near these antennas was made of fiberglass.

The rockets used for the first five flights were Nike-Apaches. The last flight employed a Nike-Tomahawk combination.

CHAPTER IV

DATA REDUCTION

1. Flight Records

During flight a ground-based receiver was used to monitor the signal from the payload telemetry transmitter. The receiver was connected to a bank of discriminators (one for each subcarrier used) which unscrambled the data and gave voltage outputs which were identical to the payload transmitter inputs. These discriminator output signals were then recorded by a paper chart recorder. A representative sample when the rocket was at an altitude of about 80 km is reproduced in Figure 15. About .8 seconds worth of data is shown since the chart speed was 10 inches/sec. From top to bottom, the magnetic aspect sensor, 1.005 MHz receiver, 3.385 MHz receiver, magnetic aspect sensor, low gain ultraviolet deck, high gain U.V. deck and solar aspect sensor signals are shown. At the bottom is a timing code supplied by the ground station.

The magnetic aspect sensor signal oscillated with the rocket spin frequency, whereas the oscillation of the receiver signals was due to both the rocket spin and the ionosphere. A comparison of the relative phases of these signals therefore gave a measure of the effect of the ionosphere (Faraday rotation). At the point in the record shown in Figure 15 the rocket was well into the ionosphere, and the 1.005 MHz signal had been absorbed at a lower altitude. The 3.385 MHz receiver record clearly showed a changing phase with respect to the magnetic aspect sensor data. The receiver signal was twice the spin frequency because the receiver antenna lined up with the polarization plane of

the wave twice in each revolution. The varying amplitude of the 3.385 MHz signal was caused by interference between the wave sent up from the ground and one reflected down from higher in the ionosphere.

The low gain channel of the ultraviolet deck was responding to a signal from the 1216A. ion chamber. Notice that this same signal was saturating the high gain channel, and that the signal from the 1450 A. ion chamber was just becoming visible midway between the sawtooth-shaped peaks.

2. Ultraviolet, X-ray and Cosmic Ray Flux Measurements

The current from an ultraviolet ion chamber was found easily by measuring on the paper record with a pair of calipers the height of the calibration signal and comparing this with the size of the ion chamber signal. By measuring the time between the pulses on the solar aspect sensor record and finding the spin period, the angle of the sun's position from the payload axis was found. These angles were used to correct the ion chamber currents to normal incidence readings. The normal incidence ion chamber currents stayed fairly constant above a certain altitude. It was reasoned that nearly all of the absorbing atmosphere for this radiation lay below this point, and the constant ion current was being caused by the known flux above the atmosphere. This provided a method for finding absolute flux levels as a function of altitude.

The relative X-ray and cosmic ray fluxes were recorded simply by counting the pulses on the paper record for each unit time interval. Data for these experiments were recorded on a second paper chart and therefore do not appear in Figure 15.

3. Electron Density

a. Simplified Derivation of Ionospheric Birefringence. The reason for the Faraday rotation effect is that the ionosphere is birefringent; i.e., if the linearly polarized wave which propagates through it is treated as two circularly polarized waves rotating in opposite directions, the index of refraction of the ionosphere for each of the two circular waves is different. The following simplified derivation of this result (Jackson, 1962) is included for the physical insight that it provides.

Consider a plane electromagnetic wave of frequency ω in a very weak uniform plasma propagating in the direction of a uniform magnetic induction B_o (earth's field). If collisions between particles are ignored, and the electrons are assumed to move a distance small compared with a wavelength, the equation of motion of an electron is given by

$$m \frac{d\vec{v}}{dt} = eE\, e^{-j\omega t} + e \frac{\vec{v}}{c} \times \hat{k}\, B_o .$$

The effect of the magnetic induction of the wave is small compared with the effect of $\vec{E}$ and is neglected. The acceleration of the ions present is very small compared with that of the electrons; therefore they are considered stationary.

The electric field is rewritten as a pair of circularly polarized waves; the amplitudes become $\vec{E} = E(\hat{i} + j\hat{j})$ and $\vec{E} = E(\hat{i} - j\hat{j})$. If $\vec{v}$ is assumed to have the form $\vec{v}(t) = v(\hat{i} \pm j\hat{j})\, e^{-j\omega t}$ and is substituted into the first equation, we see

$$\omega m v = j e E \mp \frac{eB_o v}{c}$$

The gyrofrequency of the electrons in the magnetic field is defined as $s = \frac{eB_o}{mc}$. Using this,

$$v = \frac{j\, e}{m\ (\omega \pm s)}\ E\ .$$

The polarization current density in the plasma is then

$$\frac{\partial \vec{P}}{\partial t} \equiv \vec{J} = N_e\ e\ \vec{v}$$

$$\vec{J} = \frac{j\ N_e\ e^2}{m\ (\omega \pm s)}\ \vec{E}\ .$$

This expression is substituted into Maxwell's third equation with the conduction current set equal to 0.

$$\vec{\nabla} \times \vec{H} = \frac{1}{c}\frac{\partial \vec{D}}{\partial t} = \frac{4\Pi}{c}\frac{\partial \vec{P}}{\partial t} + \frac{1}{c}\frac{\partial \vec{E}}{\partial t}$$

$$\vec{\nabla} \times \vec{H} = \left[\frac{j\omega}{c}\frac{4\Pi N_e\ e^2}{m} - j\,\frac{\omega}{c}\right]\vec{E}$$

$$\vec{\nabla} \times \vec{H} = -\,j\,\frac{\omega}{c}\left[1 - \frac{\omega_o^{\,2}}{\omega\ (\omega \pm s)}\right]\vec{E}$$

The plasma frequency is defined as $\omega_o^{\,2} = \frac{4\Pi\ N_e\ e^2}{m}$. The bracket above can be interpreted as the dielectric coefficient ε. Since the index of refraction $n = \sqrt{\varepsilon}$, then

$$n = \left[1 - \frac{\omega_o^{\,2}}{\omega\ (\omega \pm s)}\right]^{1/2} \qquad (18)$$

which has a value that depends on the direction of rotation of the circular wave. The phase velocity of these two waves is different, and their sum gives a linearly polarized wave whose plane of polarization is slowly rotating. Note that the birefringence results only because of the presence of the earth's magnetic field.

b. Generalized Appleton-Hartree Equation. The last expression will now be generalized to the case where the wave propagates at an angle with respect to the magnetic induction lines, and where the effect of collisions between the electrons and molecules is taken into account. For many years the electron collision frequency was assumed constant, independent of electron velocities. The equation that resulted for the index of refraction is called the Appleton-Hartree equation and has been discussed extensively (for example, Ratcliffe, 1959). Then Phelps and Pack (1959) showed by a laboratory measurement that the collision frequency is proportional to the electron energy. The Generalized Appleton-Hartree equation, which takes this factor into account, was first derived by Sen and Wyller (1960). An outline of their derivation is given in Appendix A, and the results which were used to determine the electron density are presented here.

In order to compute the indices of refraction, the plasma frequency ω_o, collision frequency ν_m, wave frequency ω and gyrofrequency s are used to compute

$$a = \frac{\omega_o^2}{\nu_m^2} C \frac{3}{2}\left[\frac{\omega}{\nu_m}\right] \qquad d = \frac{5\,\omega_o^2}{2\omega\nu_m} C \frac{5}{2}\left[\frac{\omega - s}{\nu_m}\right]$$

$$b = \frac{5\ \omega_o^2}{2\omega\nu_m}\ C\ \frac{5}{2}\left[\frac{\omega}{\nu_m}\right] \qquad e = \frac{\omega_o^2(\omega + s)}{\omega\nu_m^2}\ C\ \frac{3}{2}\left[\frac{\omega + s}{\nu_m}\right]$$

$$c = \frac{\omega_o^2(\omega - s)}{\omega\nu_m^2}\ C\ \frac{3}{2}\left[\frac{\omega - s}{\nu_m}\right] \qquad f = \frac{5\ \omega_o^2}{2\omega\nu_m}\ C\ \frac{5}{2}\left[\frac{\omega + s}{\nu_m}\right]$$

The $C_p(x)$ are known as Dingle integrals, and are of the form

$$C_p(x) = \frac{1}{p\ !}\int_o^\infty \frac{\varepsilon^p\ d\varepsilon}{\varepsilon^2 + x^2\ e^\varepsilon} \quad .$$

These have been tabulated (Dingle, Arndt, Roy, 1957). Hara (1963) has written a series approximation for these integrals which is suitable for computer use. Using these six quantities, compute

$$\varepsilon_I = (1 - a) - j\ b$$

$$\varepsilon_{II} = 1/2\ (f-d) + \frac{j}{2}\ (c - e)$$

$$\varepsilon_{III} = [a - 1/2\ (c - e)] + j\ [b - 1/2\ (f + d)]$$

and then

$$A = 2\ \varepsilon_I\ (\varepsilon_I + \varepsilon_{III})$$

$$B = \varepsilon_{III}\ (\varepsilon_I + \varepsilon_{III}) + \varepsilon_{II}^2$$

$$C = 2\ \varepsilon_I\ \varepsilon_{II} \qquad D = 2\ \varepsilon_I \qquad E = 2\ \varepsilon_{III}$$

The complex indices of refraction are given by

$$\left[n - \frac{j\ \kappa\ c}{\omega}\right]^2 = L - j\ M = \frac{A + B\ \sin^2\phi \pm \sqrt{B^2\ \sin^4\phi - C^2\ \cos^2\phi}}{D + E\ \sin^2\phi} \qquad (19)$$

where is the angle between the propagation direction and the earth's field lines. The two values of the real part of the refraction indices are finally given by

$$n = \sqrt{\frac{L + \sqrt{L^2 + M^2}}{2}} \tag{20}$$

The imaginary part can be computed by

$$\frac{\kappa c}{\omega} = \sqrt{\frac{-L + \sqrt{L^2 + M^2}}{2}}$$

where κ is the absorption coefficient. This imaginary part results from the inclusion of the collision term in the equation of motion. The effect of collisions on the wave is to remove energy from it, and the wave is therefore attenuated by a factor $e^{-\frac{\kappa c z}{\omega}}$. In general, the values of κ are not the same for both circular waves, which implies that one is more highly attenuated than the other. In this case the composite wave is no longer linear but elliptically polarized.

c. Faraday Rotation. It remains to derive an expression for the rotation of the polarization plane of a linearly polarized wave in terms of the indices of refraction.

At some wave maximum in space, the two circular waves are lined up. A short distance dh along the path of the ray, the circular waves have rotated through angles Ω_1 and Ω_2 respectively (Figure 16). Then

$$\Omega_2 + d\Omega = \Omega_1 - d\Omega$$

$$2\, d\Omega = \Omega_1 - \Omega_2$$

But $\Omega = \frac{2\Pi\ dh}{\lambda}$, so

$$\frac{d\Omega}{dh} = \Pi \left[\frac{1}{\lambda_1} - \frac{1}{\lambda_2}\right]$$

Now $\frac{c}{n} = f\lambda$ or $\frac{1}{\lambda} = \frac{fn}{c}$. Substitution into the last expression gives

$$\frac{d\Omega}{dh} = \frac{f\Pi}{c}(n_1 - n_2)$$

(21)

$$\frac{d\Omega}{dh} = \frac{\omega}{2c}(n_1 - n_2),$$

which shows that the rotation angle of the plane of polarization of a linearly polarized wave per unit distance in the direction of propagation is proportional to the difference in the indices of refraction.

d. Electron Density Results. The experimental value of the angle of rotation of the polarization plane per unit distance was determined in this manner. The distance from each peak of the receiver signal to the corresponding peak or valley of the magnetic aspect sensor signal was measured in degrees from the paper record. These values of angle vs. time were plotted, giving results shown in Figures 17 through 25.

At this stage trajectory data giving rocket altitude vs. time were required. For Figures 17, 22 and 23 radar tracking during flight provided this information. Radar data for the others were insufficient, and by using the baroswitch points a computer, executing a program supplied by Maynard (1966), derived the needed trajectories. Altitudes were then marked on the previous graphs and the angle of rotation per unit height was read directly.

All quantities in (21) were now known except $(n_1 - n_2)$ and therefore (21) determined the experimental value of this quantity.

The computer was programmed to compute values of $(n_1 - n_2)$ using the Generalized Appleton-Hartree equation (20). This program is shown in Appendix C. The gyrofrequency was calculated using the appropriate values of the earth's magnetic field and the collision frequency for each height was determined by a method described later. Then, beginning with an assumed value of ω_o^2 (proportional to N_e) the computer proceeded by an iterative process to alter ω_o^2 until the computed value of $(n_2 - n_1)$ matched the experimental value. It then printed out the determined value of N_e.

CHAPTER V

RESULTS

1. Flight Information

The six flights were made from various geographical locations since the other experiment on the payload was studying a latitude effect. The first flight was made from Wallops Island, Virginia on February 3, 1965, with a solar zenith angle χ of 59 degrees. The next three flights were made in the South Pacific from the deck of the USNS Croatan as part of the First NASA Mobile Launch Expedition. These were flown at 12° South on April 2, 1965 (χ = 58°), 30° South on April 5 (χ = 54°) and 60° South on April 13 (χ = 70°). The fifth shot was from Churchill, Manitoba on August 24, 1966 (χ = 58°) and the last was from Wallops Island on November 30, 1966 (χ = 66°). Equipment all functioned properly except in the following cases. On the first four flights a commercially made mechanism failed to release the protective doors which were over the solar flux detectors. The instruments appeared to operate properly in all cases, but were never exposed to the sun. Also, due to ground-based transmitter failure, the 3.385 MHz Wallops 1965, the 1.005 MHz 30° S. and the 1.005 MHz 60° S. propagation experiments did not yield data.

2. Ultraviolet Flux Data

Figures 26 through 29 depict the ion current as a function of altitude from the ultraviolet experiments. All curves show a levelling off at high altitudes which indicates that the rocket was essentially above the absorbing atmosphere at these points. It should be noticed

that the two 1216 A. records are very similar, with the first detectable flux and levelling off point occurring at approximately the same altitude for each. The apparent difference in altitudes at which the rocket was above the absorbing atmosphere for the two 1450 A. measurements is unexplained. On the Churchill flight very low ion current levels were being recorded, and some of the difference in the two graphs may be due to a measurement error.

3. Electron Collision Frequency from Ultraviolet Data

Electron collision frequency information for the lower ionosphere was obtained from the ultraviolet ion current measurements. From (3),

$$S = S_\infty \exp(-\tau \sec \chi)$$

and from (5a) $\tau = \frac{\sigma_a p}{mg}$

Therefore $$\ln \frac{S}{S} = - \frac{\sigma_a p \sec \chi}{mg}$$

$$p = \frac{mg}{\sigma_a \sec \chi} \ln \frac{S_\infty}{S} \quad .$$

Nearly all the 1216 A. flux is absorbed by O_2 with an absorption cross section of 8.6×10^{-21} cm^2 (Po Lee, 1955). Inserting for m the mass of an O_2 molecule a value for the partial pressure of O_2 was found. Below 90 km the atmosphere has the same relative composition that it has at ground level, and therefore the total pressure may be calculated. A laboratory measurement by Phelps (1960) showed that the collision frequency for electrons is proportional to their energy. Since the pressure of a gas is proportional to its energy, Phelps showed that the

collision frequency for electrons of energy kT can be set proportional to the total gas pressure, according to the relation

$$\nu_m = 9 \times 10^7 \ p \ (sec^{-1})$$

where p is in mm Hg. Collision frequencies derived by this method are shown in Figure 30. There is excellent agreement between the data from these two flights, and these data are also consistent with collision frequencies derived by Kane (1961) by another method. It should be emphasized that only the ratio of the flux at a given altitude to that above the atmosphere is involved, and no knowledge of the absolute flux was required.

The collision frequency spectrum could not be calculated from the 1450 A. data. It is known that above 90 km part of the O_2 is dissociated into O, but the respective number densities of these gases as a function of altitude is uncertain. Also, mixing processes are not sufficient to maintain the constant composition that is found lower in the atmosphere. For these reasons it is not possible to accurately calculate the total pressure from the partial pressure of O_2 at these altitudes. In addition the number relating ν_m and p measured by Phelps is valid only under good mixing conditions.

4. Experimental Electron Density Profiles

The electron density data derived are shown in Figures 31 through 36. The values of the collision frequency from Figure 30 were used for all calculations. The value of the calculated electron density

depends strongly on the collision frequency values used at low altitudes where $\nu_m \geq \omega$, so it is important to know the correct collision frequency profile for the lower D region. Where $\nu_m < \omega$, the electron density results are nearly independent of the collision frequency values used.

The points shown represent an average of the data over a height of 1 km. The uncertainty in each point is a result of the interference between the primary wave from the ground and the wave reflected from higher in the ionosphere, which in effect distorted the primary wave somewhat.

All flights with the exception of the Wallops 1966 flight were flown during quiet solar conditions. Preliminary ionosonde records taken near the flight time on November 30, 1966, indicated some sort of disturbance with the report of "blanketing sporadic E." In addition our X-ray records for this flight indicated disturbed solar conditions.

The Wallops 1965 1.005 MHz experiment measured electron density in the low altitude range of 60 to 76 km (Figure 31) and recorded a minimum of 150 electrons/cm ^{3}.

On the Croatan shots an ionosonde was operated shortly before each flight. The data from it were made available to us (Wright, 1966) and are plotted along with our values of electron density in Figures 32 through 34. Excellent agreement with our measurements is seen if the ionosonde readings are transposed 1 1/2 to 3 km in altitude (required by group delay considerations). Ionosonde results are inherently uncertain by small heights and in addition our altitude scale is uncertain by 1 or 2 km; radar tracking was not reliable during these flights and altitudes were derived from the baroswitch points.

The Churchill record, which is a typical daytime quiet sun profile (Figure 36), shows good agreement between the results derived

from the two receiver experiments at the points where they overlap. The 1.005 MHz experiment detected as few as 40 electrons/cm^3 with an accuracy of a factor of two.

The profile found during the Wallops 1966 flight is seen in Figure 36. The altitude scale was derived from the baroswitch points because no radar data for this flight has been made available.

The zenith angle was nearly the same (χ = 60°) for all these flights, and even though they were made over a period of nearly two years at varying geographical locations the electron density results are fairly consistent from 76 to 104 km except for the Wallops 1966 flight below 88 km, as shown in Figure 37. It can be seen from Figures 31 and 35 that there is no such consistency in the results below 76 km. The solar X-ray flux is the only component of the ionizing radiation in this region that varies over a wide range, and it would most likely be responsible for these disparities. This flux increases during a solar disturbance and could account for the increased electron density seen below 88 km during the Wallops 1966 flight. The flux at the lower end of the X-ray spectrum (2 to 4 A.) varies widely from day to day and probably accounts for the range of electron profiles below 76 km.

5. $(n_1 - n_2)$ Sign Reversal

The 1.005 MHz Faraday rotation data from the 12° S. and Wallops 1966 shots (Figures 18 and 24) show the plane of polarization of the signal beginning to rotate in one direction, then reversing direction for a short time and finally rotating in the original direction until the signal fades out. Aikin, Kane, and Troim (1964) have reported a similar effect. This result is surprising, because the simple theory

predicts that if no electrons are present in the vicinity of the measuring receiver, the plane of the wave does not rotate (slope of these graphs is 0) or if electrons are present, then the plane of the wave rotates by an amount proportional to the integrated number density always in the same direction (provided the electron density is small). From (21) the slope of these graphs is proportional to the magnitude of $(n_1 - n_2)$ and a reversal in the sign of $(n_1 - n_2)$ is implied by the changing of the slope. This led to an investigation of the Generalized Appleton-Hartree equation to see if there were conditions under which the sign of $(n_1 - n_2)$ could change.

The general case proved very complex, so two special cases, (a) when the wave propagates nearly along the magnetic field direction (quasi-longitudinal) and (b) when the propagation and magnetic field directions are nearly at right angles (quasi-transverse), were studied. The radical in (19) was expanded for each of these cases. Also, in each case ω_o^2/ν_m^2 was assumed less than one.

In the quasi-longitudinal case, $C^2 \cos^2\phi >> B^2 \sin^4\phi$. Then $n_2 = n_1$ when c = e, or, putting in the explicit forms, when

$$(\omega - s)\, C_{\frac{3}{2}}\left[\frac{\omega - s}{\nu_m}\right] = (\omega + s)\, C_{\frac{3}{2}}\left[\frac{\omega + s}{\nu_m}\right] \qquad (22)$$

With quasi-transverse conditions, $B^2 \sin^4\phi >> C^2 \cos^2\phi$; $n_2 = n_1$ when $2a = c + e$ or when

$$2\, C_{\frac{3}{2}}\left[\frac{\omega}{\nu_m}\right] = \left(\frac{\omega - s}{\omega}\right) C_{\frac{3}{2}}\left[\frac{\omega - s}{\nu_m}\right] + \left(\frac{\omega + s}{\omega}\right) C_{\frac{3}{2}}\left[\frac{\omega + s}{\nu_m}\right] \qquad (23)$$

The detailed calculation of (22) and (23) is given in Appendix B.

Two conclusions can be drawn at once from these equations. First, the $(n_1 - n_2) = 0$ point is independent of the electron density. Second, if $s > \omega$, there will be no reversal in the sign of $(n_1 - n_2)$. To check these results, the computer programmed with the full Generalized Appleton-Hartree equation was used to evaluate $(n_1 - n_2)$ under various conditions. The $(n_1 - n_2) = 0$ points found by the computer matched well those found by the approximate solutions (22) and (23). The two conclusions above were supported by the computer data. Changing the electron density by a factor of 10^3 only changed the $(n_1 - n_2) = 0$ point by 20 percent. Figure 38 is a graph of $(n_1 - n_2)$ vs. ν/ω, with the electron density held constant at 1250 cm^{-3}, for conditions like those during the 12° S. flight. Longitudinal, transverse and the 12° S. cases are shown.

There are difficulties in trying to explain the curves in Figures 18 and 24 by using these results. For the Wallops 1966 flight, $s > \omega$ so the effect should not be seen at all. For 12° S., this theory predicts that the rotation will begin in one direction, and will then change and continue in the new direction. This was not observed experimentally. Also, the size of the effect derived theoretically, even assuming 1250 electrons/cm^3 at altitudes under 65 km, is smaller than that observed by a factor of ten.

Were the experiments flown sensitive enough to see the rotation direction change predicted here? If it is assumed that the minimum amount of rotation detectable is one degree per km, the following empirically derived experimental conditions must be satisfied for the effect to be seen.

(a) s/ω should be very close to but less than one to make the effect large. Figure 39 shows this dependence.

(b) ω_o^2/ω^2 must be at least 10^{-2}.

(c) The value of ν/ω at which the reversal in the direction of rotation takes place can then be found from (22) or (23).

For the 1.005 MHz experiment, conditon (a) dictates that the flights should have taken place at a geographical location where $s \approx 6.3 \times 10^6$ sec^{-1}. Since at 12° S. $s = 4.87 \times 10^6$ sec^{-1}, to have the effect observable, requirement (b) must be made more stringent and ω_o^2/ω^2 must be at least 10^{-1}. This modified requirement specifies an electron density of 1250 cm^{-3}, and with quasi-transverse conditions ν_m for sign reversal would be 2.5×10^6 sec^{-1} which is at about 75 km. Therefore it appears that it might have been possible to observe the predicted effect during this one flight. For all other flights $s > \omega$ and the effect should not be present.

For the 3.385 MHz experiment, the first requirement ($s \approx 2.25 \times 10^7$ sec^{-1}) is not satisfied at any geographical location. If it were, the second and third requirements with quasi-longitudinal conditions ask for an electron density of 1250 cm^{-3} below 63 km which is unlikely to be achieved.

It is interesting to calculate the requirements for a propagation experiment which would show the optimum effect at usual launching sites. For North America $s \approx 1 \times 10^7$ sec^{-1} and therefore a wave frequency of 1.75 MHz would be the best one to use. The rotation reversal would take place with quasi-longitudinal conditions when $\nu_m = 3.3 \times 10^6$ sec^{-1} or at about 70 km, and 380 electrons/cm^3 would be needed to see the effect. Since these conditions are possible, the effect should be observable. This would be a desirable experiment to

run, because at the altitude where the rotation direction reverses, the value of the collision frequency would be absolutely determined. However, the rotation reversal due to some other condition seen in Figures 18 and 24 would likely still be present; it might be difficult to pick unambiguously the altitude where the reversal due to this effect took place.

Since this work did not explain the curves in Figures 18 and 24, another explanation was sought. Aspect sensors did not indicate any appreciable vibration, coning or change in spin rate during these times, so some kind of mechanical disturbance on the payload was ruled out as an explanation.

It was noticed upon closer investigation that on both of these flights, the 3.385 MHz experiment underwent the same kind of rotation reversal, although to a lesser extent, at the same altitude. This is shown in Figures 40 and 41. This is another factor that would eliminate the explanation offered by the preceding theoretical derivation, since the derivation predicts that the reversal should occur at different altitudes for each frequency.

The Faraday rotation recorded at any altitude is the total angle through which the plane of the wave has been rotated, and depends on the integrated electron density up to the altitude of the measuring equipment. Therefore, if there was a change of electron density over the path between the transmitter and receiver, it seems plausible that the curves in question could result. This is the only explanation of the observed data that seems reasonable at present.

This dependence of the rotation observed at some altitude on the integrated electron density is really a weakness in the Faraday rotation method of determining electron density. Provided the electron

distribution stays constant in time, the theory is very good; if it doesn't there is no way to know how the distribution has changed as a function of altitude. When the electron density at the receiver position is large this is not really a problem, but it may be with a small electron density at the receiver. The important consideration is how the electron density change over a range of altitudes affects the value of the integrated electron density compared with the effect of N_e dh for the element of path just added. All that can be done, unless there is evidence to the contrary, is to assume that there was no time change of electron distribution during the flight and compute electron densities on this basis.

6. Solar X-ray Flux

Figure 42 is a plot of X-ray and energetic charged particle flux for the Churchill flight. The maximum in the charged particle counting rate at low altitudes is due to the secondary charged particles created there. The X-ray detector was also sensitive to the charged particles as indicated by the increased counting rate at low altitudes, so the charged particle counting rate was taken as a measure of the background for this detector throughout the flight. The X-ray counts indicate primarily the flux of 6 to 9 A. X-rays as seen from Figure 12.

On the Wallops 1966 flight the X-ray counting rate increased rapidly at an altitude of 84 km as seen in Figure 43, indicating that a solar disturbance was in progress at the time. The counter was saturated after 105 km.

Friedman (1960) points out that a great enhancement of the 2 to 12 A. band usually accompanies a solar flare. The flux of softer X-rays (20 - 100 A.) and extreme ultraviolet (200 - 910 A.) increases somewhat at these times also, with the amount of enhancement decreasing at increasing wavelengths. Above 910 A. little if any change is seen. It is also well known that a disturbed lower ionosphere often results nearly simultaneously with the observation of a solar flare. It is thought that ionization caused by the additional flux of 2 to 12 A. is responsible.

November 30, 1966 was classed by the Environmental Science Services Administration (ESSA) as a disturbed day, with geomagnetic planetary indices K_p between 4 and 5. On a typical day during November 1966 K_p was 0 to 2. On this day a class 1B flare was observed about 1 1/2 hours before flight time. It was accompanied by a Sudden Shortwave Fadeout which lasted about 20 minutes. In addition, an ESSA satellite, which samples the solar X-ray flux for short intervals, reported some enhancement of the 0 to 8 A. flux when it sampled about 2 hours before flight time. An ionosonde operated before and during the flight indicated "blanketing Sporadic E conditions."

7. Comparison of Calculated and Measured Electron Density

From the solar flux levels measured on the Churchill and Wallops 1966 flights the electron density expected in the D region was calculated. Equations (4) and (14) were used to compute the profile due to Lyman α by assuming a value for S_∞ of 5.1 erg/cm^2 sec. and then using our measured values of flux, and adopting values of $n(NO) = 1.5 \times 10^7$ molecules/cm^3, $\sigma_i = 2.4 \times 10^{-18}$ cm^2, $\eta = .81$ and $\alpha_D = 1.6 \times 10^{-6}$ cm^3/sec. as discussed in Chapter II.

Poppoff, Whitten and Edmonds (1964) have given a summary of the non-flare solar X-ray contribution to the electron density. They show that the measured X-ray spectrum depends strongly on the position in the solar cycle, and consequently so does the X-ray contribution to the electron density. An electron profile for a solar cycle position representative of the Churchill flight date was adopted from their work, with their altitude scale adjusted to agree with the relative flux levels measured by us.

The results for Churchill are shown in Figure 44. The predicted and measured electron density profiles agree quite well. It is seen that Lyman α is apparently the predominant radiation, but in the region from 83 to 88 km the X-ray contribution is important as well. A lower E region process, not investigated, would be necessary to follow the measured curve above 87 km.

The Wallops 1966 flight results (Figure 45) are not nearly as satisfying. The X-ray contribution was calculated assuming the same X-ray spectrum as was used for the Churchill calculations. Although the flux was known to be large (Figure 43) this spectrum was most certainly quite different from that found with quiet solar conditions. If the proper spectrum was known the calculated and measured values would likely agree more closely.

It is evident that more work of this type needs to be carried on, as well as experimentation which would give more confidence to the values of the NO concentration and effective recombination coefficients for constituents present in the D region.

CHAPTER VI

CONCLUSIONS

The radio propagation experiments gave a reliable measure of the electron density under all conditions from a few hundred to 10^5 electrons/cm^3 and under some conditions provided a measure of as few as 40 electrons/cm^3. The reliability at the very low values seems at present to be contingent on the assumption of a distribution which does not change during the time when the rocket is passing through the region of interest. There was good agreement with ionosonde measurements and between simultaneous measurements by the two different frequency experiments where it was possible to compare them.

The electron collision frequencies for use in processing the electron density data were derived from the Lyman α radiation measurements. The results from two flights were consistent with measurements made by Kane (1961).

Simultaneous measurements of ionizing radiation and electron density for the D region during a quiet sun time indicated, on the basis of one flight, that the D region is formed primarily by Lyman α acting on NO with solar X-rays playing a minor role as an ionizing agent. The same measurements made during a flight when the sun was disturbed indicated that the Lyman α - NO process is not sufficient to explain the observed electron density, which substantiates the prevelant theory of solar X-rays being the important radiation during a disturbance.

A study of the Generalized Appleton-Hartree equation , prompted by an observed reversal in the Faraday rotation direction on two flights, showed that $(n_1 - n_2) = 0$ under specified conditions.

Although the experimentally observed reversals did not satisfy these conditions, and therefore need to be explained by other considerations, the Faraday rotation reversal predicted by the equations should be observable by a propagation experiment with a carefully chosen wave frequency.

There are three areas in which further study would be worthwhile. First, a series of propagation experiments should be designed and flown specifically for observing the Faraday rotation reversal effect.

Second, it would be useful to measure electron densities with a probe in conjunction with the propagation experiment. This should be done with the hope that correction factors for the probe data in the lower ionosphere could be derived. Eventually if enough confidence in the probe measurements was gained, the propagation experiment could be omitted.

Finally, the key to deciding whether solar X-rays or Lyman α is most important in forming the D region lies in repeated measurements of these ionizing radiations along with the electron density. Unless there are day to day variations in the NO concentration the contribution from Lyman α should be fairly constant. Since the Lyman α flux above the atmosphere is known to be nearly constant, an absolute calibration of these detectors is not really needed. On the other hand, the wide variations in spectrum and intensity of the 2 to 12 A. X-rays makes an absolute calibration of the spectral response and sensitivity of these detectors very desirable.

BIBLIOGRAPHY

Aikin, A. C. and S. J. Bauer, The Ionosphere, Introduction to Space Science, ed. by W. N. Hess, 133-164, Gordon and Breach, New York (1965).

Aikin, A. C., J. A. Kane, and J. Troim, Interpretation of a Rocket Measurement of Electron Density in the Lower Ionosphere, Space Research IV, 358-362 (1964).

Aikin, A. C., J. A. Kane, and J. Troim, Some Results of Rocket Experiments in the Quiet D Region, J. Geophys. Research 69, 4621-4628 (1964).

Barth, C. A., Nitric Oxide in the Upper Atmosphere, Annales de Geophysique 22, 198-207 (1966).

Bourdeau, R. E., Ionospheric Research from Space Vehicles, Sp. Sci. Reviews I, 683-728 (1962-63).

Bourdeau, R. E., A. C. Aikin, and J. L. Donley, Lower Ionosphere at Solar Minimum, J. Geophys. Research 71, 727-740 (1966).

Chapman, S., The Absorption and Dissociative or Ionizing Effect of Monochromatic Radiation in an Atmosphere on a Rotating Earth, Proc. Phys. Soc. 43, 26-45 (1931).

Chapman, S. and T. G. Cowling, The Mathematical Theory of Non-Uniform Gases, Cambridge University Press, New York (1960).

Davies, K., Ionospheric Radio Propagation, Chpt. 1, U. S. Government Printing Office, Washington, D. C. (1965).

Dingle, R. B., D. Arndt, and S. K. Roy, The Integrals $C_p(x) = (p!)^{-1} \int_0^\infty \varepsilon^p (\varepsilon^2 + x^2)^{-1} e^{-\varepsilon} d\varepsilon$ and $D_p(x) = (p!)^{-1} \int_0^\infty p (\varepsilon^2 + x^2)^{-2} e^{-\varepsilon} d\varepsilon$ and their Tabulation, Appl. Sci. Research 6B, 155-164 (1957).

Donahue, T. M., On the Ionospheric Conditions in the D Region and Lower E Region, J. Geophys. Research 71, 2237-2242 (1966).

Friedman, H., The Sun's Ionizing Radiations, Physics of the Upper Atmosphere, ed. by J. A. Ratcliffe, 133-218, Academic Press, New York (1960).

Friedman, H., Ultraviolet and X-rays from the Sun, Ann. Rev. Astronomy and Astrophys. 1, 59-96 (1963).

Gunton, R. C. and T. M. Shaw, Electron-Ion Recombination in Nitric Oxide in the Temperature Range 196 to 358° K., Phys. Rev. 140A, 756-763 (1965).

Hara, E. H., Approximations to the Semiconductor Integrals C_p (x) and D_p (x) for use with the Generalized Appleton-Hartree Magnetoionic Formulas, J. Geophys. Research 68, 4388-4389 (1963).

Heikkila, W. J., Impedance and Conductivity Probes, Presented at the Second Conference on Direct Aeronomic Measurements in the Lower Ionosphere, Urbana, Illinois Sept. 26-30 (1965).

Hinterreger, H. E., L. A. Hall, and G. Schmidtke, Solar XUV Radiation and Neutral Particle Distribution in the July 1963 Thermosphere, Space Research V, 1175-1190 (1965).

Houston, R. E., The Effect of Certain Solar Radiations in the Lower Ionosphere, Penn. State University Scientific Report 95 (1957).

Jackson, J. D., Classical Electrodynamics 226-229, John Wiley and Sons, Inc., New York (1962).

Jackson, J. E. and J. C. Seddon, Ionosphere Electron Density Measurements with the Navy Aerobee - hi Rocket, J. Geophys. Research 63, 197-208 (1958).

Kane, J. A., Re-evaluation of Ionospheric Electron Densities and Collision Frequencies Derived from Rocket Measurements of Refractive Index and Attenuation, J. Atmospheric Terrest. Phys. 23, 338-347 (1961).

Lockwood, J. A., Private communication (1966).

Malmstadt, H. V., C. G. Enke, and E. C. Toren, Electronics for Scientists, Chapt. 8, W. A. Benjamin, Inc., New York (1963).

Maynard, N. C., Measurements of Ionospheric Currents, Thesis, University of New Hampshire (1966).

McKinnon, P. J. and L. G. Smith, A Solar Aspect Sensor for Sounding Rockets, G. C. A. Technical Report 64-12-N (1964).

Moler, W. F., VLF Propagation Effects of a D Region Layer Produced by Cosmic Rays, J. Geophys. Research 65, 1459-1468 (1960).

Nicolet, M. and A. C. Aikin, The Formation of the D Region of the Ionosphere, J. Geophys. Research 65, 1469-1483 (1960).

Patterson, D. A. and W. H. Vaughn, Influence of Crystal Surface on the Optical Transmission of Lithium Fluoride in the Vacuum Ultraviolet Spectrum, J. Opt. Soc. Am. 53, 851-855 (1963).

Phelps, A. V., Propagation Constants for Electromagnetic Waves in Weakly Ionized Dry Air, J. Appl. Phys. 31, 1723-1729 (1960).

Phelps, A. V. and J. L. Pack, Electron Collision Frequencies in Nitrogen and in the Lower Ionosphere, Phys. Rev. Letters 3, 340-342 (1959).

Philbrick Researches Engineering Staff, Applications Manual for Computing Amplifiers for Modelling, Measuring, Manipulating and Much Else, Nimrod Press, Boston (1966).

Po Lee, Dissociation and Photoionization of Oxygen (O_2) as inferred from Measuring Absorption Coefficients, J. Opt. Soc. Am. 45, 703-709 (1955).

Poppoff, I. G., R. C. Whitten, and R. S. Edmonds, The Role of Nonflare X Radiation in the D Region, J. Geophys. Research 69, 4081-4085 (1964).

Radio Amateur's Handbook, ed. by Byron Goodman, American Radio Relay League, Newington, Conn. (1966).

Ratcliffe, J. A., The Magneto-Ionic Theory and its Applications to the Ionosphere, Cambridge University Press, Cambridge (1959).

Ratcliffe, J. A. and K. Weekes, The Ionosphere, Physics of the Upper Atmosphere, ed. by J. A. Ratcliffe, 377-470, Academic Press, New York (1960).

Reid, G. C., Physical Processes in the D Region of the Ionosphere, Rev. of Geophysics 2, 311-333 (1964).

Sagalyn, R. C. and M. Smiddy, Rocket Investigation of the Electrical Structure of the Lower Ionosphere, Space Research IV, 371-387 (1964).

Salah, J. E. and S. A. Bowhill, Collision Frequencies and Electron Temperatures in the Lower Ionosphere, University of Illinois Aeronomy Report 14 (1966).

Schaefer, E. J. and M. H. Nichols, Upper Air Neutral Composition Measurements by a Mass Spectrometer, J. Geophys. Research 69, 4649-4660 (1964).

Stober, A. K., Ceramic Vacuum Ultraviolet Ion Chambers, NASA Technical Note D-1180 (1962).

Stober, A. K., R. Scolnik, and J. P. Hennes, A. Vacuum Ultraviolet Photoionization Detector, NASA Technical Note D-1715 (1963).

Sen, H. K. and A. A. Wyller, On the Generalization of the Appleton-Hartree Magnetoionic Formulas, J. Geophys. Research 65, 3931-3950 (1960).

Szachta, F. D., The Design of an Improved Receiver for Rocket Experiments, Thesis, University of New Hampshire (1965).

U. S. Standard Atmosphere, U. S. Government Printing Office, Washington, D. C. (1962).

Van Zandt, T. E. and R. W. Knecht, The Structure and Physics of the Upper Atmosphere, Space Physics, ed. by D. P. LeGalley and A. Rosen, 166-221, John Wiley and Sons, Inc., New York (1964).

Watanabe, K., Photoionization and Total Absorption Cross-Section of Gases I. Ionization Potentials of Several Molecules. Cross-Sections of NH_3 and NO., J. Chem. Phys. 22, 1564-1570 (1954).

Webber, W., The Production of Free Electrons in the Ionospheric D Layer by Solar and Galactic Cosmic Rays and the Resultant Absorption of Radio Waves, J. Geophys. Research 67, 5091-5106, (1962).

Whitten, R. C. and I. G. Poppoff, Physics of the Lower Ionosphere, Prentice-Hall, Inc., Englewood Cliffs, New Jersey (1965).

Whitten, R. C., I. G. Poppoff, R. S. Edmonds, and W. W. Berning, Effective Recombination Coefficients in the Lower Ionosphere, J. Geophys. Research 70, 1737-1742 (1965a).

Wilkes, M. V., A Table of Chapman's Grazing Incidence Integral Ch (x, X), Proc. Phys. Soc. B67, 304-308 (1954).

Wright, W. J., Private communication (1966).

APPENDIX A

GENERALIZED APPLETON-HARTREE EQUATION

This derivation of the complex index of refraction of the ionosphere was first presented by Sen and Wyller (1960). Earlier expressions were derived with an assumption that the frequency of electron-molecule collisions is independent of electron velocity, whereas this work is valid for any collision frequency dependence and requires only that it be specified in order to obtain a closed form solution. Phelps and Pack (1959) measured the electron collision frequency in the laboratory and found it was proportional to the electron energy. Utilizing this result allows a calculation of the closed form solution for the index of refraction.

Begin with two of Maxwell's equations.

$$\vec{\nabla} \times \vec{E} = -\frac{1}{c}\frac{\partial \vec{H}}{\partial t} \qquad \vec{\nabla} \times \vec{H} = \frac{4\Pi}{c}\vec{J} + \frac{1}{c}\frac{\partial \vec{D}}{\partial t}$$

We assume that the conduction current is 0, and express the electron motion as a displacement current.

$$\vec{\nabla} \times (\vec{\nabla} \times \vec{E}) = -\frac{1}{c}\frac{\partial}{\partial t}\vec{\nabla} \times \vec{H}$$

$$\vec{\nabla}(\vec{\nabla} \cdot \vec{E}) - \nabla^2 \vec{E} = \frac{1}{c^2}\frac{\partial^2}{\partial t^2}\vec{D}$$

Assume an electric intensity of the form $\vec{E} = \vec{E}_o\, e^{j(\omega t - \vec{k} \cdot \vec{r})}$ and the last equation can be written

$$-k^2 \vec{n}\,(\vec{n} \cdot \vec{E}) + k^2 \vec{E} = \frac{\omega^2}{c^2}\vec{D} = \frac{\omega^2}{c^2} \|\varepsilon\| \vec{E}$$

where $\|\varepsilon\|$ is the dielectric tensor for the medium and $\vec{n}$ is a unit vector in the wave propagation direction. Writing $k = \frac{\omega}{u}$ where u is the phase velocity of the wave, the following relation between the square of the complex index of refraction $\frac{c^2}{u^2}$ and $\|\varepsilon\|$ results.

$$\frac{c^2}{u^2}\left[\vec{E} - \vec{n}\,(\vec{n} \cdot \vec{E})\right] = \|\varepsilon\|\,\vec{E} \tag{A1}$$

The displacement current density is

$$\frac{\partial \vec{D}}{\partial t} = \frac{\partial \vec{E}}{\partial t} + 4\pi \frac{\partial \vec{P}}{\partial t}$$

with the polarization current density given by

$$\frac{\partial \vec{P}}{\partial t} \equiv \vec{J} = \|\sigma\|\,\vec{E} = n_2\, e\, \vec{v}_2 \,. \tag{A2}$$

n_2 and v_2 are the electron number density and velocity respectively. Insert this into the last equation.

$$\begin{aligned} j\omega\vec{D} &= j\omega\vec{E} + 4\pi\,\|\sigma\|\,\vec{E} \\ \|\varepsilon\| &= 1 + \frac{4\pi\,\|\sigma\|}{j\,\omega} \end{aligned} \tag{A3}$$

The procedure is to find the velocity distribution function for the electrons and use it to calculate $\vec{J}$ from (A2). Then $\|\varepsilon\|$ can be found from (A3), and this result is inserted into (A1) to give a solution for $\frac{c^2}{u^2}$.

The following assumptions are made about the gas.

(a) Lightly ionized.

(b) Neutral molecules are very heavy.

(c) Collisions between charged particles can be ignored.

(d) Elastic collisions.

(e) Heavy neutral particles have a Maxwellian velocity distribution but the electron distribution function is not necessarily Maxwellian.

(f) Homogeneous medium.

(g) Motion of the positive ions due to the fields can be neglected.

The forces on an electron are $e \frac{\vec{v}}{c} \times \vec{H}_o$ due to the earth's field and $e \vec{E}_o \cos \omega t$ due to the electromagnetic wave if we assume that the distance the electrons move is small. The force due to the magnetic field of the wave is a factor v/c smaller than that from the electric field and is neglected.

A solution to the Boltzmann equation is needed.

$$\frac{\partial f_2}{\partial t} + \left[\vec{\Gamma}_2 \cos \omega t + \frac{e}{m_2 c} (\vec{v}_2 \times \vec{H}_o) \right] \nabla_{v_2} f_2$$

$$\iiint (f_1' f_2' - f_1 f_2) \, g \, b \, d \, b \, d \, \varepsilon \, d \, v_1 \qquad \text{(A4)}$$

where $\vec{\Gamma}_2 = \frac{e}{m_2} \vec{E}_o$, $g = \left| \vec{v}_2 - \vec{v}_1 \right| = \left| \vec{v}_2' - \vec{v}_1' \right|$ and b and ε are impact parameters defined by Chapman and Cowling (1960). The primed and unprimed quantities are for after and before the collisions respectively. Quantities with subscript 2 are for electrons and 1 for molecules. The distribution function for the molecules (Maxwellian) is

$$f_1 = n_1 \left[\frac{m_1}{2 \Pi \, k \, T} \right]^{\frac{3}{2}} e^{- \frac{m_1 v_1^2}{2 k T}} \qquad \text{(A5)}$$

f_2 is expanded in the following form, where $f_2^{(o)}$ is isotropic and $\vec{f}_2^{(1)}$ depends on spatial direction.

$$f_2 = f_2^{(o)} + \vec{f}_2^{(1)} \cdot \vec{v}_2$$

$$f_2 = f_2^{(o)} + (\vec{\Gamma}_2 \cdot \vec{v}_2)\,(\alpha_2 \cos \omega t + \beta_2 \sin \omega t) +$$

$$(\vec{H}_o \times \vec{\Gamma}_2) \cdot \vec{v}_2\,(\zeta_2 \cos \omega t + \eta_2 \sin \omega t) + \qquad \text{(A6)}$$

$$[\vec{H}_o \times (\vec{H}_o \times \vec{\Gamma}_2)] \cdot \vec{v}_2\,(\gamma_2 \cos \omega t + \delta_2 \sin \omega t)$$

The constants α_2 through δ_2 depend on the magnitude of v_2.

For a gas satisfying the stated assumptions (Lorentz gas) Chapman and Cowling solve the right side of (A4).

$$R\ H\ S = \frac{kT}{m_1 \lambda} v_2^3 \frac{\partial f_2^{(o)}}{\partial\ v_2} + \frac{m_2\ v_2^4}{m_1 \lambda} f_2^{(o)}$$

$\lambda = \dfrac{v_2}{\nu}$ is the mean free path of an electron where ν is the collision frequency.

Substitute (A7), (A6) and (A5) into the Boltzmann equation (A4). After several pages of algebra, expressions for α_2, β_2, ζ_2, η_2, γ_2, δ_2 and $f_2^{(o)}$ can be found.

If we let the direction of $\vec{f}_2^{(1)}$ be the z axis in velocity space, then

$$n_2\ v_{2x} = \iiint v_2 \sin\ \theta \cos\ \phi\ (f_2^{(o)} + f_2^{(1)}\ v_2 \cos\ \theta)\ v_2^2\ d\ v_2$$

$$\sin\ \theta\ d\ \theta\ d\ \phi = 0$$

$$n_2 v_{2y} = \iiint v_2 \sin\theta \sin\phi (f_2^{(o)} + f_2^{(1)} v_2 \cos\theta) v_2^2 \, d v_2$$

$$\sin\theta \, d\theta \, d\phi = 0$$

$$n_2 v_{2z} = \iiint v_2 \cos\theta (f_2^{(o)} + f_2^{(1)} v_2 \cos\theta) v_2^2 \, d v_2 \sin\theta$$

$$d\theta \, d\phi$$

$$n_2 v_{2z} = \int_o^\infty f_2^{(1)} \frac{4\pi}{3} v_2^4 \, d v_2$$

Therefore the total current is given by

$$\vec{J} = n_2 e \vec{v}_2 = \frac{4\pi}{3} e \int_o^\infty f_2^{(1)} v_2^4 \, d v_2.$$

Put in the explicit expression for $f_2^{(1)}$ given in (A6).

$$\vec{J} = \frac{4\pi}{3} e \left(J_1 \vec{\Gamma}_2 + J_2 (\vec{H}_o \times \vec{\Gamma}_2) + J_3 [\vec{H}_o \times (\vec{H}_o \times \vec{\Gamma}_2)] \right) e^{j\omega t} \quad (A7)$$

where, after writing $\cos\omega t = e^{j\omega t}$ and $\sin\omega t = -j e^{j\omega t}$

$$J_1 = \int_o^\infty (\alpha_2 + \frac{\beta_2}{j}) v_2^4 \, d v_2$$

$$J_2 = \int_o^\infty (\zeta_2 + \frac{\eta_2}{j}) v_2^4 \, d v_2$$

$$J_3 = \int_o^\infty (\gamma_2 + \frac{\delta_2}{j}) v_2^4 \, d v_2$$

The coordinate system usually used for magnetoionic calculations, with the wave propagating in the x direction and $\vec{H}_o$ in the x - z plane, is shown in Figure 46. In this orthogonal coordinate system $\vec{J}$ can be

written

$$\begin{pmatrix} J_x \\ J_y \\ J_z \end{pmatrix} = \frac{4\Pi}{3}\frac{e^2}{m_2} \begin{pmatrix} (J_1 - H_o^2 J_3 \sin^2\phi) & -(H_o J_2 \sin\phi) & (H_o^2 J_3 \cos\phi \sin\phi) \\ (H_o J_2 \sin\phi) & (H_1 - H_o^2 J_3) & (-H_o J_2 \cos\phi) \\ (J_3 H_o^2 \cos\phi \sin\phi) & (H_o J_2 \cos\phi) & (J_1 - J_3 H_o^2 \cos^2\phi) \end{pmatrix} \begin{pmatrix} E_x \\ E_y \\ E_z \end{pmatrix} \quad \text{(A8)}$$

$$\sigma_g = \frac{4\Pi}{3}\frac{e^2}{m_2} \begin{pmatrix} (J_1 - H_o^2 J_3 \sin^2\phi) & -(H_o J_2 \sin\phi) & (H_o^2 J_3 \cos\phi \sin\phi) \\ (H_o J_2 \sin\phi) & (J_1 - H_o^2 J_3) & (-H_o J_2 \cos\phi) \\ (J_3 H_o^2 \cos\phi \sin\phi) & (H_o J_2 \cos\phi) & (J_1 - J_3 H_o^2 \cos^2\phi) \end{pmatrix} \quad \text{(A9)}$$

This is a general expression for the conductivity which holds for any electron velocity distribution. Only when a velocity dependence of the collision frequency is specified can J_1, J_2, and J_3 actually be calculated.

Now, define

$$\varepsilon_I = 1 - \frac{4\Pi j}{3\omega}\omega_o^2 J_1'$$

$$\varepsilon_{II} = -\frac{4\Pi j}{3\omega}\omega_o^2 H_o J_2' \quad \text{(A10)}$$

$$\varepsilon_{III} = \frac{4\Pi j}{3\omega}\omega_o^2 H_o^2 J_3'$$

where $\omega_o^2 = \frac{4\Pi n_2 e^2}{m_2}$, $J_1 = n_2 J_1'$, $J_2 = n_2 J_2'$ and $J_3 = n_2 J_3'$. ε_I, ε_{II}, and ε_{III} are elements of the dielectric tensor associated with the directions of current flow.

From the measurements by Phelps and Pack, we write $\nu = \nu_m \frac{m_2 v_2^2}{2kT}$ where ν_m is the collision frequency for an electron of energy kT. This

is inserted into the expressions for α_2, β_2, ζ_2, η_2, γ_2, and δ_2. After extensive algebra J_1, J_2, and J_3 can be found and putting these into the last equations,

$$\varepsilon_I = (1 - a) - j\, b$$

$$\varepsilon_{II} = 1/2\ (d - f\ ) + \frac{j}{2}\ (e - c)$$

$$\varepsilon_{III} = [a - 1/2\ (c + e)] + j\ [b - 1/2\ (f + d)]$$

where

$$a = \frac{\omega_o^2}{\nu_m^2}\, C\, \frac{3}{2}\left(\frac{\omega}{\nu_m}\right) \qquad d = \frac{5\omega_o^2}{2\omega\nu_m}\, C\, \frac{5}{2}\left(\frac{\omega - s}{\nu_m}\right)$$

$$b = \frac{5\omega_o^2}{2\omega\nu_m}\, C\, \frac{5}{2}\left(\frac{\omega}{\nu_m}\right) \qquad e = \frac{\omega_o^2(\omega+s)}{\omega\nu_m^2}\, C\, \frac{3}{2}\left(\frac{\omega+s}{\nu_m}\right) \qquad \text{(A12)}$$

$$c = \frac{\omega_o^2(\omega-s)}{\omega\nu_m^2}\, C\, \frac{3}{2}\left(\frac{\omega-s}{\nu_m}\right) \qquad f = \frac{5\omega_o^2}{2\omega\nu_m}\, C\, \frac{5}{2}\left(\frac{\omega+s}{\nu_m}\right)$$

$s = \frac{eH_o}{m\,c}$ is the electron gyrofrequency and

$$C_p(x) = \frac{1}{p!}\int_o^\infty \frac{\varepsilon^p\, e^{-\varepsilon} d\varepsilon}{\varepsilon^2 + x^2} \quad \text{where } \varepsilon = \frac{m_2\, v_2^2}{2\, k\, T} \quad .$$

These integrals have been tabulated by Dingle, Arndt and Roy (1957) and are known as Dingle integrals.

The dielectric tensor is given in terms of the conductivity by (A3), where $\|\sigma\|$ is given by (A9). Substituting (A9) into (A3), and evaluating the tensor in terms of ε_I, ε_{II}, and ε_{III},

$$\|\varepsilon\| = \begin{pmatrix} (\varepsilon_I + \varepsilon_{III} \sin^2 \phi) & (-\varepsilon_{II} \sin \phi) & (-\varepsilon_{III} \sin \phi \cos \phi) \\ (\varepsilon_{II} \sin \phi) & (\varepsilon_I + \varepsilon_{II}) & (-\varepsilon_{II} \cos \phi) \\ (-\varepsilon_{III} \sin \phi \cos \phi) & (\varepsilon_{II} \cos \phi) & (\varepsilon_I + \varepsilon_{III} \cos^2 \phi) \end{pmatrix} \quad \text{(A13)}$$

$$\|\varepsilon\| = \begin{pmatrix} \varepsilon_{x\,x} & \varepsilon_{x\,y} & \varepsilon_{x\,z} \\ \varepsilon_{y\,x} & \varepsilon_{y\,y} & \varepsilon_{y\,z} \\ \varepsilon_{z\,x} & \varepsilon_{z\,y} & \varepsilon_{z\,z} \end{pmatrix} \quad \text{(A14)}$$

A recapitulation is in order. A solution of the Boltzmann equation for the electron velocity distribution function allowed an expression for the polarization current to be written. This expression was rewritten in the form $\vec{J} = \|\sigma\| \vec{E}$ in equation (A8), from which the conductivity tensor could be recognized. J_1, J_2, and J_3 depend on six constants α_2, β_2, ζ_2, η_2, γ_2, and δ_2 which could not be calculated until the velocity dependence of the collision frequency was specified. This specification was made by using the results of Phelps and Pack which give $\nu = \nu_m \frac{m_2 v_2^2}{2 k T}$. α_2 through δ_2 were then calculated in closed form which then specified J_1, J_2, and J_3, from which in turn the explicit form of the conductivity tensor was known. By using (A3) the dielectric tensor was then written. To simplify this tensor, quantities ε_I, ε_{II}, and ε_{III} were defined in terms of J_1, J_2, and J_3, and resulted in the simplified expressions given by (A11) and (A12). (A13) is the dielectric tensor written interms of ε_I, ε_{II}, and ε_{III}.

Now that $\|\varepsilon\|$ is known, equation (A1) is written in component form. In order to have non-trivial solutions for E_x, E_y, and E_z, $\frac{c^2}{u^2}$ must be chosen so that the determinant of the coefficients equal 0.

$$\begin{vmatrix} \varepsilon_{x\,x} & \varepsilon_{x\,y} & \varepsilon_{x\,z} \\ \varepsilon_{y\,x} & -\frac{c^2}{u^2} + \varepsilon_{y\,y} & \varepsilon_{y\,z} \\ \varepsilon_{z\,x} & \varepsilon_{z\,y} & -\frac{c^2}{u^2} + \varepsilon_{z\,z} \end{vmatrix} = 0$$

Solving this, and substituting in from (A13) the explicit expressions for $\varepsilon_{x\,x}$ through $\varepsilon_{z\,z}$,

$$\frac{c^2}{u^2} = \frac{A + B \sin^2 \phi \pm \sqrt{B^2 \sin^4 \phi - C^2 \cos^2 \phi}}{D + E \sin \phi} \qquad \text{(A15)}$$

where $A = 2\varepsilon_I (\varepsilon_I + \varepsilon_{III})$

$B = \varepsilon_{III} (\varepsilon_I + \varepsilon_{III}) + \varepsilon_{II}^2$

$C = 2\varepsilon_I \varepsilon_{II}$

$D = 2 \varepsilon_I$

$E = 2 \varepsilon_{III}$

The complex index of refraction can be written in terms of the real refractive index and absorption factor as

$$\frac{c^2}{u^2} = \left(n - \frac{j \kappa c}{\omega} \right)^2 = L - j M$$

where L and M are the real and imaginary parts of (A15). Note that there are two values for each. Then,

$$n = \sqrt{\frac{L + \sqrt{L^2 + M^2}}{2}}$$

$$\frac{\kappa c}{\omega} = \sqrt{\frac{-L + \sqrt{L^2 + M^2}}{2}}$$

APPENDIX B

CALCULATION OF (n_1-n_2) SIGN REVERSAL CONDITIONS

The intention of this work is to derive from the Generalized Appleton-Hartree equation simplified approximate expressions for conditions which must hold for n_1 to equal n_2. This is done for two cases, where $B \sin^2 \phi > C \cos \phi$ (quasi-transverse) and where $C \cos \phi > B \sin^2 \phi$ (quasi-longitudinal). In all cases it was assumed that $\nu_m^2 >> \omega_o^2$, a condition which holds well in the lower D region. Although successive approximations have been made, typical values for quantities have been calculated at each stage and these indicate that the approximations are valid. In addition the approximate calculation of necessary conditions matches quite well the conditions derived by using the exact equations.

The method is to expand the radical in equation (A15), and then to make approximations until a workable solution results.

1. Quasi-transverse Case

In this case the first term of the radical is large.

$$\text{Radical} \approx B \sin^2 \phi - \frac{1}{2} \frac{C^2 \cos^2 \phi}{B \sin^2 \phi}$$

Then

$$\frac{c^2}{u^2} \approx \frac{A + B \sin^2 \phi \pm B \sin^2 \phi \mp \frac{1}{2} \frac{C^2 \cos^2 \phi}{B \sin^2 \phi}}{D + E \sin^2 \phi} \qquad \text{(B1)}$$

$$\left(\frac{c^2}{u^2}\right)_1 \approx \frac{A + \frac{1}{2}\ \frac{C^2 \cos^2 \phi}{B \sin^2 \phi}}{D + E \sin^2 \phi}$$

Assume the second term in the numerator is small.

$$\left(\frac{c^2}{u^2}\right)_1 \approx \frac{2\ \varepsilon_I\ (\varepsilon_I + \varepsilon_{III})}{2\ \varepsilon_I + 2\ \varepsilon_{III} \sin^2 \phi}$$

$$\left(\frac{c^2}{u^2}\right)_1 \approx \frac{\varepsilon_I\ (\varepsilon_I + \varepsilon_{III})}{\varepsilon_I + \varepsilon_{III} - \varepsilon_{III} \cos^2 \phi}$$

The last term in the denominator is small.

$$\left(\frac{c^2}{u^2}\right)_1 \approx \varepsilon_I$$

$$\left(\frac{c^2}{u^2}\right)_1 \approx (1 - a) - j\ b$$

The real part is much larger than the imaginary part; under these conditions

$$n_1^2 \approx 1 - a \qquad \text{(B2)}$$

From (B1), neglecting the last term in the numerator,

$$\left(\frac{c^2}{u^2}\right)_2 \approx \frac{A + 2\ B \sin^2 \phi}{D + E \sin^2 \phi}$$

$$\left(\frac{c^2}{u^2}\right)_2 \approx \frac{2\ \varepsilon_I(\varepsilon_I+\varepsilon_{III}) + 2\ \varepsilon_{III}(\varepsilon_I+\varepsilon_{III})\ \sin^2\phi + 2\ \varepsilon_{II}^2(\varepsilon_I + \varepsilon_{III})\ \sin^2\phi}{2\ \varepsilon_I\ +\ 2\ \varepsilon_{III}\ \sin^2\phi}$$

ε_{II}^2 is very small compared with ε_I or ε_{III}.

$$\left(\frac{c^2}{u^2}\right)_2 \approx \frac{(\varepsilon_I + \varepsilon_{III})\ (2\ \varepsilon_I + 2\ \varepsilon_{III}\ \sin^2\phi)}{2\ \varepsilon_I + 2\ \varepsilon_{III}\ \sin^2\phi}$$

$$\left(\frac{c^2}{u^2}\right)_2 \approx \varepsilon_I + \varepsilon_{III}$$

$$\left(\frac{c^2}{u^2}\right)_2 \approx (1 - a) + \left[a - \frac{1}{2}(c + e)\right] - \frac{j}{2}(f + d)$$

Again the real part is large compared with the imaginary part, and

$$n_2^2 \approx \left[(1 - a) + a - \frac{1}{2}(c + e)\right] \qquad \text{(B3)}$$

To make (B2) and (B3) equal, we must require that

$$2\ a = c + e \qquad \text{(B4)}$$

where a, c and e are defined by equations (A12).

2. Quasi-longitudinal Case

The last term in the radical is assumed large.

$$\text{Radical} \approx j\left[C\cos\phi - 1/2\ \frac{B^2\sin^4\phi}{C\cos\phi}\right]$$

$$\frac{c^2}{u^2} \approx \frac{A + B\sin^2\phi \pm j\ C\cos\phi \mp 1/2\ \frac{B^2\sin^4\phi}{C\cos\phi}}{D + E\sin^2\phi} \qquad \text{(B5)}$$

Now assume all terms containing $\sin^2 \phi$ are small.

$$\left(\frac{c^2}{u^2}\right)_1 \approx \frac{A + j\ C \cos \phi}{D}$$

$$\left(\frac{c^2}{u^2}\right)_1 \approx \varepsilon_I + \varepsilon_{III} + j\ \varepsilon_{II} \cos \phi$$

$$\left(\frac{c^2}{u^2}\right)_1 \approx [1 - 1/2\ (c + e) - (e - c) \cos \phi] -$$

$$j\ [1/2\ (f + d) - (d - f) \cos \phi]$$

The real part is much larger than the imaginary.

$$n_1^2 \approx [1 - 1/2\ (c + e) - (e - c) \cos \phi] \qquad \text{(B6)}$$

From (B5),

$$\left(\frac{c^2}{u^2}\right)_2 \approx \frac{A - j\ C \cos \phi}{D}$$

$$\left(\frac{c^2}{u^2}\right)_2 \approx [\varepsilon_I + \varepsilon_{III}] - j\ \varepsilon_{II} \cos \phi$$

$$\left(\frac{c^2}{u^2}\right)_2 \approx [1 - 1/2\ (c + e) + (e - c) \cos \phi] - j\ [1/2\ (f + d) +$$

$$(d - f) \cos \phi]$$

Once again the real part is large.

$$n_2^2 \approx [1 - 1/2\ (c + e) + (e - c) \cos \phi] \qquad \text{(B7)}$$

To make $n_1 = n_2$, we must set

$$e = c. \qquad \text{(B8)}$$

A criterion for the range of ϕ over which each case is valid is that the ratio $\frac{B \sin^2 \phi}{C \cos \phi}$ should be greater than 3 or less than 1/3 for quasi-transverse or quasi-longitudinal conditions respectively. This range should be calculated for the specific geographical location where these results are to be used. For one typical case investigated, the quasi-longitudinal conditions were valid for $0 < \phi < 24$ degrees and the quasi-transverse from $63 < \phi < 90$ degrees.

APPENDIX C

COMPUTER PROGRAMS

The tables list IBM 1130 Fortran IV source programs for the Generalized Appleton-Hartree equation. The first program (Table 1) was used for calculating the indices of refraction and absorption coefficients under various assumed ionospheric conditions. The computations were carried out for two wave frequencies at three different geographical locations for each input card. The inputs needed are ω, ϕ, ω_o^2, ν_m, s and the altitude.

The second program (Table 2) begins with an assumed value for ω_o^2 and alters it by an iterative process until the computed $(n_1 - n_2)$ matches the observed value. One of the statements 3 should be removed, which depends on whether ω_o^2 is to be altered on 10% or 1% steps. The inputs needed are ω, ϕ, ω_o^2, ν_m, s, altitude and the experimental value of $(n_1 - n_2)$.

Table 3 lists a function subprogram for computing Dingle integrals (Hara, 1963) which must be used in conjunction with either of the other programs.

The following notation was used in the above programs. ω = OMEGA or OMEG, ϕ = PHI or PH, total number of statement 2 cards = N, ω_o^2 = OMO2, ν_m = XNU, s = S, altitude = H, $(n_1 - n_2)_{exp}$ = XNEXP, n_1 = XN1, n_2 = XN2, $\frac{c\kappa_1}{\omega}$ = SK1, $\frac{c\kappa_2}{\omega}$ = XK2, N_e = ELDEN and C_y (x) = CC(X,Y).

Table 4 is a program for computing solar zenith angles. The inputs needed are geographic latitude, solar declination and date. The following notation was used: geographic latitude = XLAT, total number of statement 1 cards = J, solar declination = DECL, and the date = IDATE.

TABLE I

GENERALIZED APPLETON-HARTREE CALCULATIONS L. LARSON

```
    DIMENSION OMEGA(2),PHI(3),AX(2),BX(2),CX(2),DX(2),EX(2),SX(3)
    READ(2,99)
99  FORMAT(49H)
    WRITE(3,99)
    PI=3.14159
    M=0
 1  READ(2,101)OMEGA(1),OMEGA(2),PHI(1),PHI(2),PHI(3),N
 2  READ(2,102)OMO2,XNU,H,SX(1),SX(2),SX(3)
    M=M+1
    DO 6 J=1,2
    OMEG=OMEGA(J)
    DO 6 K=1,3
    PH=PHI(K)
    S=SX(K)
    ARG1=OMEG/XNU
    ARG2=S/XNU
    ARG3=ARG1-ARG2
    ARG4=ARG1+ARG2
    PROD=OMEG*XNU
    A=OMO2/XNU*CC(ARG1,1.5)/XNU
    B=2.5*OMO2/PROD*CC(ARG1,2.5)
    C=OMO2/PROD*ARG3*CC(ABS(ARG3),1.5)
    D=2.5*OMO2/PROD*CC(ABS(ARG3),2.5)
    E=OMO2/PROD*ARG4*CC(ARG4,1.5)
    F=2.5*OMO2/PROD*CC(ARG4,2.5)
    WRITE(3,103)A,B,C,D,E,F
    E1R=1.-A
    E1I=-B
    E2R=.5*(F-D)
    E2I=.5*(C-E)
    E3R=A-.5*(C+E)
    E3I=B-.5*(F+D)
    AX(1)=2.*(E1R*(E1R+E3R)-E1I*(E1I+E3I))
    AX(2)=2.*(E1I*(E1R+E3R)+E1R*(E1I+E3I))
    BX(1)=(E3R+E1R)*E3R-E3I*(E1I+E3I)+E2R*E2R-E2I*E2I
    BX(2)=E3I*(E1R+E3R)+(E1I+E3I)*E3R+2.*E2I*E2R
    CX(1)=2.*(E1R*E2R-E1I*E2I)
    CX(2)=2.*(E1I*E2R+E1R*E2I)
    DX(1)=2.*E1R
    DX(2)=2.*E1I
    EX(1)=2.*E3R
    EX(2)=2.*E3I
    SNPH=SIN(PH)**2
    CSPH=COS(PH)**2
    ROOTR=SNPH*SNPH*(BX(1)*BX(1)-BX(2)*BX(2))-CSPH*(CX(1)*CX(1)-CX(2)*
   1CX(2))
    ROOTI=2.*(SNPH*SNPH*BX(1)*BX(2)-CSPH*CX(1)*CX(2))
    AB=SQRT(ROOTR*ROOTR+ROOTI*ROOTI)
    ANG=ATAN(ROOTI/ROOTR)
```

```
      AB=SQRT(AB)
      IF(ROOTR)3,4,4
    3 ANJ=ANG+PI
      GO TO 7
    4 ANJ=ANG
      GO TO 7
    7 IF(ANJ)8,5,5
    8 ANJ=ANJ+2.*PI
      GO TO 5
    5 ANG1=ANJ*.5
      SAR=AB*COS(ANG1)
      SAI=AB*SIN(ANG1)
      AA=AX(1)+SNPH*BX(1)
      BB=AX(2)+SNPH*BX(2)
      S1R=AA+SAR
      S1I=BB+SAI
      S2R=AA-SAR
      S2I=BB-SAI
      DR=DX(1)+SNPH*EX(1)
      DI=DX(2)+SNPH*EX(2)
      AC=(DR*DR+DI*DI)
      XL1R=(S1R*DR+S1I*DI)/AC
      XL1I=(S1I*DR-S1R*DI)/AC
      XL2R=(S2R*DR+S2I*DI)/AC
      XL2I=(S2I*DR-S2R*DI)/AC
      SQF1=SQRT(XL1R*XL1R+XL1I*XL1I)
      SQF2=SQRT(XL2R*XL2R+XL2I*XL2I)
      XN1=SQRT(ABS((XL1R+SQF1)*.5))
      XN2=SQRT(ABS((XL2R+SQF2)*.5))
      XK1=SQRT(ABS((-XL1R+SQF1)*.5))
      XK2=SQRT(ABS((-XL2R+SQF2)*.5))
      WRITE(3,103)OMEG,PH,H
      WRITE(3,103)XN1,XN2,XK1,XK2
    6 WRITE(3,103)XL1R,XL1I,XL2R,XL2I
      IF(N-M)15,15,2
   15 CALL EXIT
  101 FORMAT(E6.2,2X,E7.2,2X,3(F5.4,2X),I2)
  102 FORMAT(E7.1,2X,E7.3,2X,F5.1,2X,3(E6.2,2X))
  103 FORMAT(1H ,5(2X,E14.7))
      END
```

TABLE 2

EXP IONOSPHERIC CALCULATIONS BY APPLETON-HARTREE METHOD L. LARSON

```
      DIMENSION AX(2),BX(2),CX(2),DX(2),EX(2)
      READ(2,99)
   99 FORMAT(49H)
      WRITE(3,99)
      PI=3.14159
      M=0
      READ(2,101)OMEG,PH,N
    2 READ(2,102)OMO2,XNU,S,H,XNEXP
      M=M+1
      DO 7 J=1,25
    3 OMO2=OMO2 + .01*OMO2
    3 OMO2=OMO2 + .1*OMO2
      ARG1=OMEG/XNU
      ARG2=S/XNU
      ARG3=ARG1-ARG2
      ARG4=ARG1+ARG2
      PROD=OMEG*XNU
      A=OMO2/XNU*CC(ARG1,1.5)/XNU
      B=2.5*OMO2/PROD*CC(ARG1,2.5)
      C=OMO2/PROD*ARG3*CC(ABS(ARG3),1.5)
      D=2.5*OMO2/PROD*CC(ABS(ARG3),2.5)
      E=OMO2/PROD*ARG4*CC(ARG4,1.5)
      F=2.5*OMO2/PROD*CC(ARG4,2.5)
      E1R=1.-A
      E1I=-B
      E2R=.5*(F-D)
      E2I=.5*(C-E)
      E3R=A-.5*(C+E)
      E3I=B-.5*(F+D)
      AX(1)=2.*(E1R*(E1R+E3R)-E1I*(E1I+E3I))
      AX(2)=2.*(E1I*(E1R+E3R)+E1R*(E1I+E3I))
      BX(1)=(E3R+E1R)*E3R-E3I*(E1I+E3I)+E2R*E2R-E2I*E2I
      BX(2)=E3I*(E1R+E3R)+(E1I+E3I)*E3R+2.*E2I*E2R
      CX(1)=2.*(E1R*E2R-E1I*E2I)
      CX(2)=2.*(E1I*E2R+E1R*E2I)
      DX(1)=2.*E1R
      DX(2)-2.*E1I
      EX(1)=2.*E3R
      EX(2)=2.*E3I
      SNPH=SIN(PH)**2
      CSPH=COS(PH)**2
      ROOTR=SNPH*SNPH*(BX(1)*BX(1)-BX(2)*BX(2))-CSPH*(CX(1)*CX(1)-CX(2)*
     1CX(2))
      ROOTI=2.*(SNPH*SNPH*BX(1)*BX(2)-CSPH*CX(1)*CX(2))
      AB=SQRT(ROOTR*ROOTR+ROOTI*ROOTI)
      ANG=ATAN(ROOTI/ROOTR)
      AB=SQRT(AB)
      IF(ROOTR)4,5,5
```

```
 4  ANJ=ANG+PI
    GO TO 10
 5  ANJ=ANG
    GO TO 10
10  IF(ANJ)11,6,6
11  ANJ=ANJ+2.*PI
    GO TO 6
 6  ANG1=ANJ*.5
    SAR=AB*COS(ANG1)
    SAI=AB*SIN(ANG1)
    AA=AX(1)+SNPH*BX(1)
    BB=AX(2)+SNPH*BX(2)
    S1R=AA+SAR
    S1I=BB+SAI
    S2R=AA-SAR
    S2I=BB-SAI
    DR=DX(1)+SNPH*EX(1)
    DI=DX(2)+SNPH*EX(2)
    AC=(DR*DR+DI*DI)
    XL1R=(S1R*DR+S1I*DI)/AC
    XL1I=(S1I*DR-S1R*DI)/AC
    XL2R=(S2R*DR+S2I*DI)/AC
    XL2I=(S2I*DR-S2R*DI)/AC
    SQF1=SQRT(XL1R*XL1R+XL1I*XL1I)
    SQF2=SQRT(XL2R*XL2R+XL2I*XL2I)
    XN1=SQRT(ABS((XL1R+SQF1)*.5))
    XN2=SQRT(ABS((XL2R+SQF2)*.5))
    XK1=SQRT(ABS((-XL1R+SQF1)*.5))
    XK2=SQRT(ABS((-XL2R+SQF2)*.5))
    XNCOM=XN1-XN2
    IF (XK2) 12,12,13
12  XK2=.0000001
13  XKCOM=XK1/XK2
    XNDIF=XNCOM-XNEXP
    IF(XNEXP)15,14,14
14  IF(XNDIF) 7,7,8
15  IF(XNDIF) 8,7,7
 7  CONTINUE
    GO TO 9
 8  ELDEN=3.1429E-10*OMO2
    WRITE(3,103)OMO2,ELDEN,H
    WRITE(3,103)PH,OMEG,XKCOM
    GO TO 16
 9  WRITE(3,104)
16  IF(N-M)17,17,2
17  CALL EXIT
101 FORMAT (E7.2,2X,F5.3,2X,I2)
102 FORMAT (E7.1,2X,E7.3,2X,E6.2,2X,F5.1,2X,F7.5)
103 FORMAT(1H ,5(2X,E14.7))
104 FORMAT(1H ,12H GUESS AGAIN)
    END
```

TABLE 3

FUNCTION SUBPROGRAM CC(X,Y)

```
      FUNCTION CC(X,Y)
      IF (Y-2.5)1,2,1
1     XNUM=(((X+2.4653115E1)*X+1.1394160E2)*X+1.1287513E1)*X+2.3983474E
     1-2
      XDEN=((((X+2.4656819E1)*X+1.2049512E2)*X+2.8958085E2)*X+1.492125
     14E2)*X+9.387732)*X+1.8064128E-2
3     CC=XNUM/XDEN
      RETURN
2     XNUM=((X+6.6945939)*X+1.6901002E1)*X+1.1630641
      XDEN=(((X+6.6314497)*X+3.5355257E1)*X+6.8920505E1)*X+6.4093464E1
     1)*X+4.3605732
      GO TO 3
      END
```

TABLE 4

ZENITH ANGLE CALCULATIONS

```
      DIMENSION PH(5)
      READ (2,99)
      WRITE (3,99)
      READ (2,101)XLAT,J
      I=0
      PH(1)=.0000
      PH(2)=.2618
      PH(3)=.5236
      PH(4)=.7854
      PH(5)=1.0472
      THET=XLAT*.01745
    1 READ(2,102)DECL,IDATE
      I=I+1
      DELT=DECL*.01745
      DO 2 K=1,5
      PHI=PH(K)
      COKI=SIN(DELT)*SIN(THET)+COS(DELT)*COS(THET)*COS(PHI)
      SIKI=SQRT(1-(COKI*COKI))
      XKI1=ATAN(SIKI/COKI)
      XKI=XKI1*57.3
      PHIT=PHI*3.82
    2 WRITE(3,103)COKI,PHIT,IDATE,XKI
      IF(J-I)3,3,1
    3 CALL EXIT
   99 FORMAT(1H ,50H)
  101 FORMAT(F5.1,2X,I2)
  102 FORMAT(F6.2,2X,I4)
  103 FORMAT(1H ,F6.4,2X,F3.1,2X,I4,2X,F5.1)
      END
```

FIGURE CAPTIONS

Figure 1 Mean mid-day electron electron density profile for the lower ionosphere (Van Zandt and Knecht, 1964).

Figure 2 Schematic diagram of a 3.385 MHz exciter to drive a Gates HFL 1000 linear amplifier.

Figure 3 Block diagram for the rocket-borne receiver.

Figure 4 Receiver schematic diagram (2 diagrams).

Figure 5 Photograph of a completed receiver and mounting deck.

Figure 6 Simplified schematic diagram for the ultraviolet electronics.

Figure 7 Complete schematic diagram for the ultraviolet electronics.

Figure 8 Photograph of a completed ultraviolet experiment.

Figure 9 Photograph of an ultraviolet photoionization chamber (foreground) and a Geiger tube for detecting 2 to 12 A. X-rays.

Figure 10 A typical spectral response curve for a photoionization chamber with a BaF_2 window and a filling gas of $(C_2H_5)_2$ S (Stober, Scolnik and Hennes, 1963).

Figure 11 Schematic diagram of the system used to calibrate the ultraviolet detectors.

Figure 12 A typical response curve for a Geiger tube with a 1.5 mg/cm^2 mica window and an argon plus halogen filling.

Figure 13 Photograph of an X-ray detector deck. The unit in the foreground is the solar aspect sensor.

Figure 14 Schematic diagram of the electronics associated with the 2 to 12 A. Geiger tube.

Figure 15 Portion of a typical flight record. Shown, from top to bottom, are the magnetic aspect sensor, 1.005 MHz receiver, 3.385 MHz receiver, magnetic aspect sensor, low gain U.V. deck, high gain U.V. deck and solar aspect sensor signals. At the bottom is a timing code supplied by the ground station.

Figure 16 Diagram used to compute the relationship between Faraday rotation and $(n_1 - n_2)$. The wave, which propagates in a direction perpendicular to the paper, is made up of two circularly polarized components. After the wave has travelled a distance dh, one circular component has rotated through an angle Ω_1, the other has rotated through Ω_2 and the composite has rotated through $d\Omega$.

Figure 37 A comparison of the measured electron density profiles from 76 to 104 KM.

Figure 38 Calculated values of $(n_1 - n_2)$ vs. ν_m/ω to show $(n_1 - n_2)$ sign reversal, which indicates how the effect depends on the angle ϕ between the propagation direction and the earth's field.

Figure 39 Calculated values of $(n_1 - n_2)$ vs. ν_m/ω to show $(n_1 - n_2)$ sign reversal for the longitudinal propagation case, which indicates how the effect depends on the ratio s/ω.

Figure 40 Comparison of the Faraday rotation for both 1.005 and 3.385 MHz data for the 12° S. flight, which shows that the direction of rotation reversed at the same altitude for both frequencies.

Figure 41. Comparison of the Faraday rotation for both 1.005 and 3.385 MHz data for the Wallops 1966 flight, which shows that the direction of rotation reversed at the same altitude for both frequencies.

Figure 42 X-ray and charged particle data for the Churchill flight.

Figure 43 X-ray and charged particle data for the Wallops 1966 flight.

Figure 44 Comparison of the measured and computed electron density profiles for the Churchill flight.

Figure 45 Comparison of the measured and computed electron density profiles for the Wallops 1966 flight.

Figure 46 Coordinate system usually used in magnetoionic work. The wave propagates along the X direction, and the earth's field lies in the X - z plane at an angle ϕ with the propagation direction.

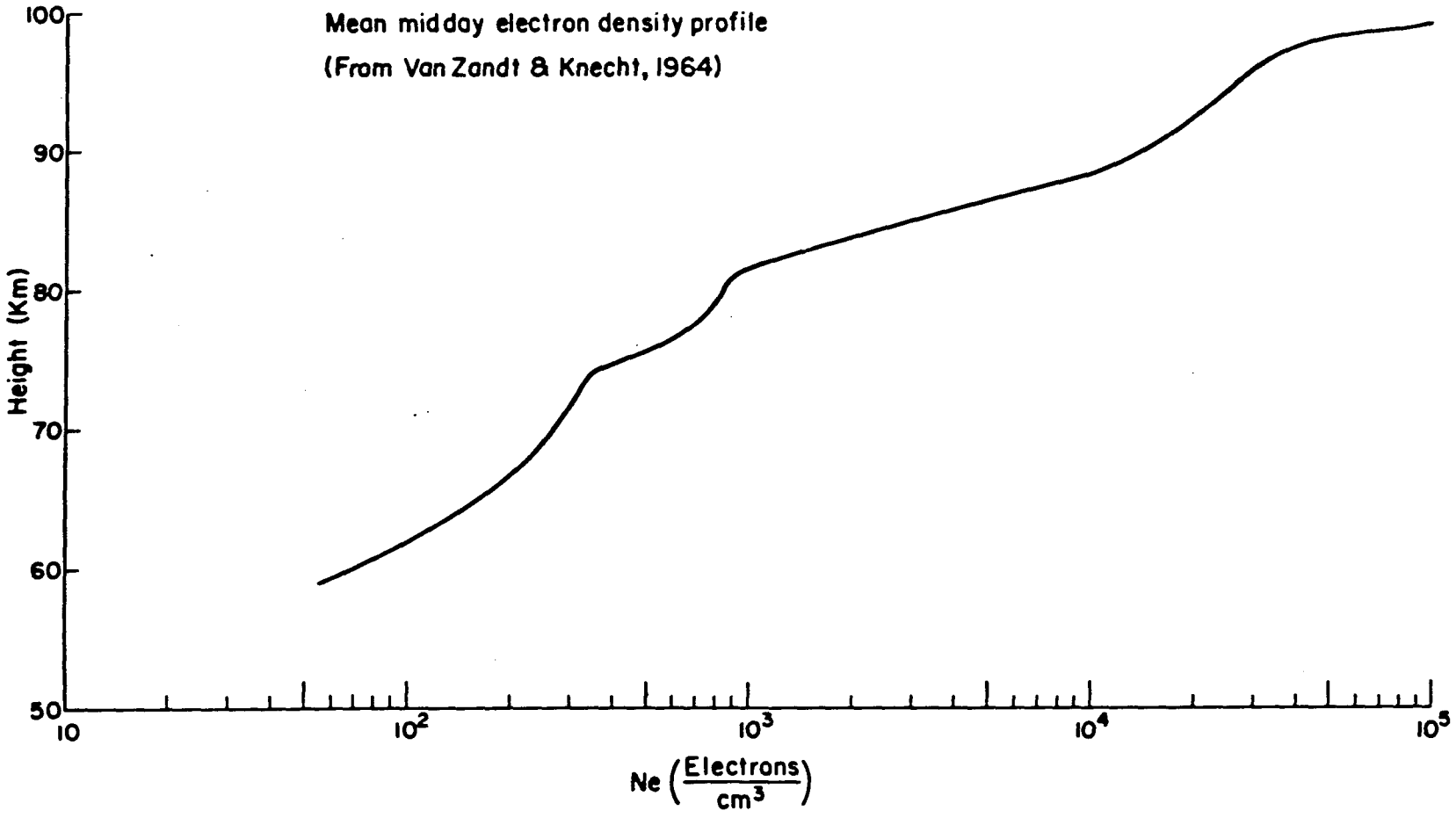
Mean midday electron density profile
(From Van Zandt & Knecht, 1964)
100
90
80
70
60
50
Height (Km)
10
10^2
10^3
10^4
10^5
Ne $\left(\frac{\text{Electrons}}{\text{cm}^3}\right)$

FIGURE 1

EXCITER TO DRIVE GATES HFL 1000 AMPLIFIER

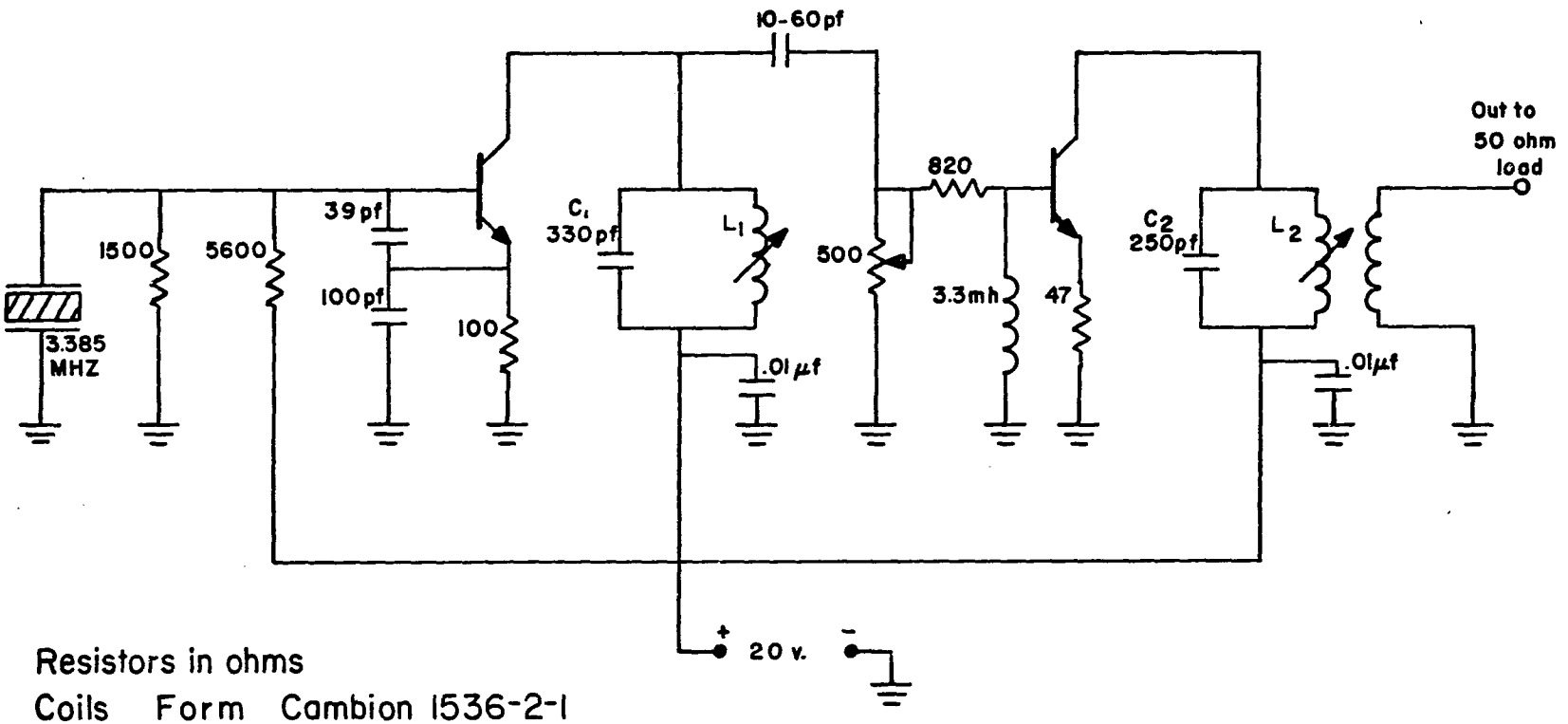

Resistors in ohms

Coils Form Cambion 1536-2-1

35 turns #30 wire
Link 8 turns

Transistors are 2N697

FIGURE 2

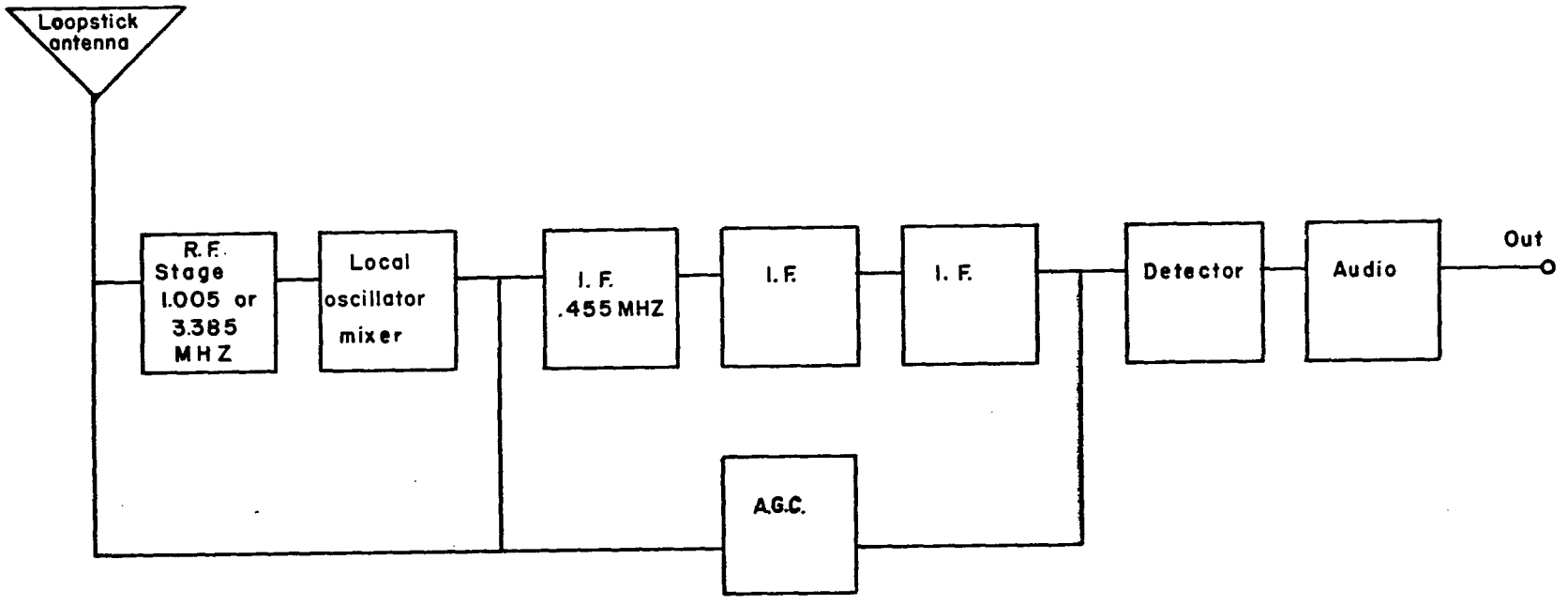

RECEIVER BLOCK DIAGRAM

FIGURE 3

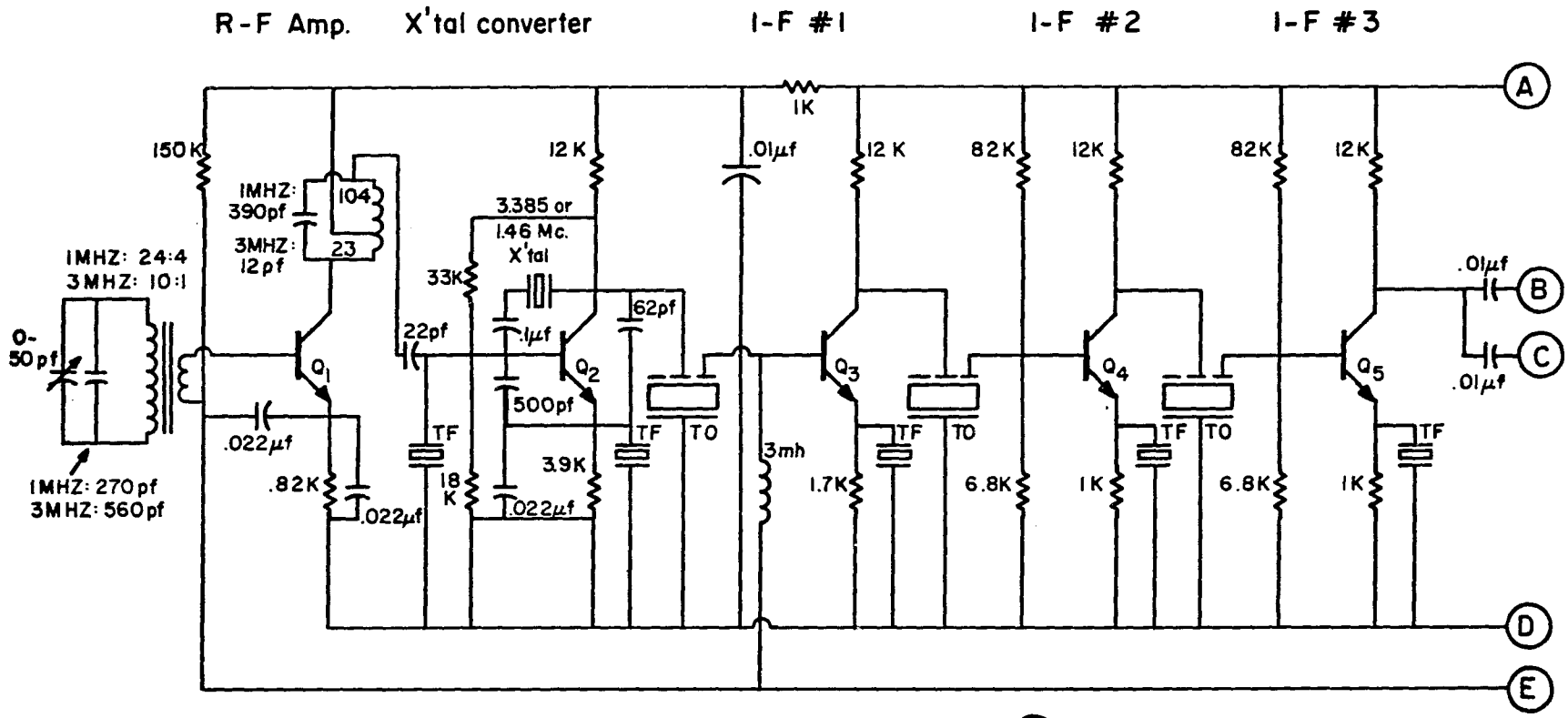

Q_1, Q_2 2N916

Q_3, Q_4, Q_5 2N338

TO are TO-02A transfilters

TF are TF-01A bypass filters

(A) V_{CC} +20v.

(B) I-F output to 2nd detector

(C) I-F output to AGC detector

(D) Electric ground

(E) AVC line

RECEIVER SCHEMATIC

FIGURE 4

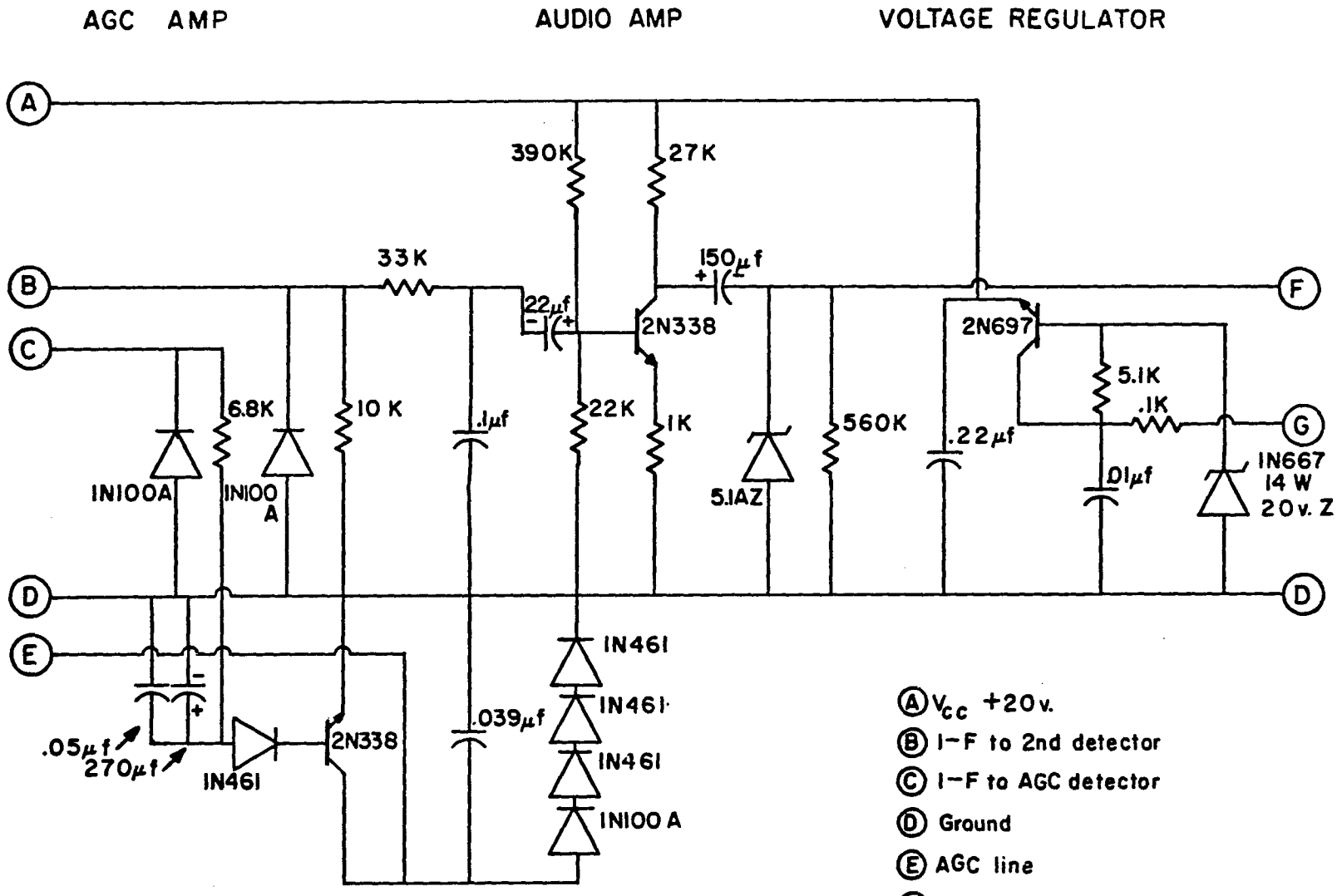

RECEIVER SCHEMATIC

FIGURE 4

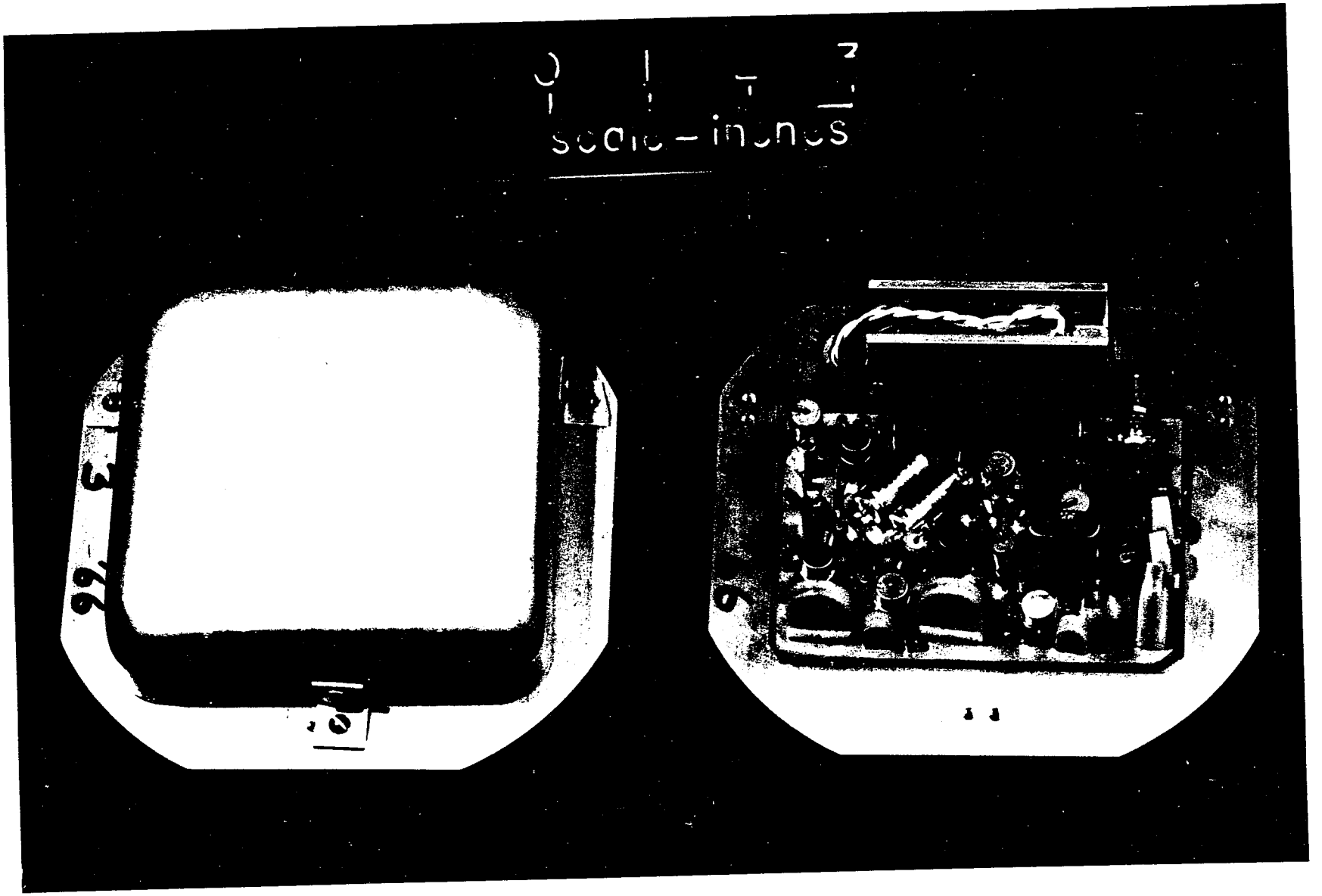

FIGURE 5

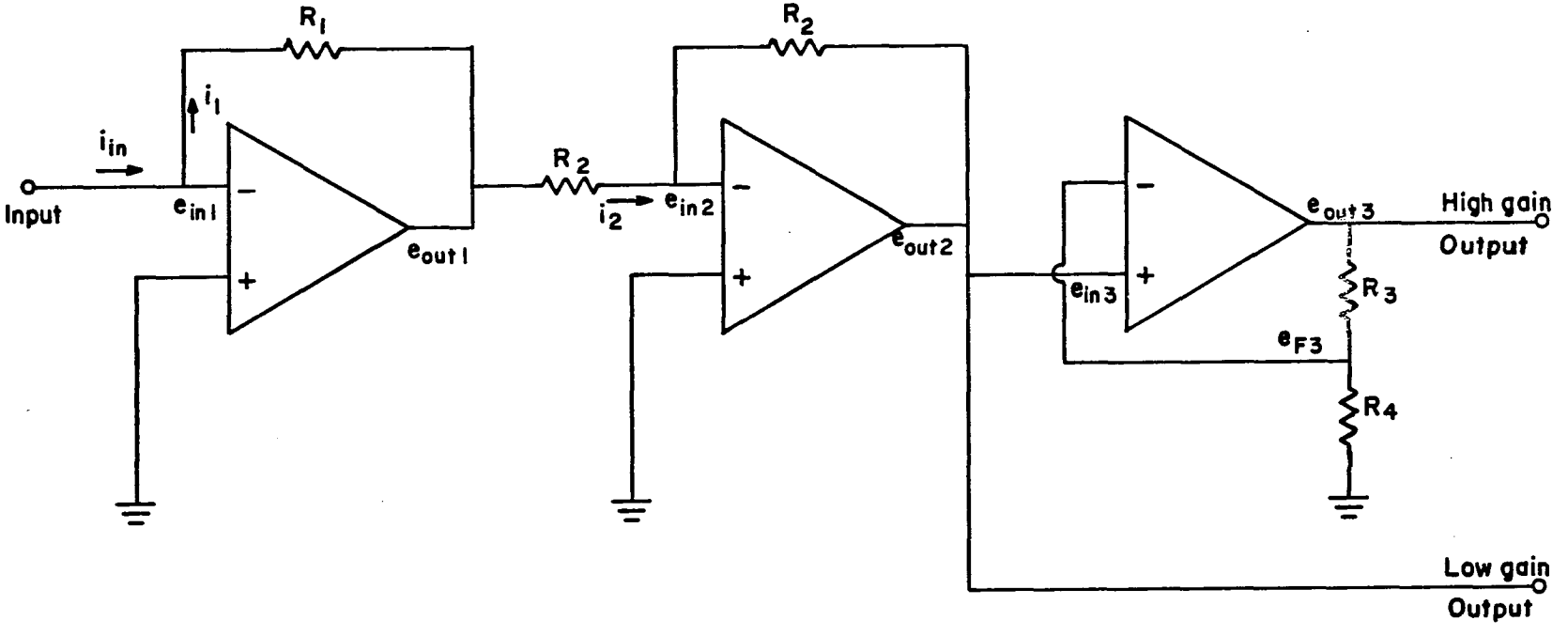
R1
i1
iin
Input
ein1
eout1
R2
i2
ein2
R2
eout2
ein3
eout3
High gain
Output
R3
eF3
R4
Low gain
Output

FIGURE 6

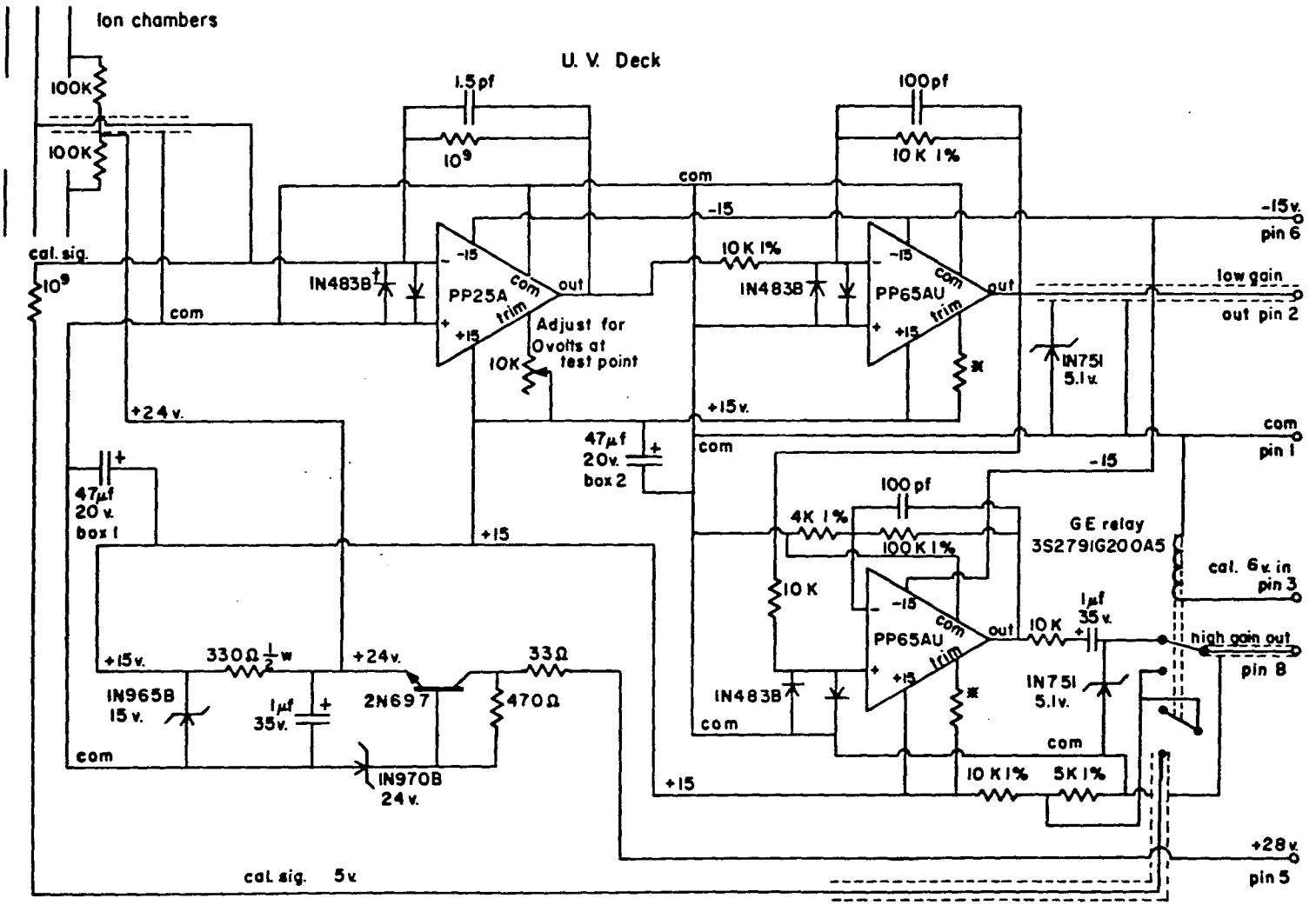

All resistors ¼ w. 10% unless specified

All 1% resistors .1 w.

* Use resistor specified on unit

+ Select for high back resistance

FIGURE 7

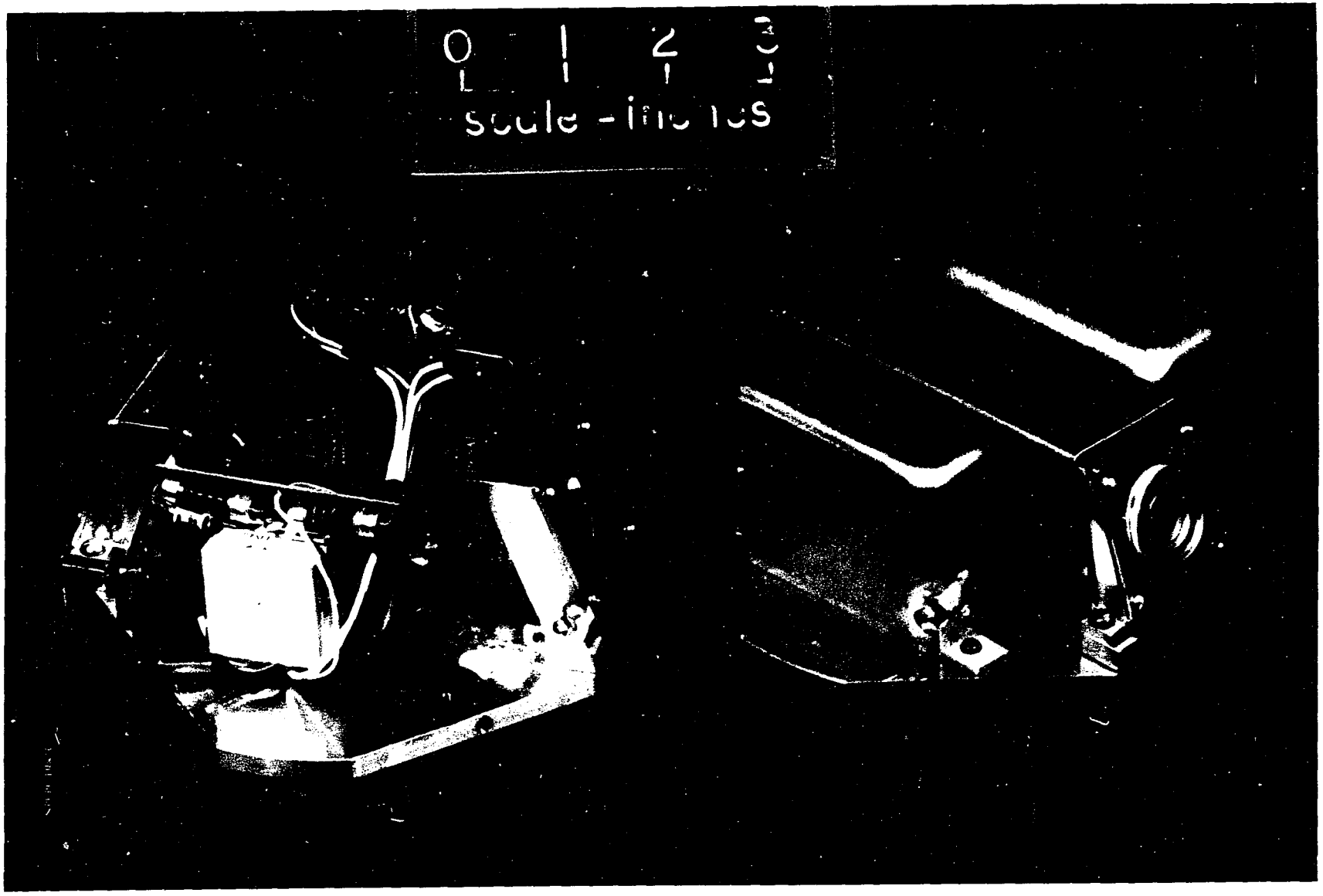

FIGURE 8

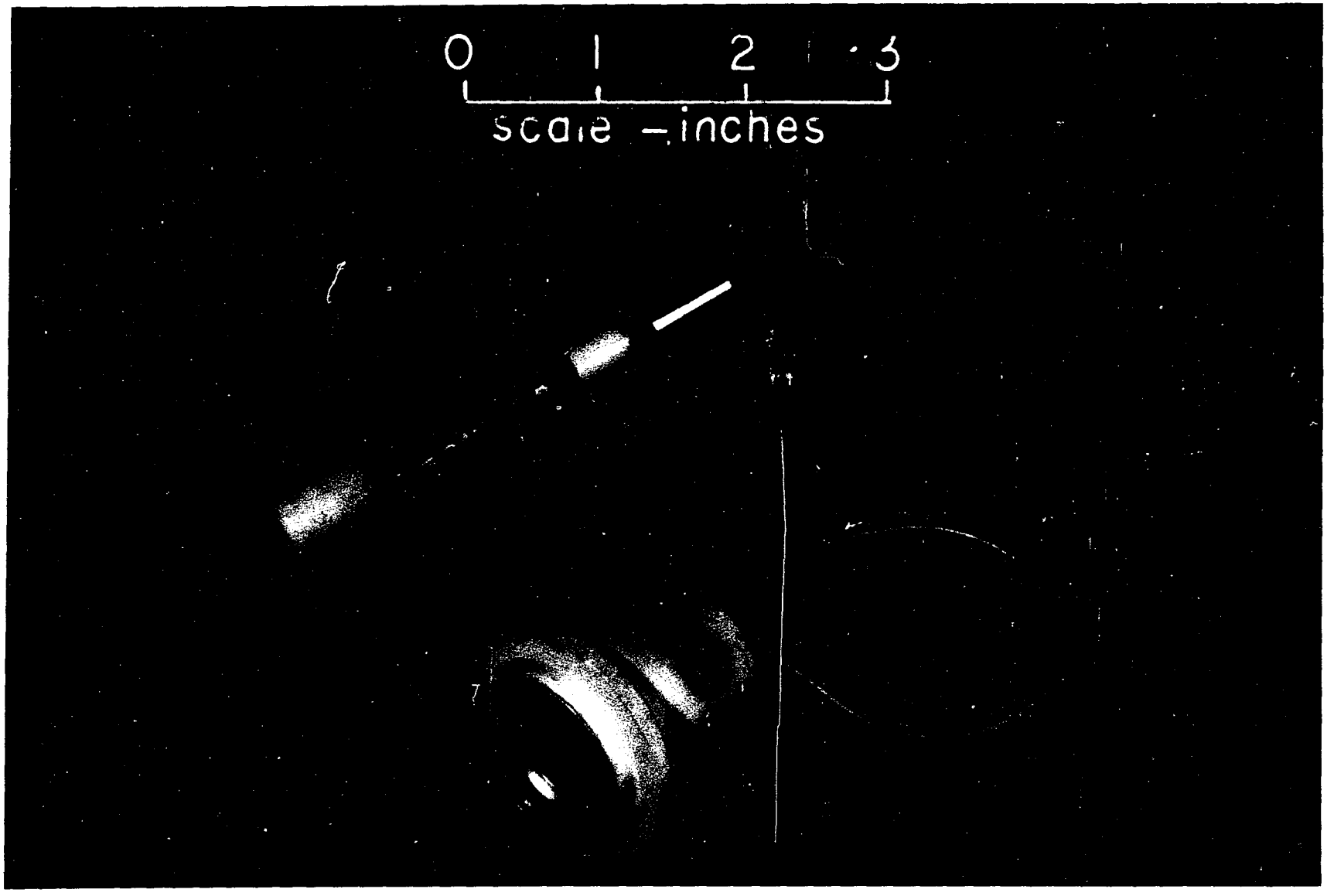

FIGURE 9

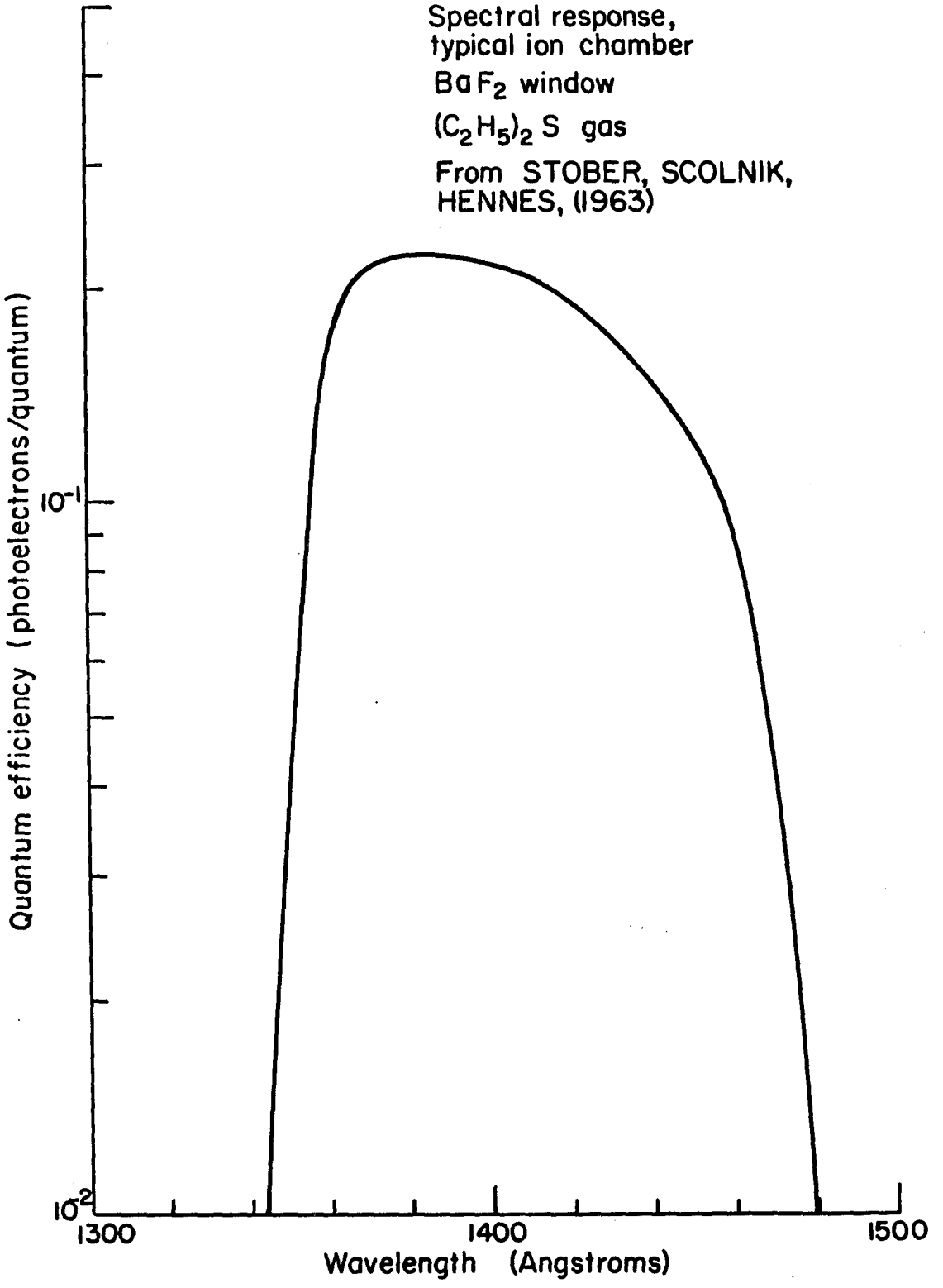
Spectral response,
typical ion chamber
BaF2 window
(C2H5)2 S gas
From STOBER, SCOLNIK,
HENNES, (1963)
Quantum efficiency (photoelectrons/quantum)
10-1
10-2
1300
1400
1500
Wavelength (Angstroms)

FIGURE 10

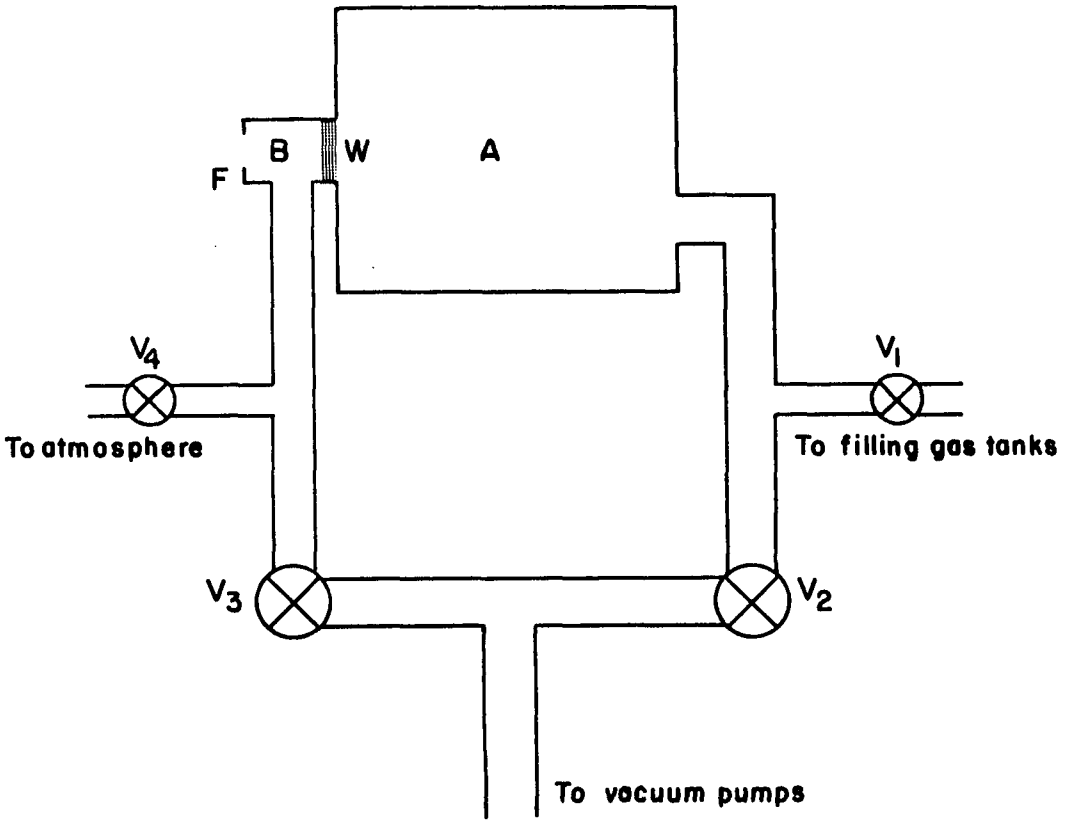
B
W
A
F
V4
V1
To atmosphere
To filling gas tanks
V3
V2
To vacuum pumps

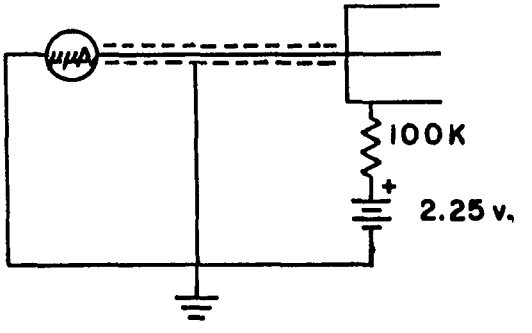
μμA
100K
+
2.25 v.

FIGURE 11

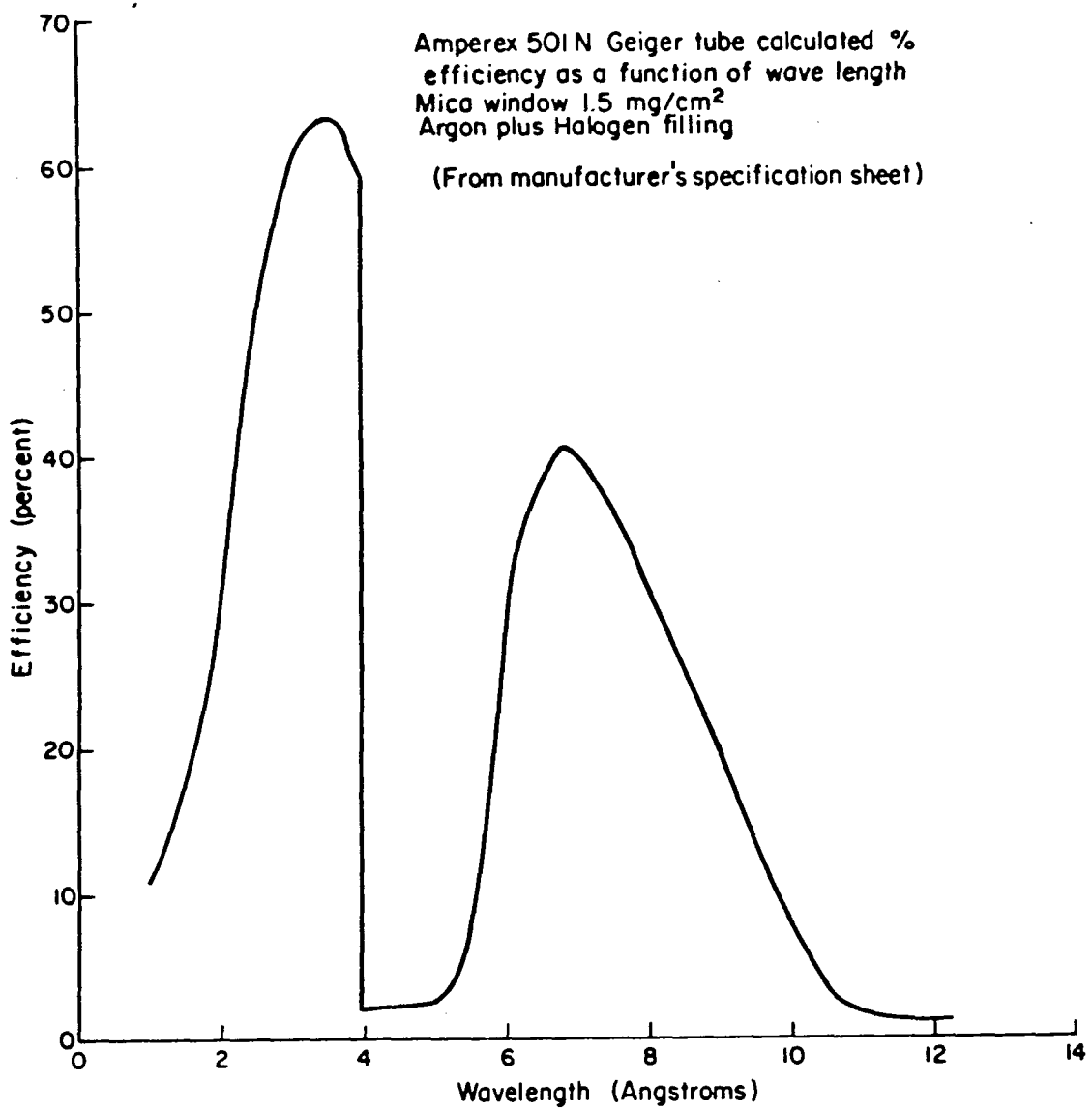
Amperex 501 N Geiger tube calculated % efficiency as a function of wave length
Mica window 1.5 mg/cm²
Argon plus Halogen filling
(From manufacturer's specification sheet)
Efficiency (percent)
70
60
50
40
30
20
10
0
0
2
4
6
8
10
12
14
Wavelength (Angstroms)

FIGURE 12

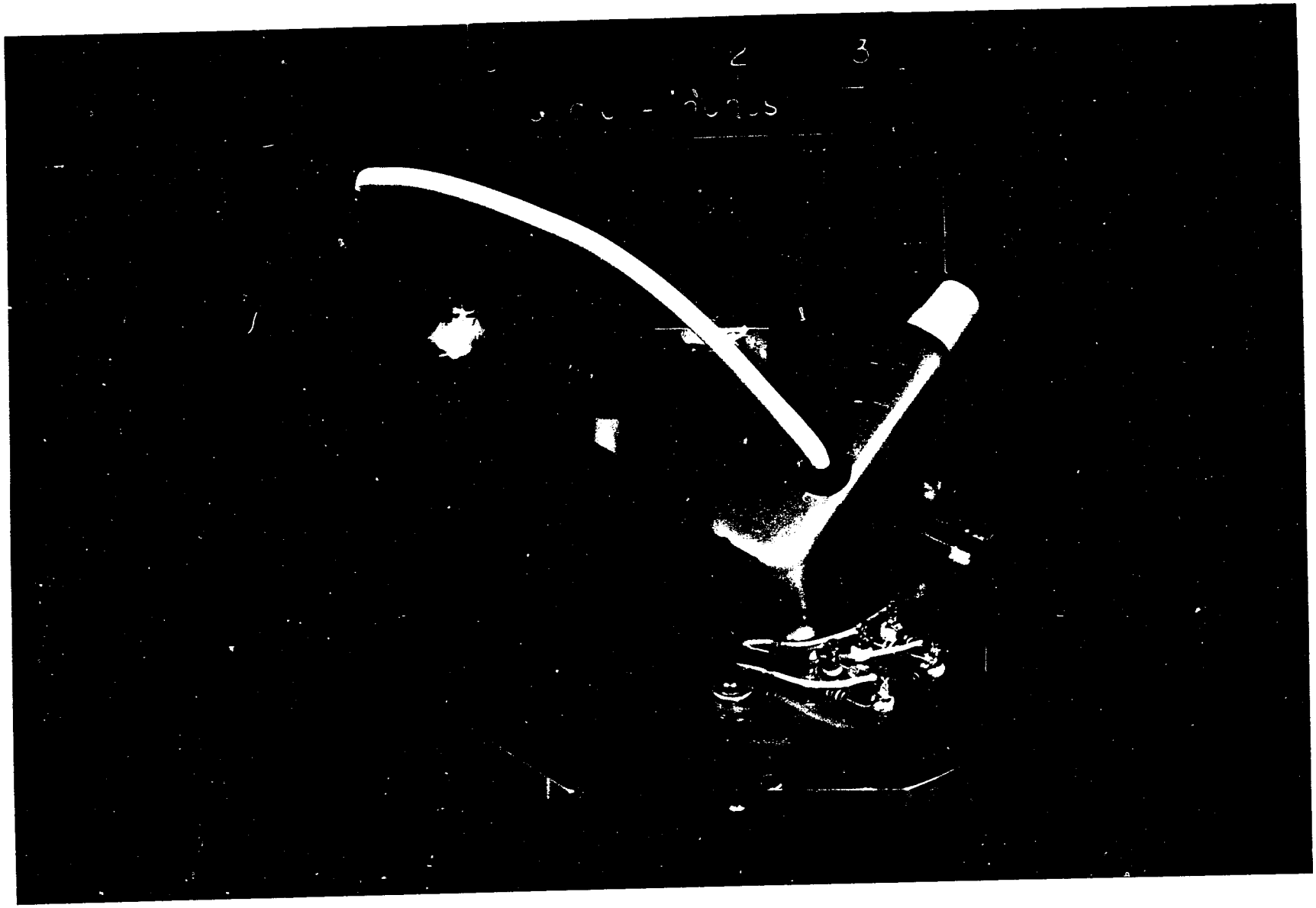

FIGURE 13

GEIGER ELECTRONICS

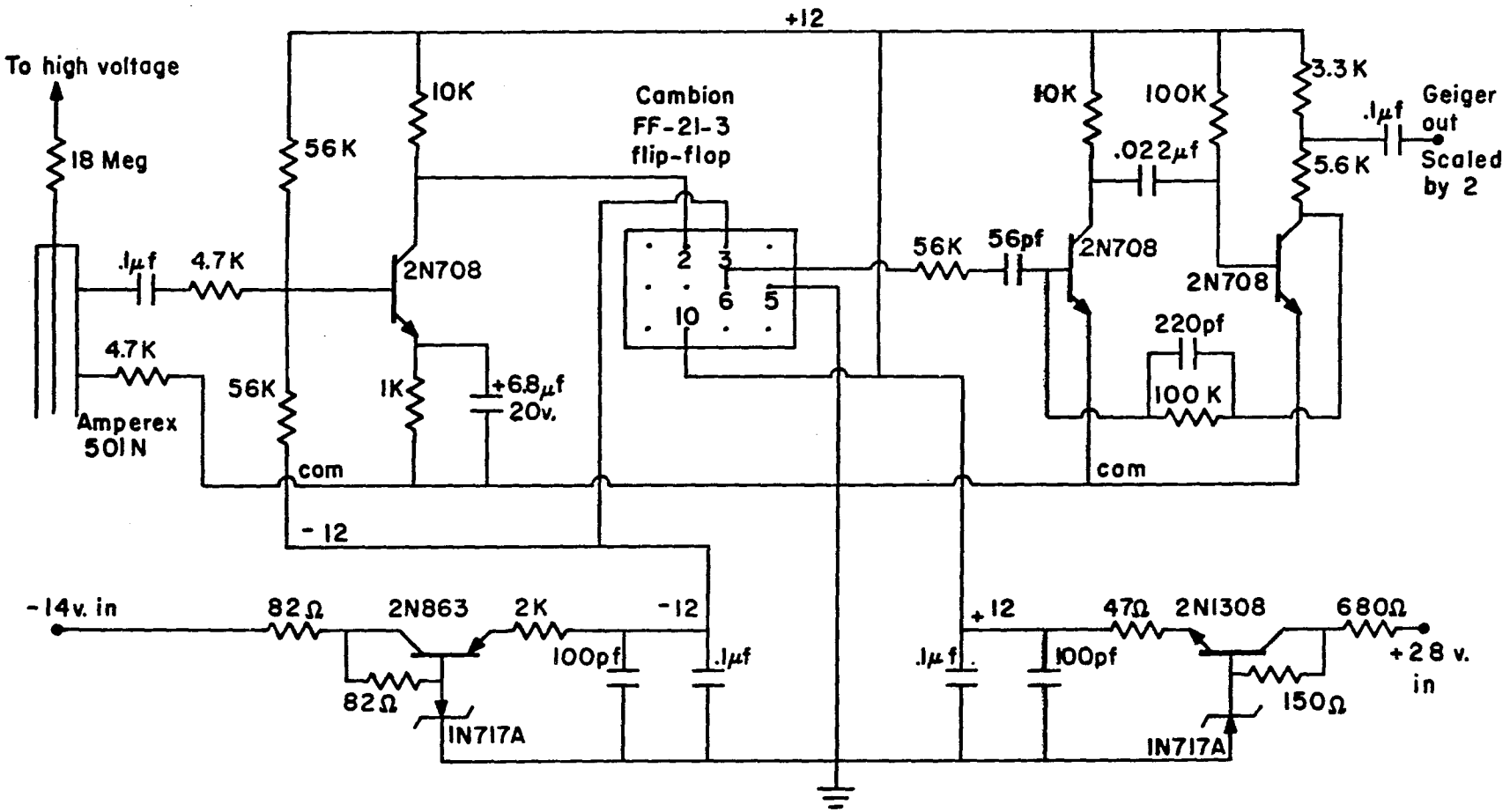

FIGURE 14

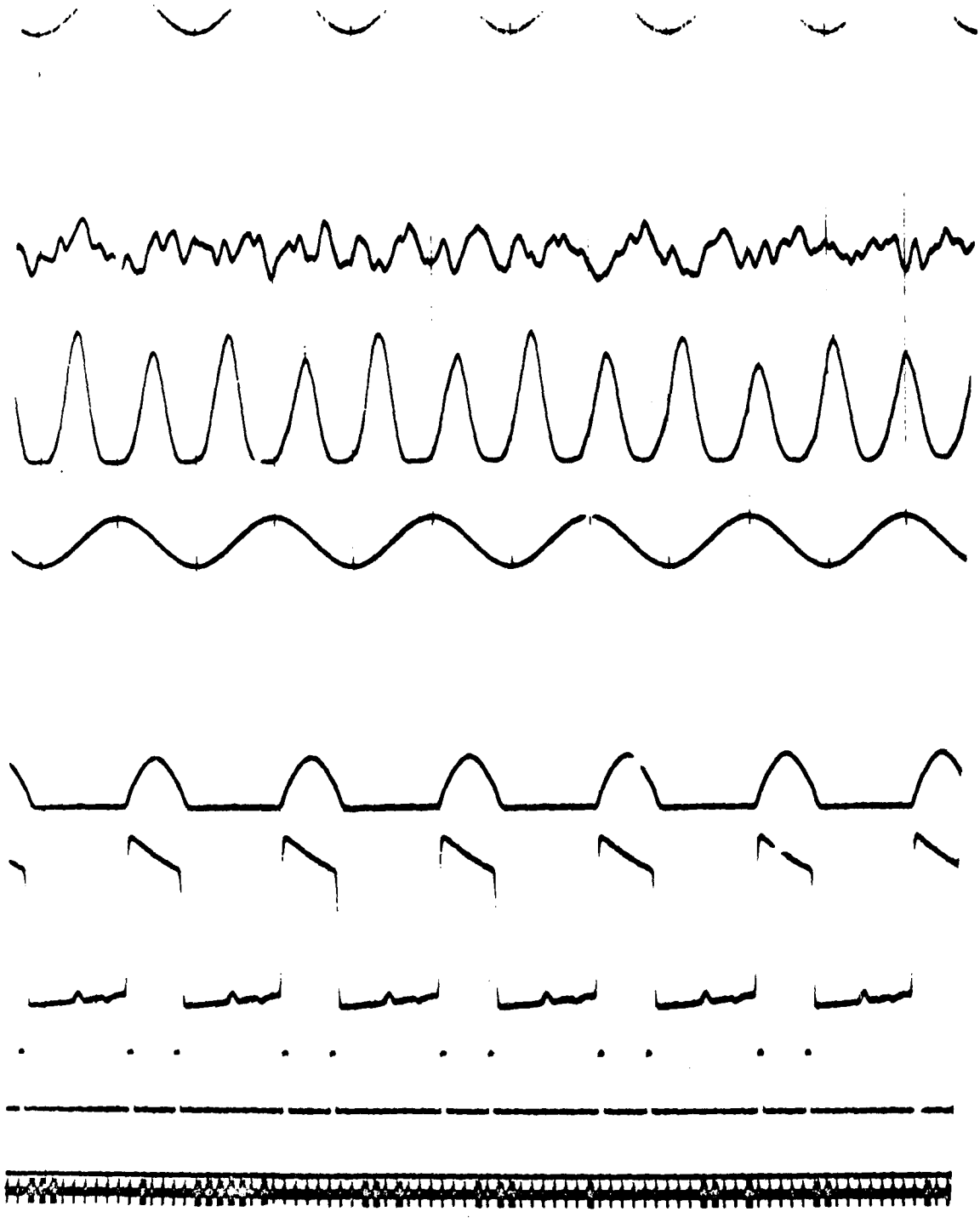

FIGURE 15

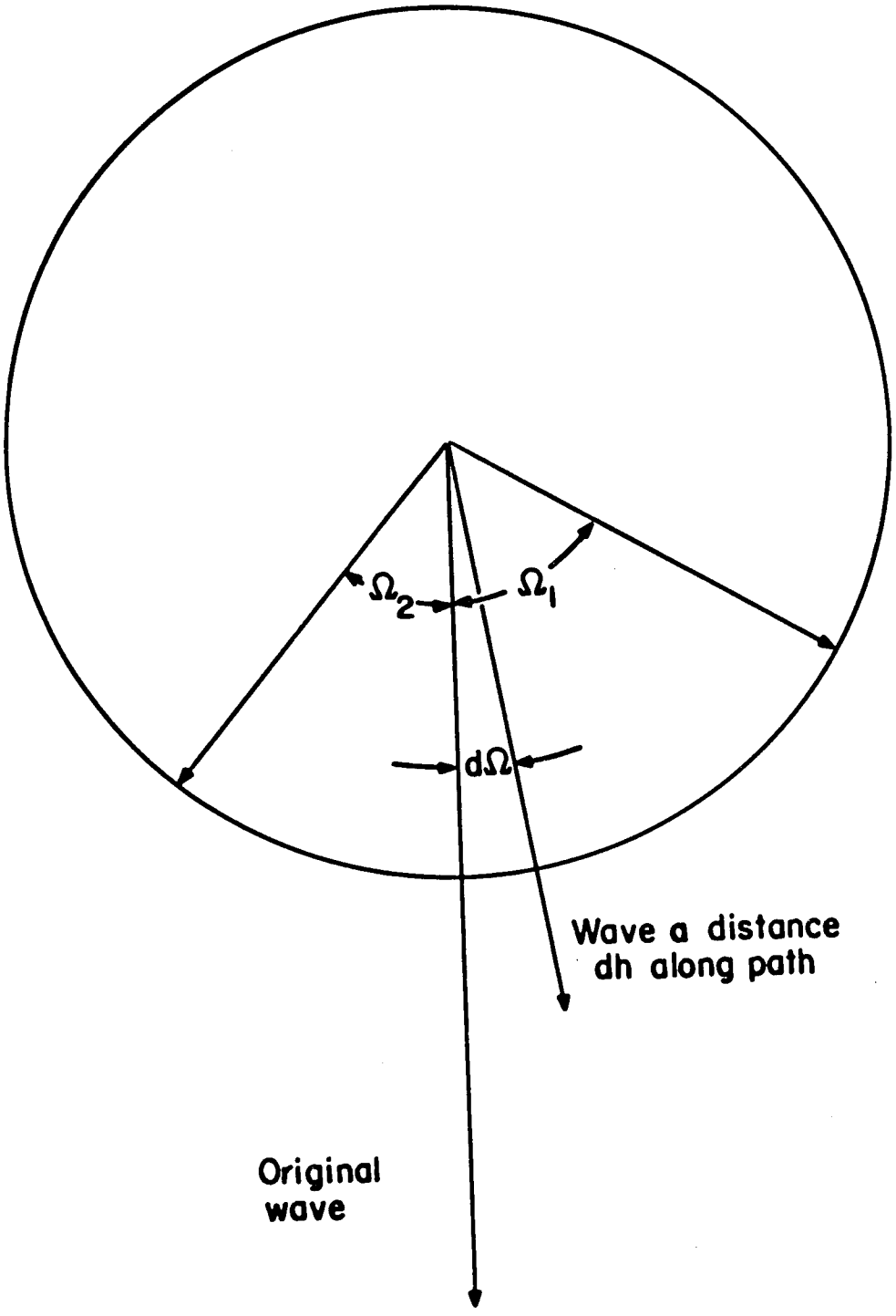
Ω_2
Ω_1
$d\Omega$
Wave a distance dh along path
Original wave
Wave propagates perpendicular to the paper

FIGURE 16

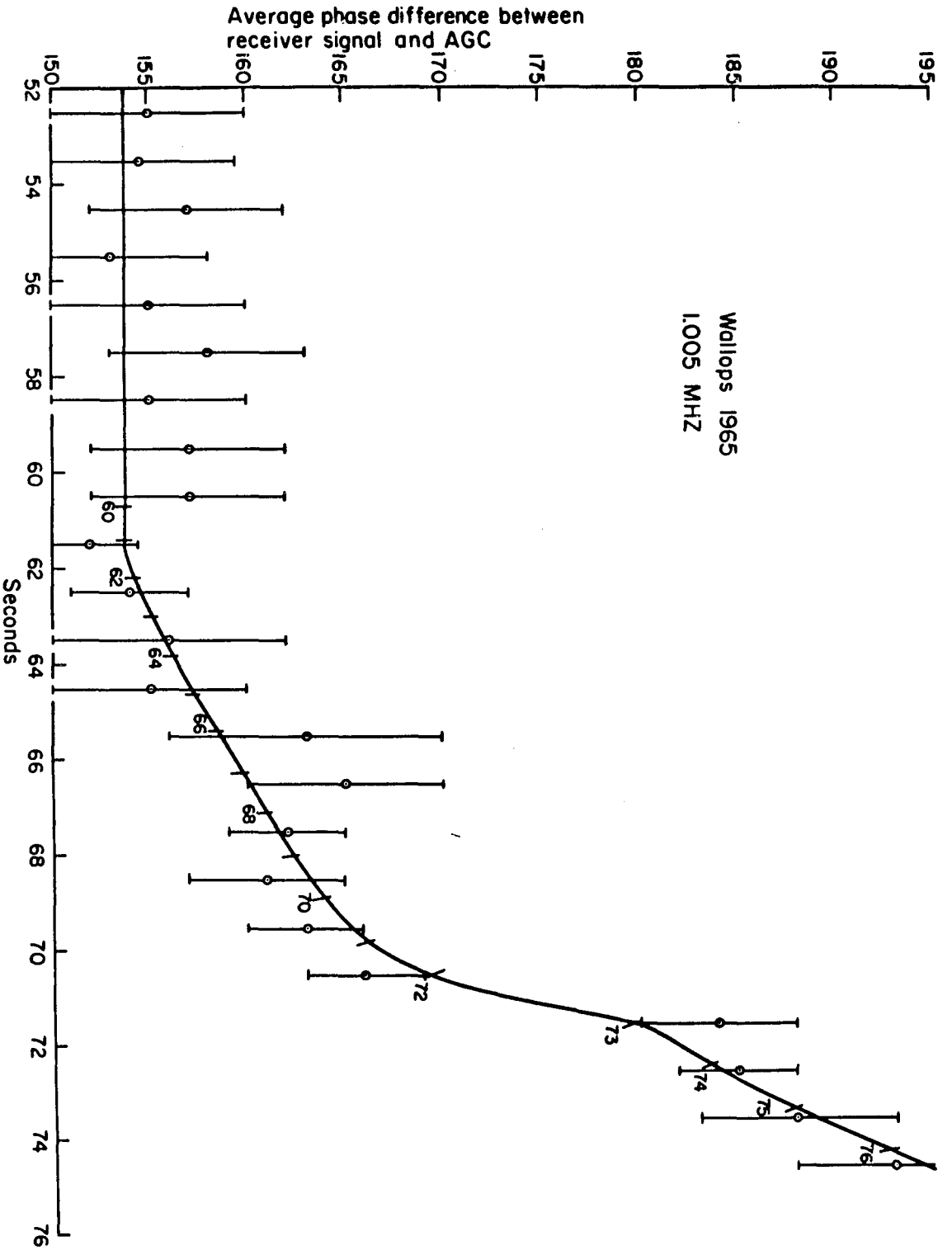
Average phase difference between receiver signal and AGC
150
155
160
165
170
175
180
185
190
195
Wallops 1965
1.005 MHZ
Seconds
52
54
56
58
60
62
64
66
68
70
72
74
76

FIGURE 17

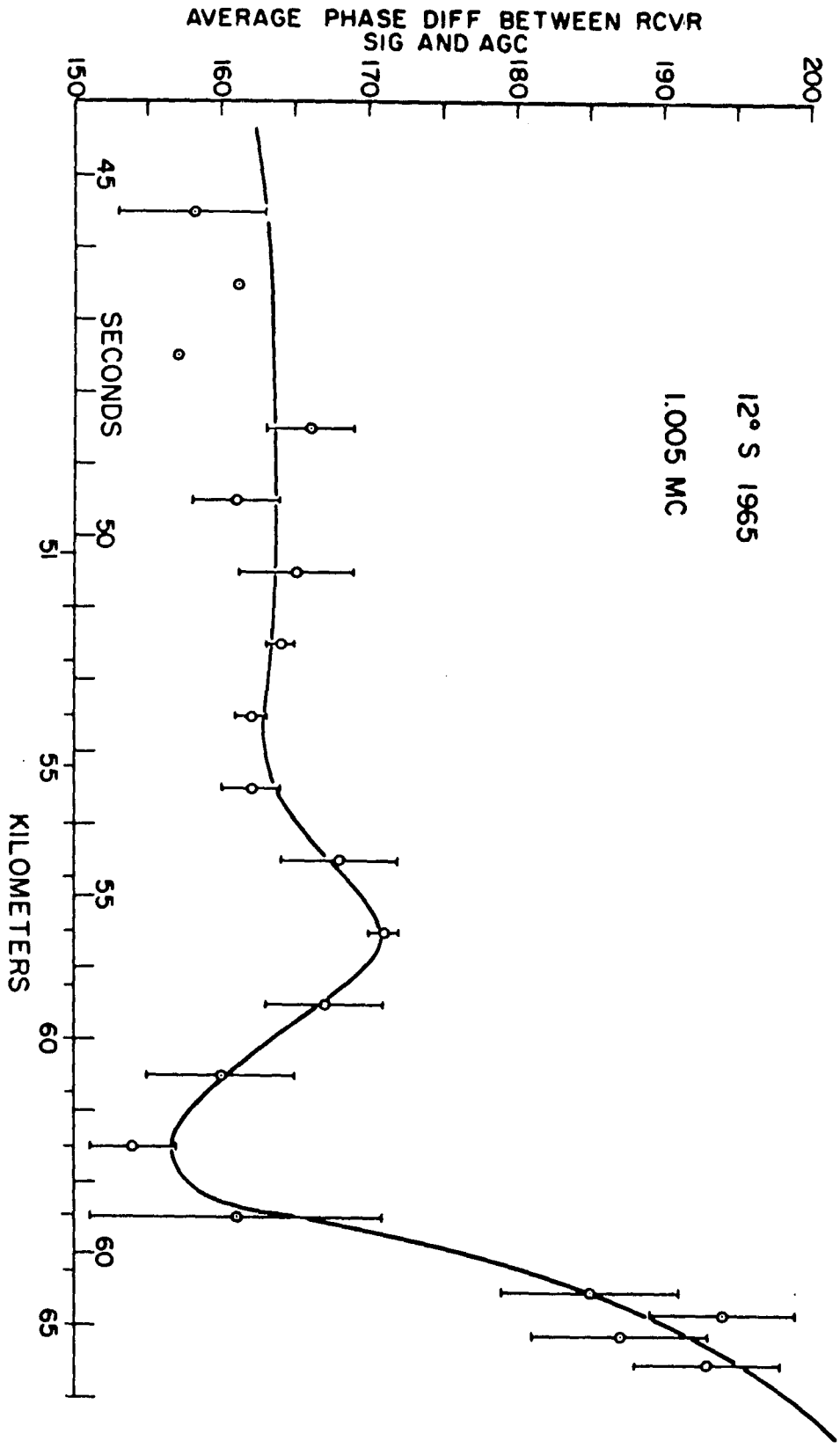
AVERAGE PHASE DIFF BETWEEN RCVR SIG AND AGC
150
160
170
180
190
200
45
SECONDS
50
51
55
55
60
60
65
KILOMETERS
1.005 MC
12° S 1965

FIGURE 18

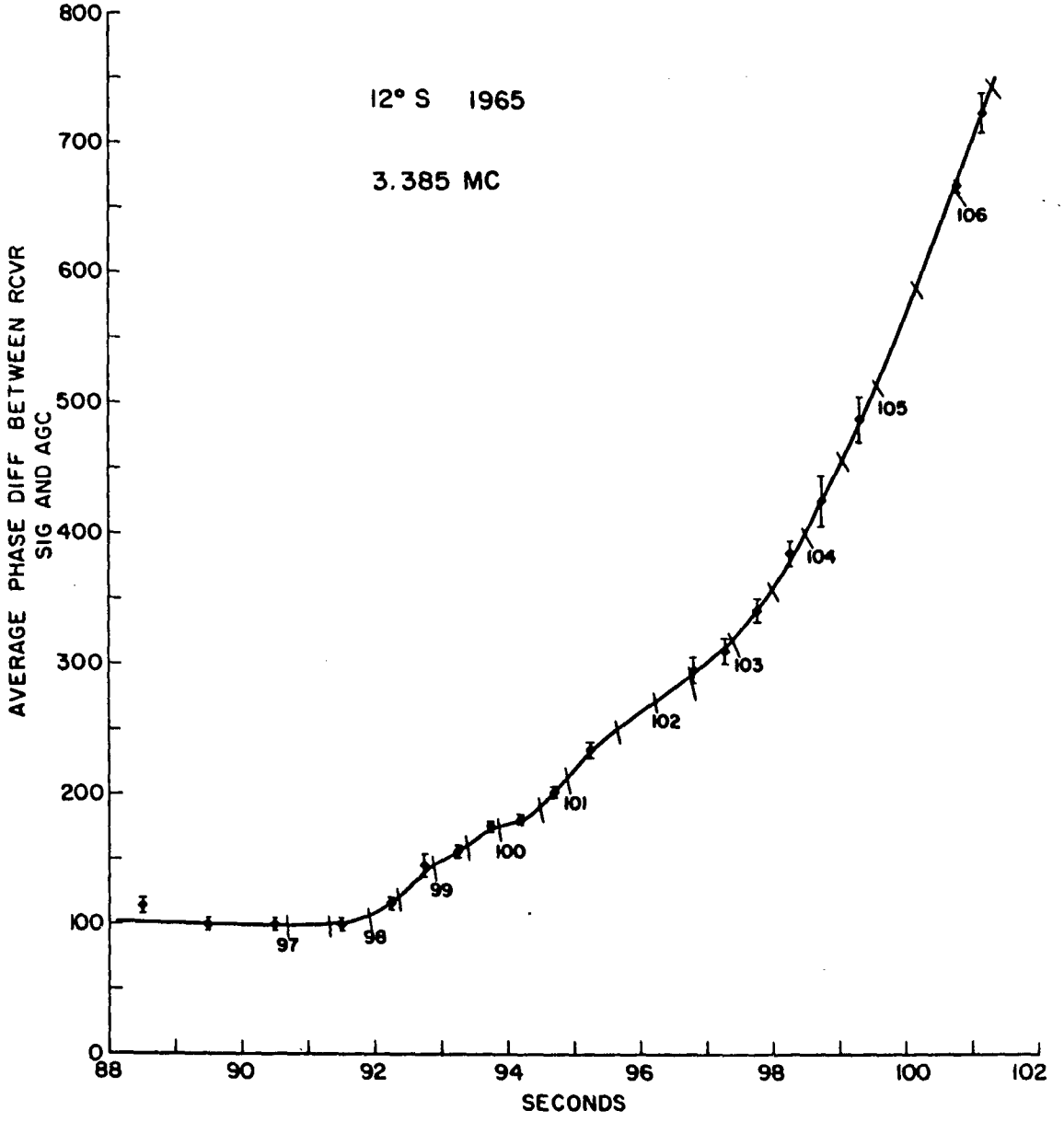
12° S 1965
3.385 MC
AVERAGE PHASE DIFF BETWEEN RCVR SIG AND AGC
SECONDS
800
700
600
500
400
300
200
100
0
88
90
92
94
96
98
100
102
97
98
99
100
101
102
103
104
105
106

FIGURE 19

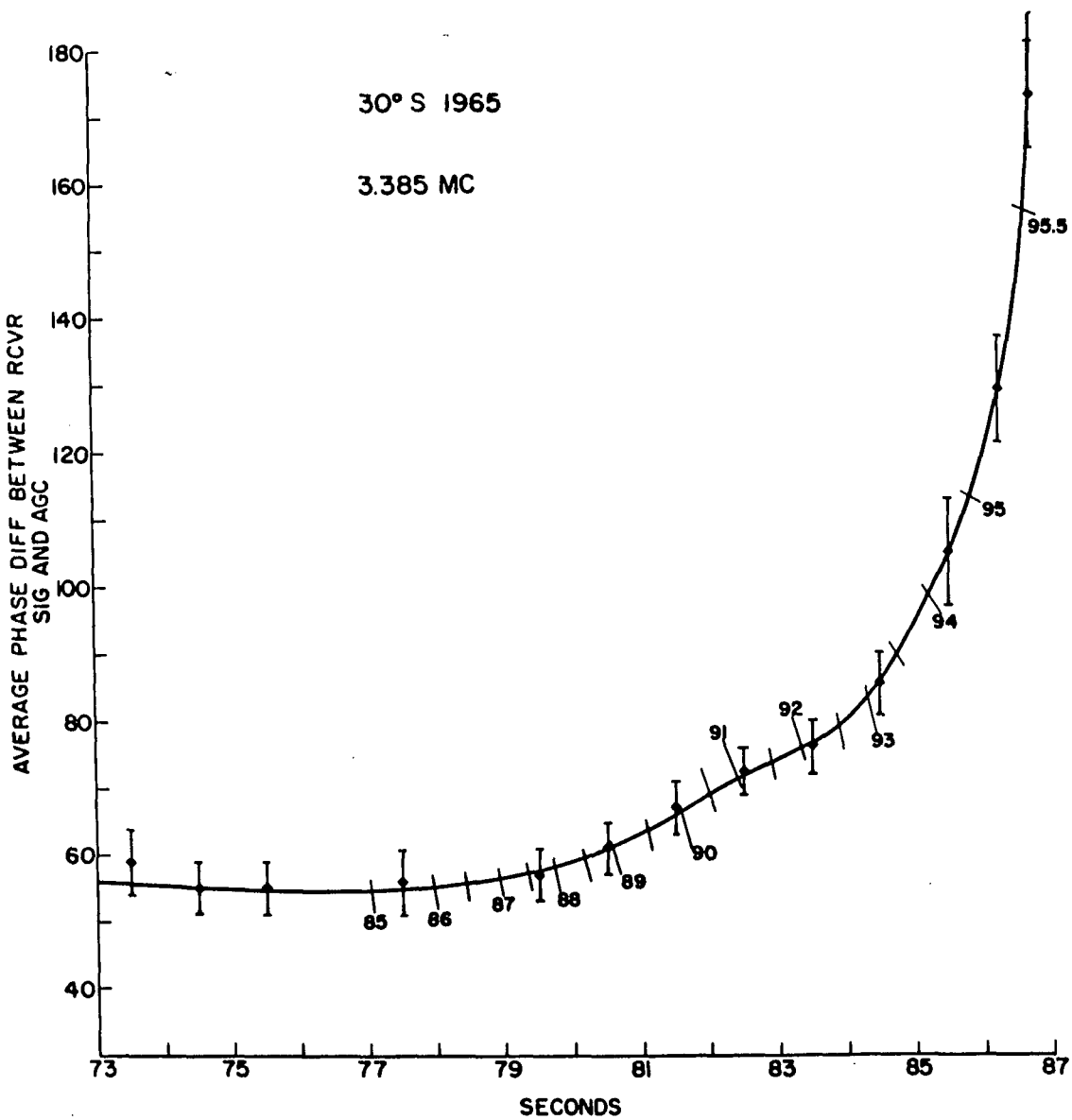
30° S 1965
3.385 MC
AVERAGE PHASE DIFF BETWEEN RCVR SIG AND AGC
SECONDS
180
160
140
120
100
80
60
40
73
75
77
79
81
83
85
87
85
86
87
88
89
90
91
92
93
94
95
95.5

FIGURE 20

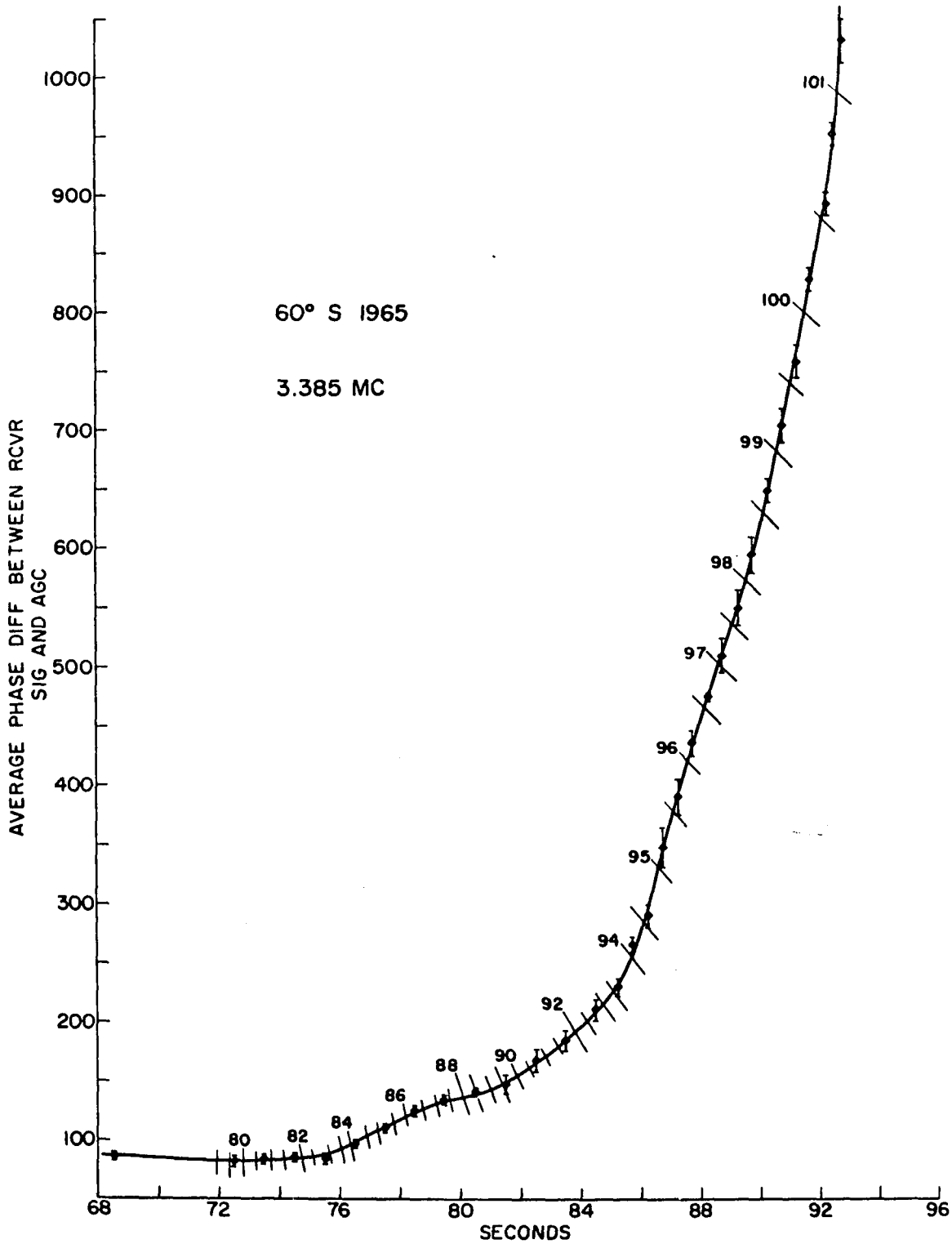
60° S 1965
3.385 MC
AVERAGE PHASE DIFF BETWEEN RCVR SIG AND AGC
SECONDS
1000
900
800
700
600
500
400
300
200
100
68
72
76
80
84
88
92
96
80
82
84
86
88
90
92
94
95
96
97
98
99
100
101

FIGURE 21

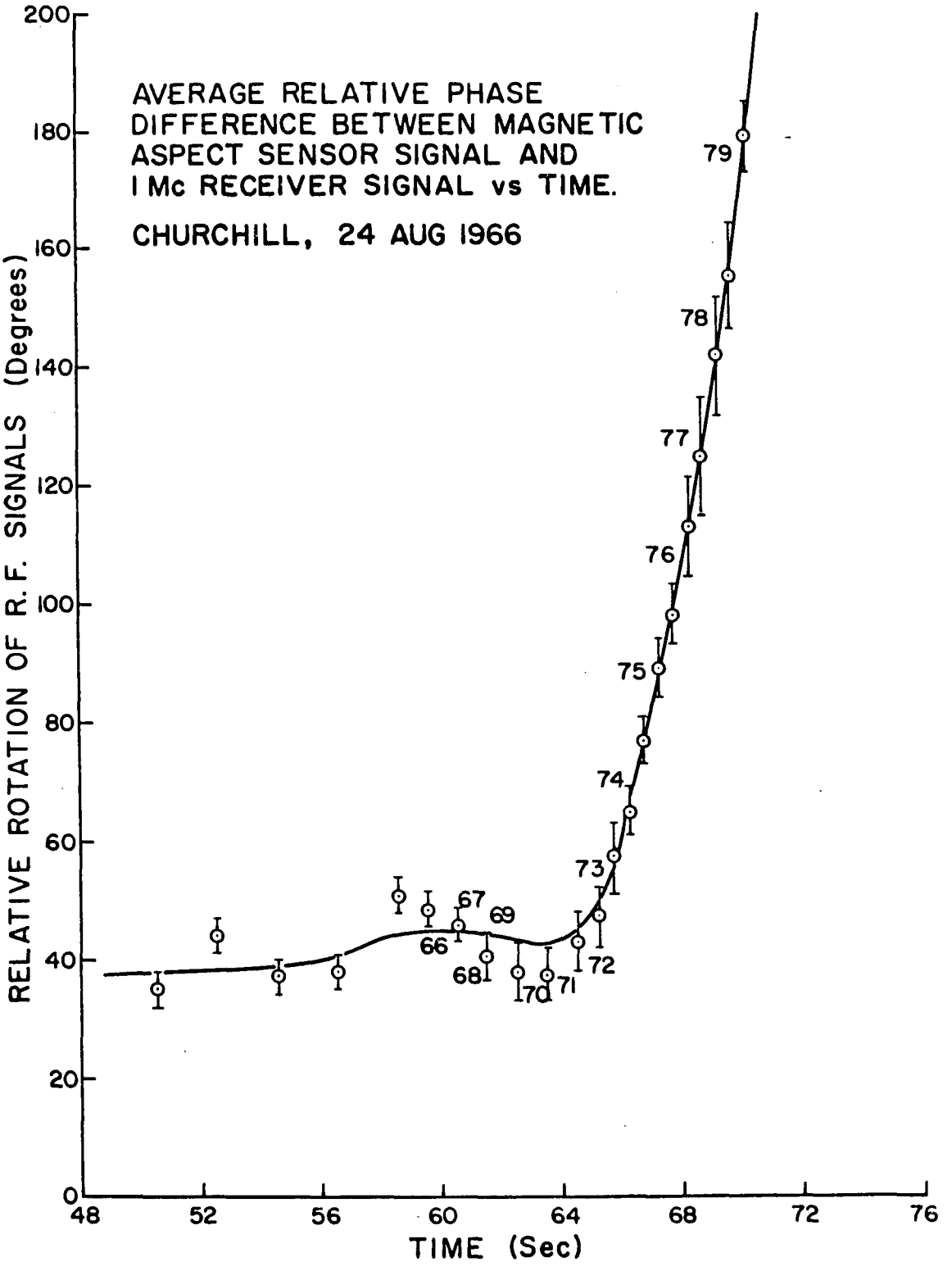
AVERAGE RELATIVE PHASE
DIFFERENCE BETWEEN MAGNETIC
ASPECT SENSOR SIGNAL AND
I Mc RECEIVER SIGNAL vs TIME.
CHURCHILL, 24 AUG 1966
RELATIVE ROTATION OF R.F. SIGNALS (Degrees)
TIME (Sec)
0
20
40
60
80
100
120
140
160
180
200
48
52
56
60
64
68
72
76
66
67
68
69
70
71
72
73
74
75
76
77
78
79

FIGURE 22

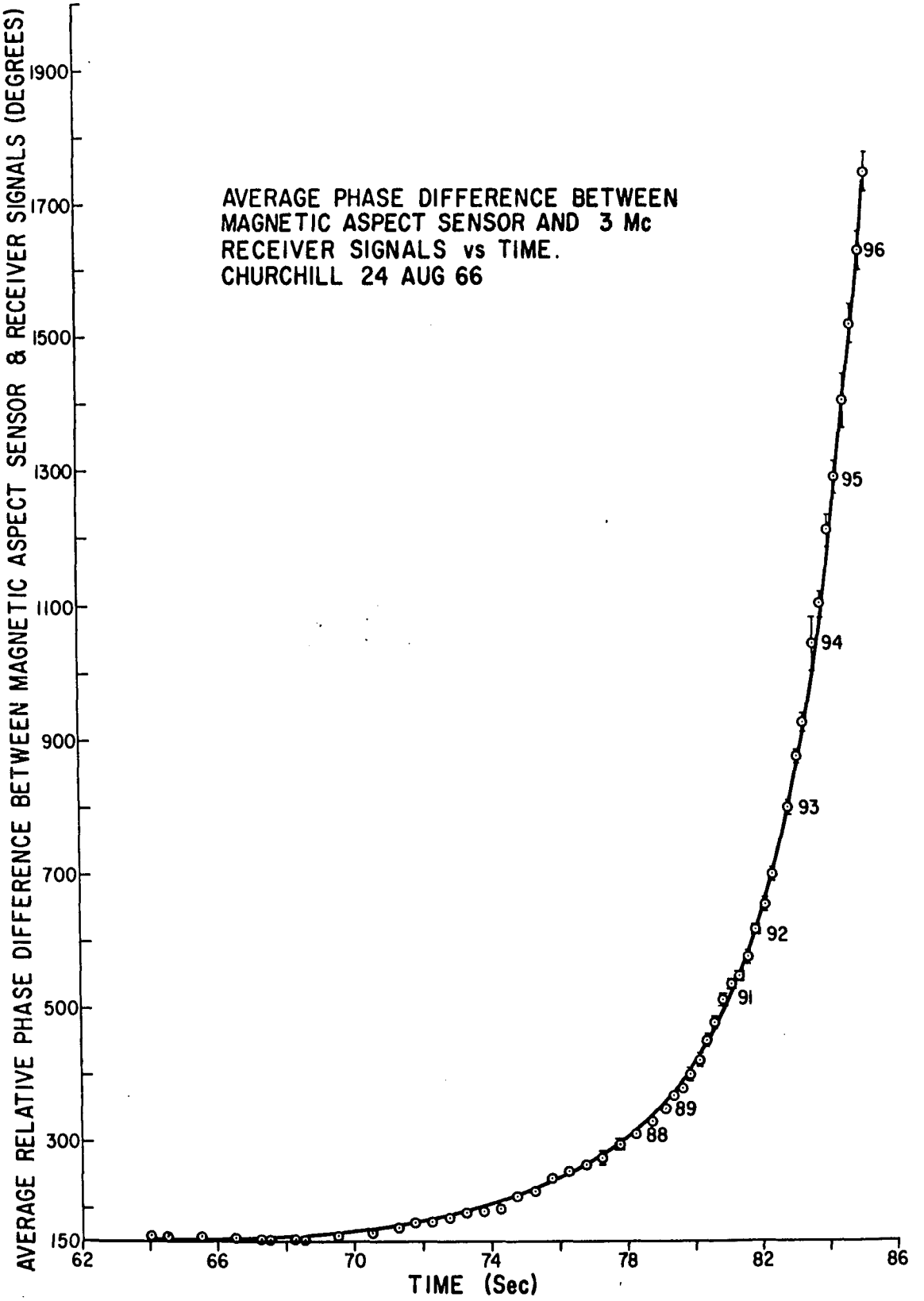
AVERAGE PHASE DIFFERENCE BETWEEN MAGNETIC ASPECT SENSOR AND 3 Mc RECEIVER SIGNALS vs TIME.
CHURCHILL 24 AUG 66
AVERAGE RELATIVE PHASE DIFFERENCE BETWEEN MAGNETIC ASPECT SENSOR & RECEIVER SIGNALS (DEGREES)
1900
1700
1500
1300
1100
900
700
500
300
150
62
66
70
74
78
82
86
TIME (Sec)
88
89
91
92
93
94
95
96

FIGURE 23

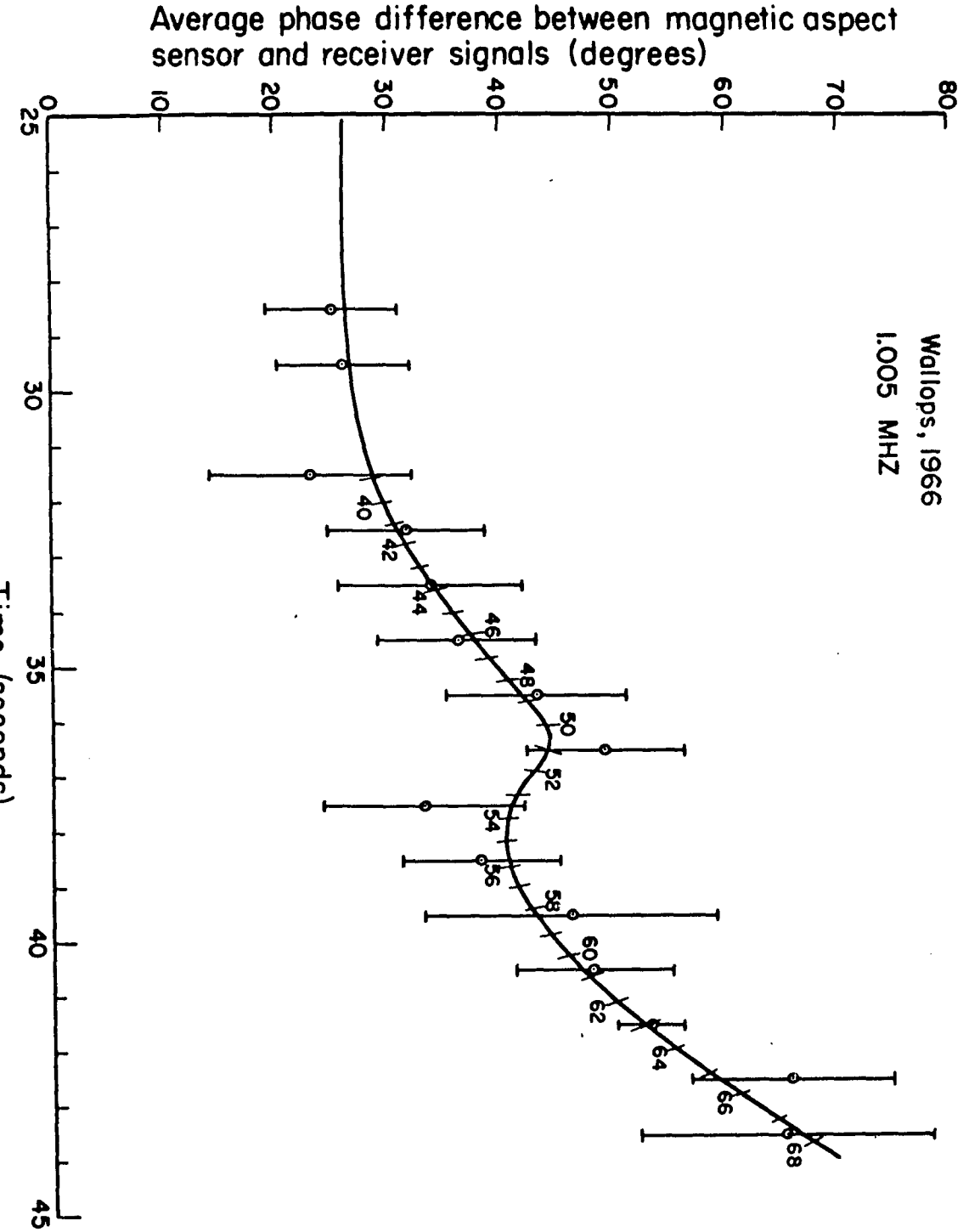
Average phase difference between magnetic aspect sensor and receiver signals (degrees)
0
10
20
30
40
50
60
70
80
25
30
35
40
45
Time (seconds)
40
42
44
46
48
50
52
54
56
58
60
62
64
66
68
Wallops, 1966
1.005 MHZ

FIGURE 24

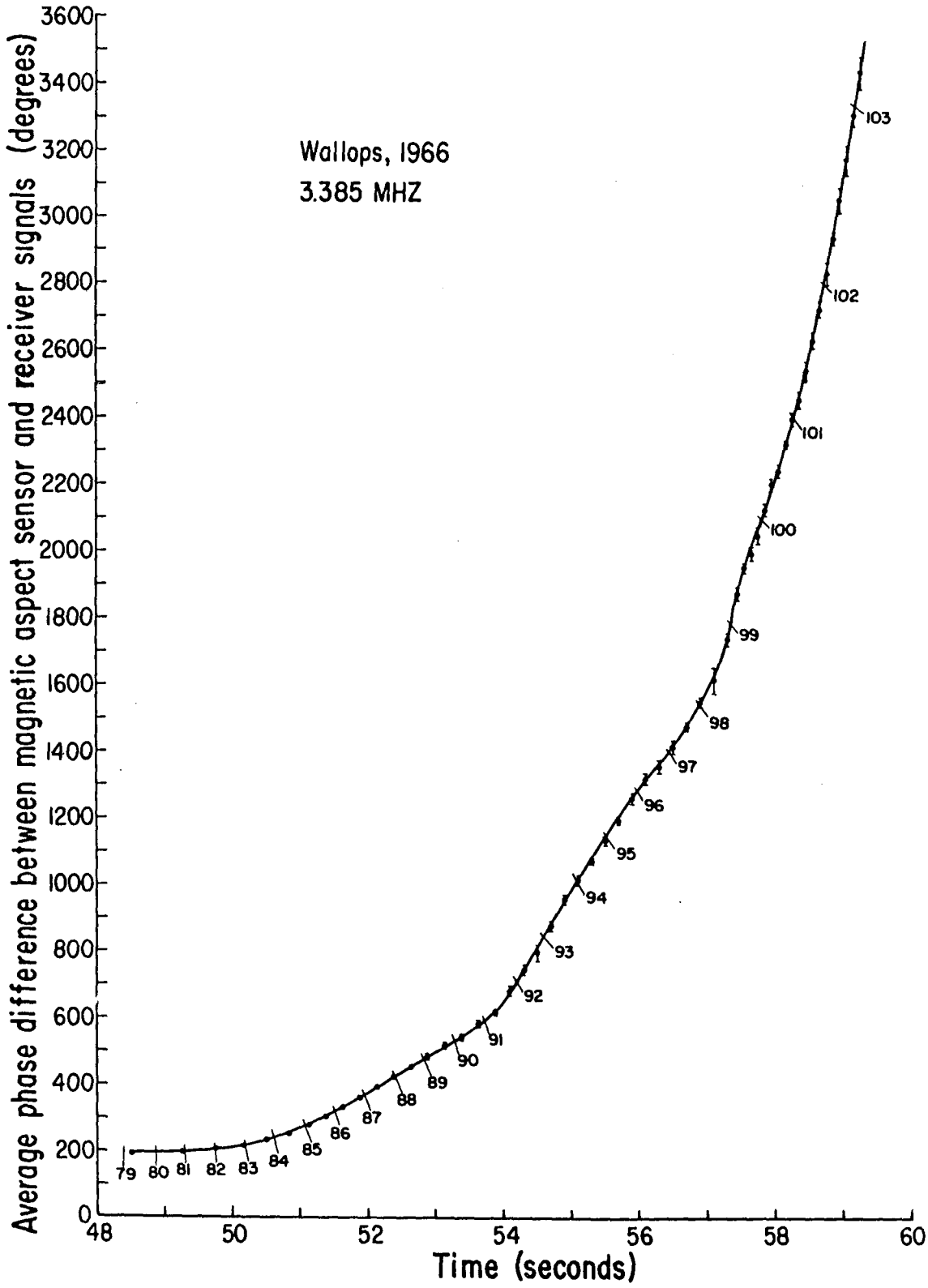
Wallops, 1966
3.385 MHZ
Average phase difference between magnetic aspect sensor and receiver signals (degrees)
Time (seconds)
0
200
400
600
800
1000
1200
1400
1600
1800
2000
2200
2400
2600
2800
3000
3200
3400
3600
48
50
52
54
56
58
60
79
80
81
82
83
84
85
86
87
88
89
90
91
92
93
94
95
96
97
98
99
100
101
102
103

FIGURE 25

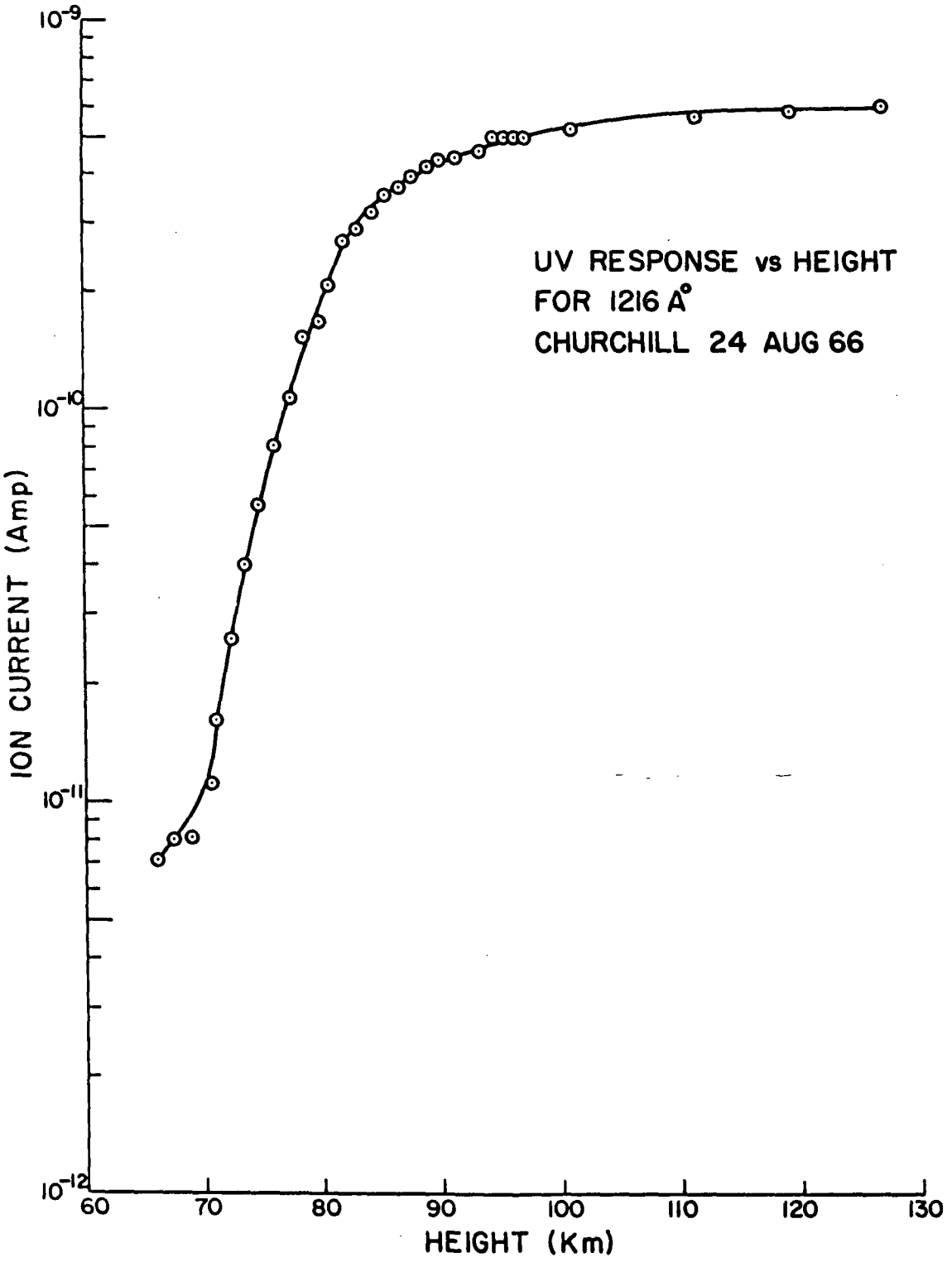
UV RESPONSE vs HEIGHT
FOR 1216 A°
CHURCHILL 24 AUG 66
ION CURRENT (Amp)
10⁻⁹
10⁻¹⁰
10⁻¹¹
10⁻¹²
60
70
80
90
100
110
120
130
HEIGHT (Km)

FIGURE 26

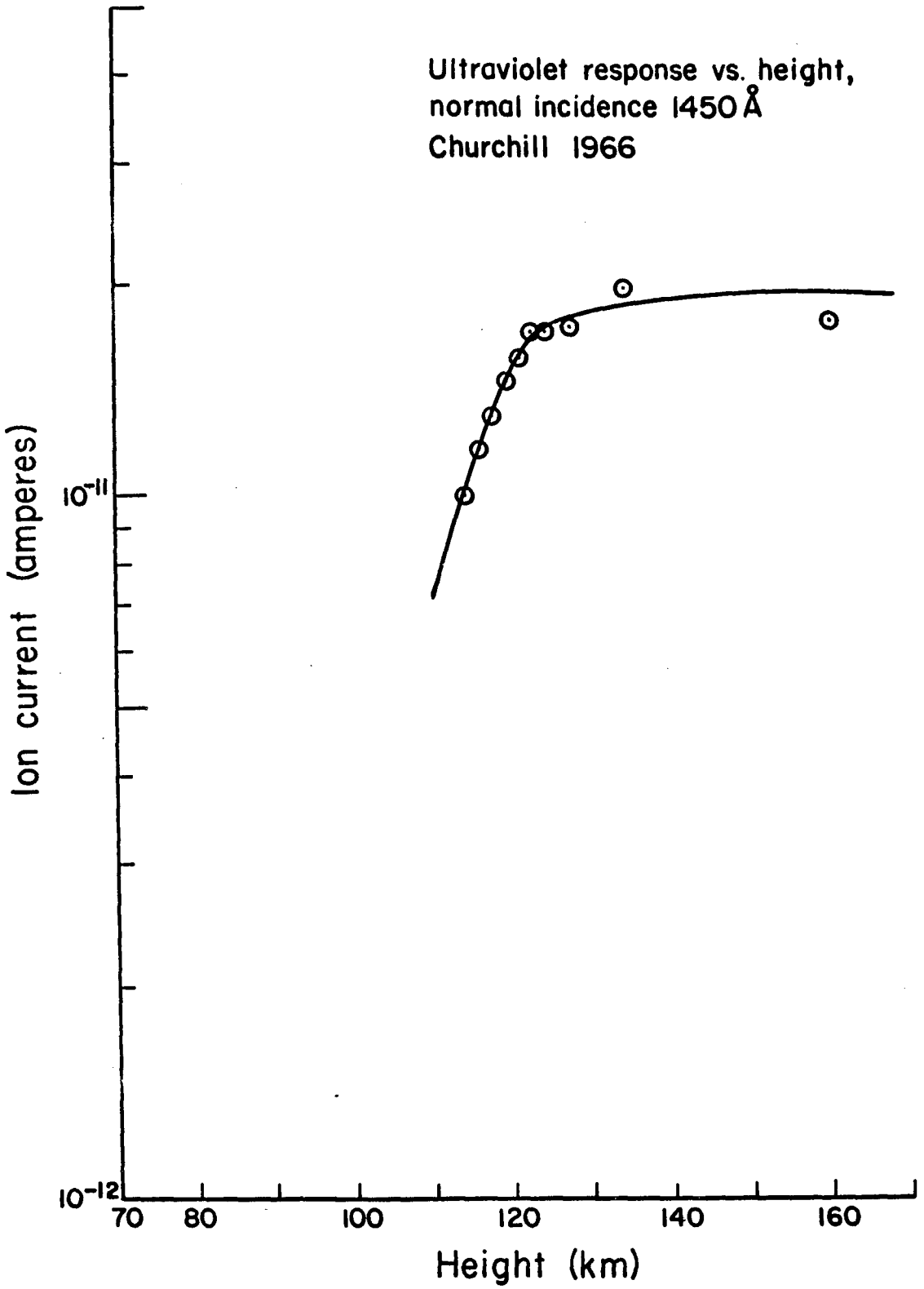
Ultraviolet response vs. height,
normal incidence 1450 Å
Churchill 1966
Ion current (amperes)
10^{-11}
10^{-12}
70
80
100
120
140
160
Height (km)

FIGURE 27

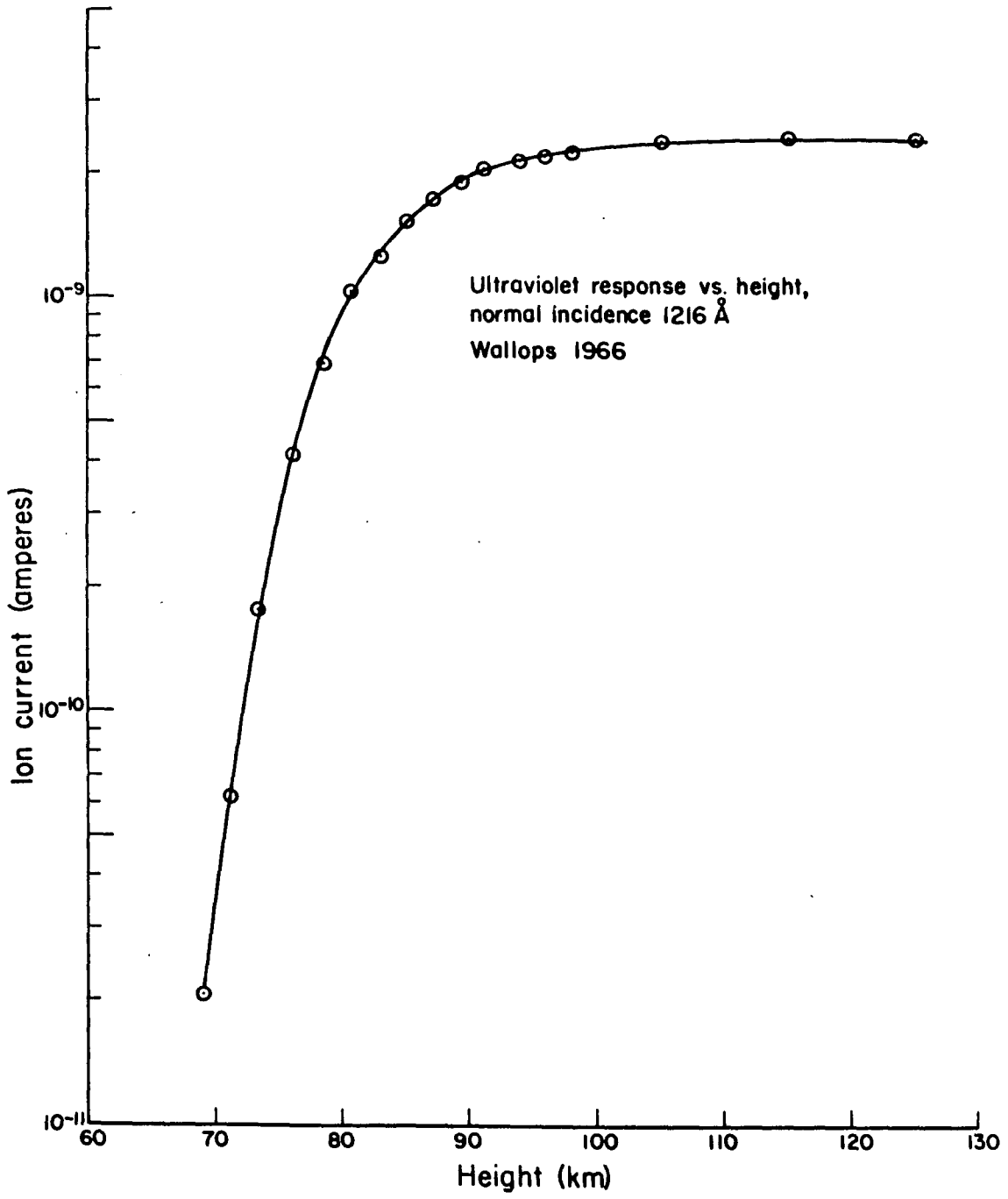
Ultraviolet response vs. height,
normal incidence 1216 Å
Wallops 1966
Ion current (amperes)
10⁻⁹
10⁻¹⁰
10⁻¹¹
60
70
80
90
100
110
120
130
Height (km)

FIGURE 28

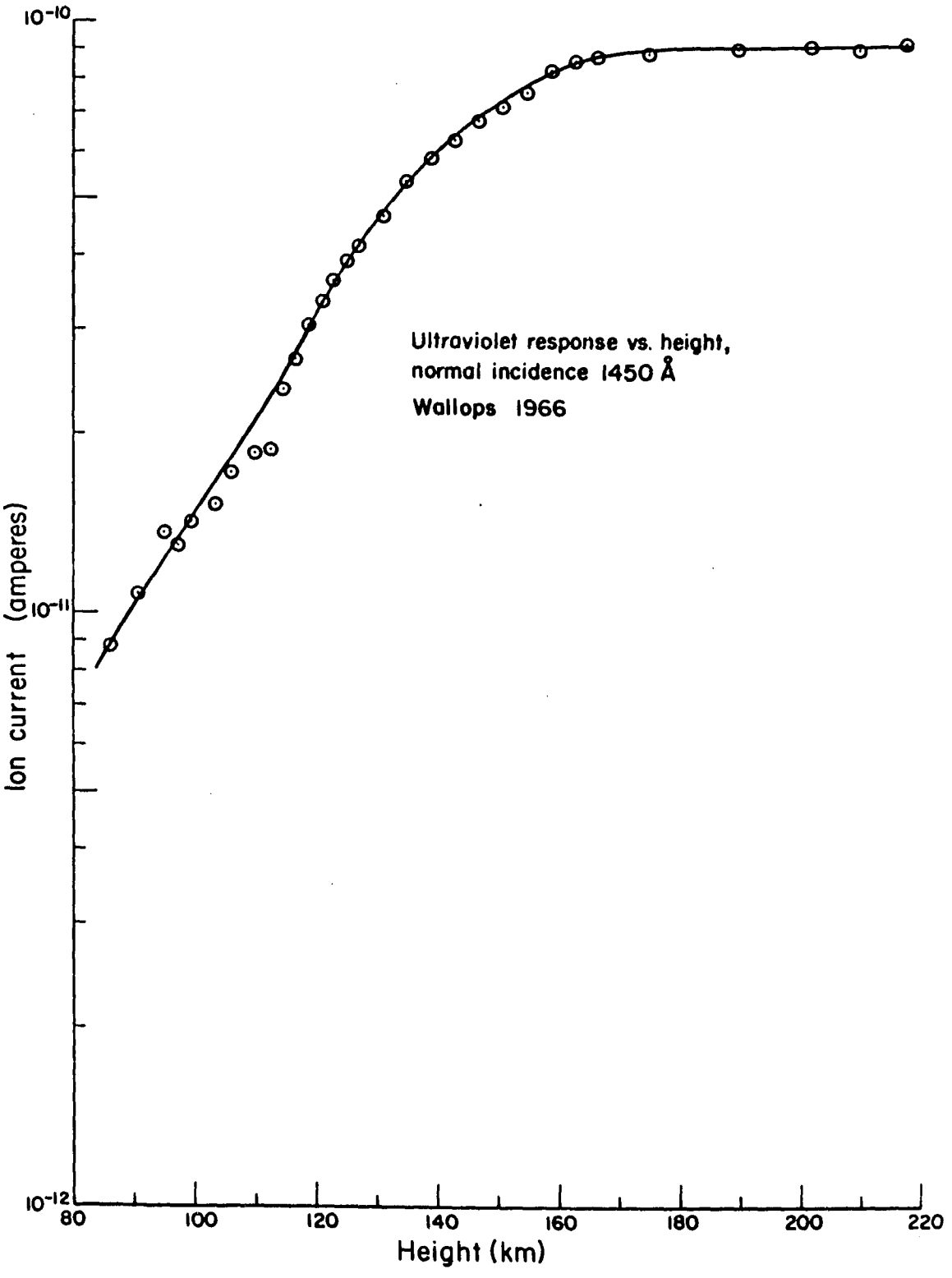
Ultraviolet response vs. height,
normal incidence 1450 Å
Wallops 1966
Ion current (amperes)
10-10
10-11
10-12
80
100
120
140
160
180
200
220
Height (km)

FIGURE 29

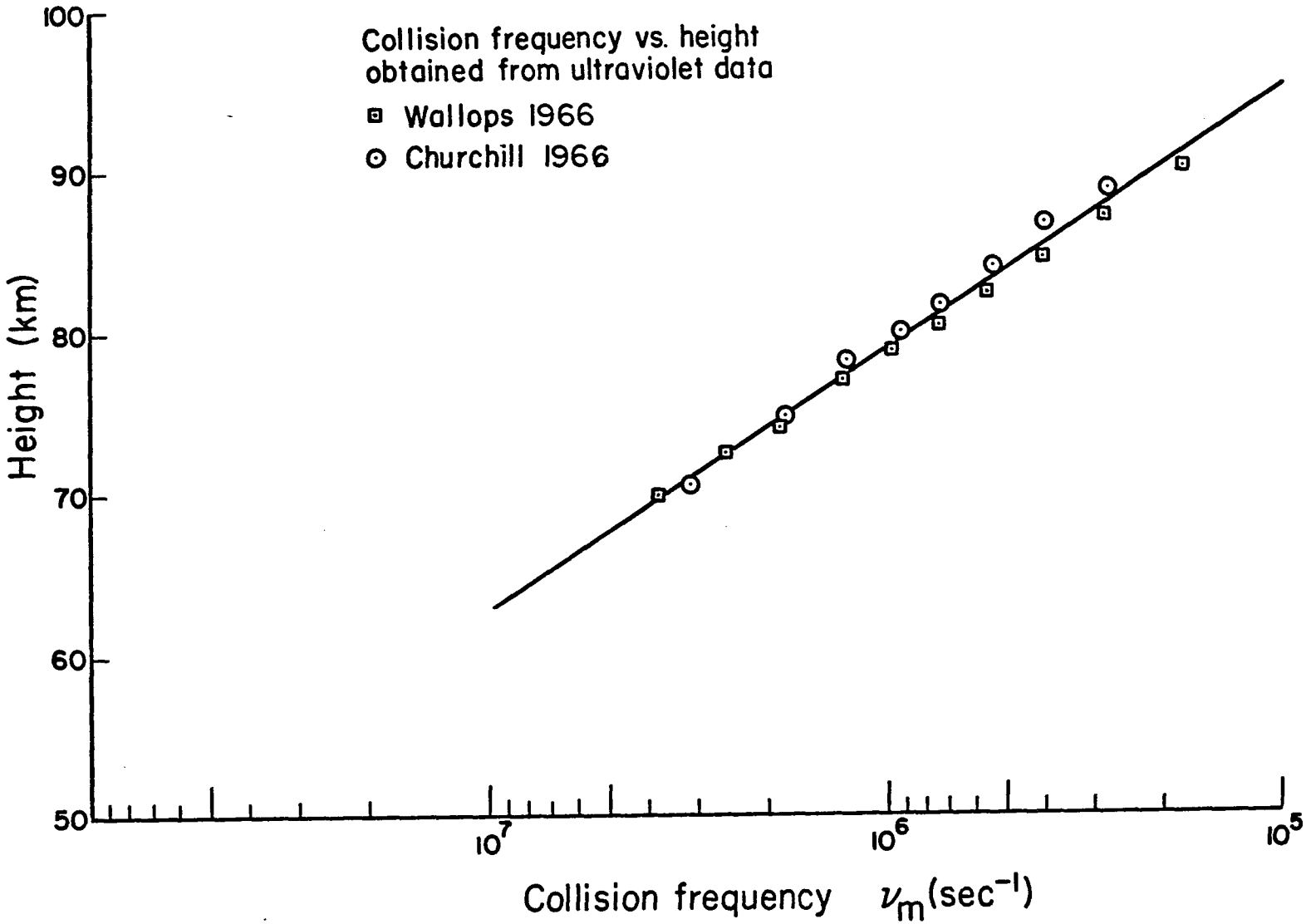
Collision frequency vs. height
obtained from ultraviolet data
Wallops 1966
Churchill 1966
100
90
80
70
60
50
Height (km)
10^7
10^6
10^5
Collision frequency $\nu_m(sec^{-1})$

FIGURE 30

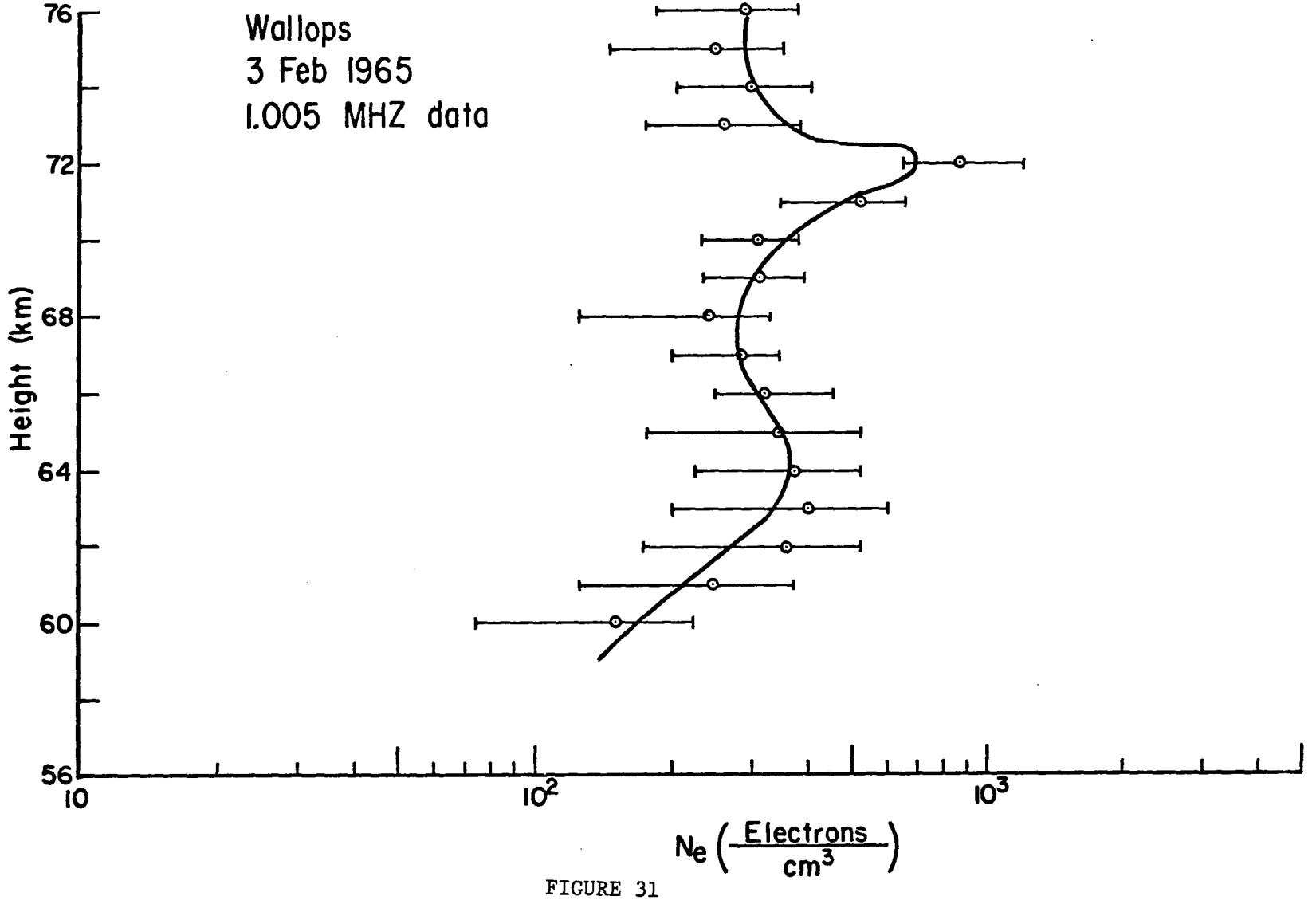
Wallops
3 Feb 1965
1.005 MHZ data
76
72
68
64
60
56
Height (km)
10
10^2
10^3
$N_e \left(\frac{\text{Electrons}}{cm^3} \right)$

FIGURE 31

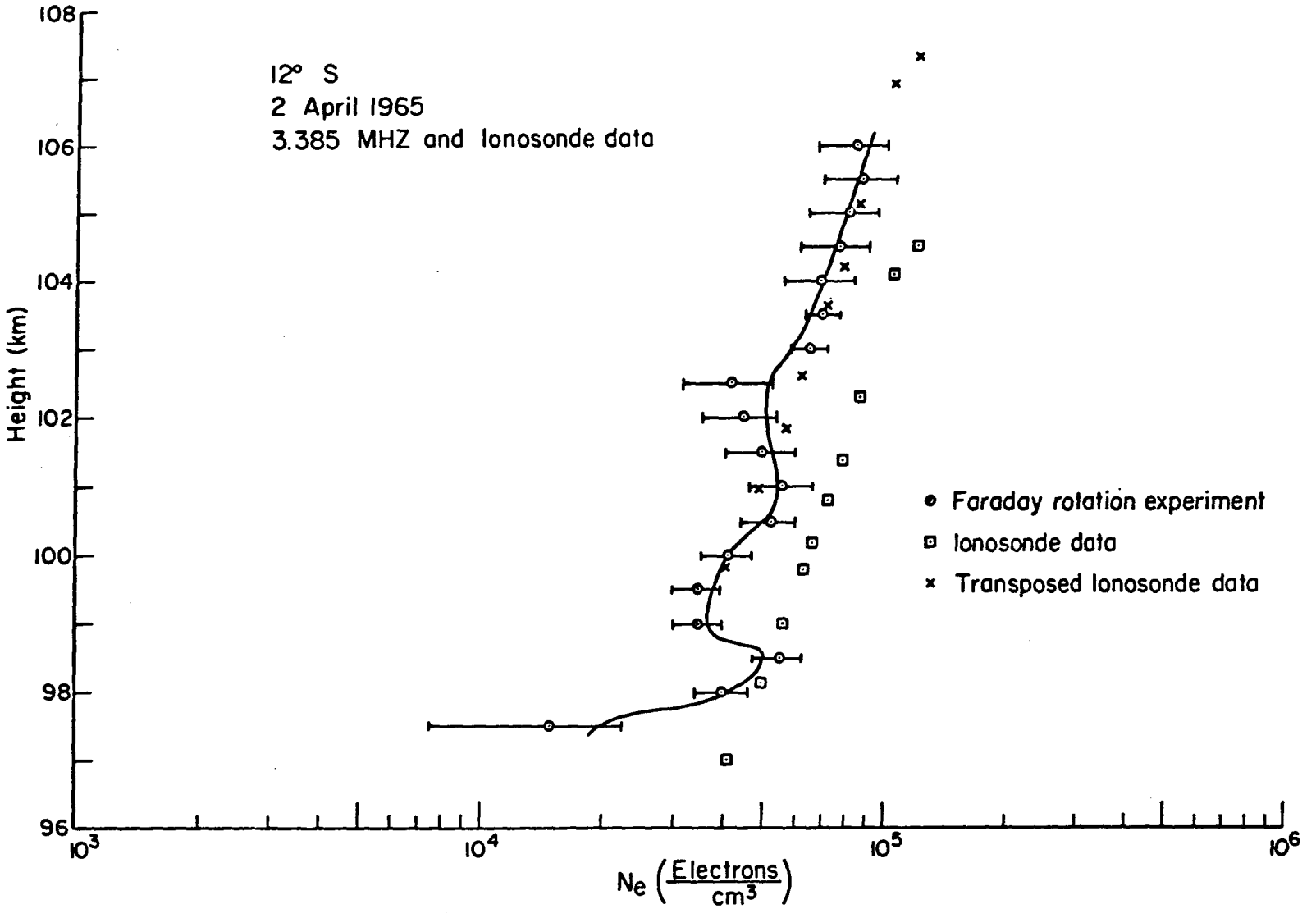
12° S
2 April 1965
3.385 MHZ and Ionosonde data
Height (km)
108
106
104
102
100
98
96
10^3
10^4
10^5
10^6
$N_e \left(\frac{\text{Electrons}}{cm^3}\right)$
Faraday rotation experiment
Ionosonde data
Transposed Ionosonde data

FIGURE 32

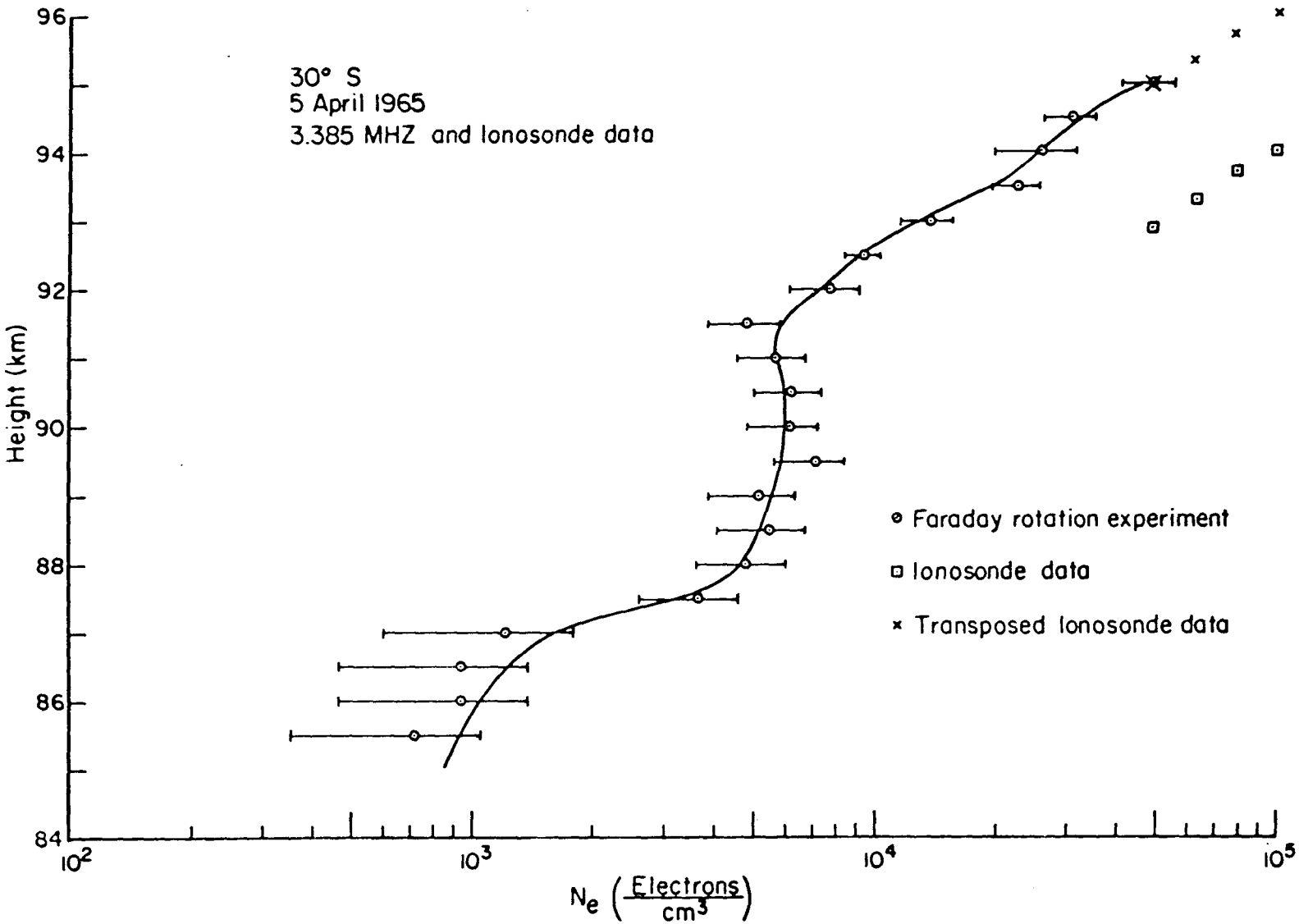
30° S
5 April 1965
3.385 MHZ and Ionosonde data
Height (km)
96
94
92
90
88
86
84
10^2
10^3
10^4
10^5
N_e (Electrons / cm^3)
Faraday rotation experiment
Ionosonde data
Transposed Ionosonde data

FIGURE 33

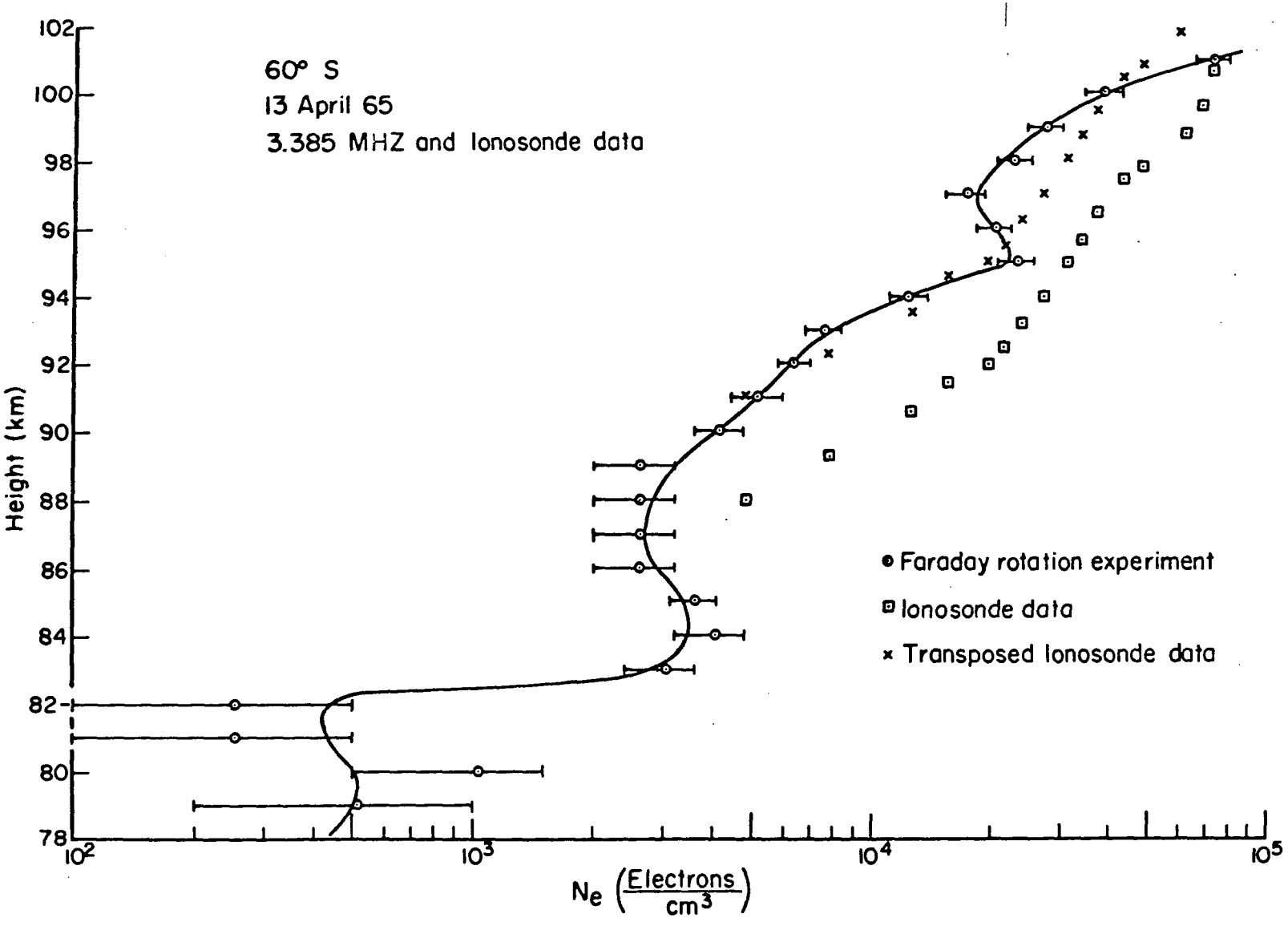
60° S
13 April 65
3.385 MHZ and Ionosonde data
Height (km)
102
100
98
96
94
92
90
88
86
84
82
80
78
10^2
10^3
10^4
10^5
N_e (Electrons / cm^3)
Faraday rotation experiment
Ionosonde data
Transposed Ionosonde data

FIGURE 34

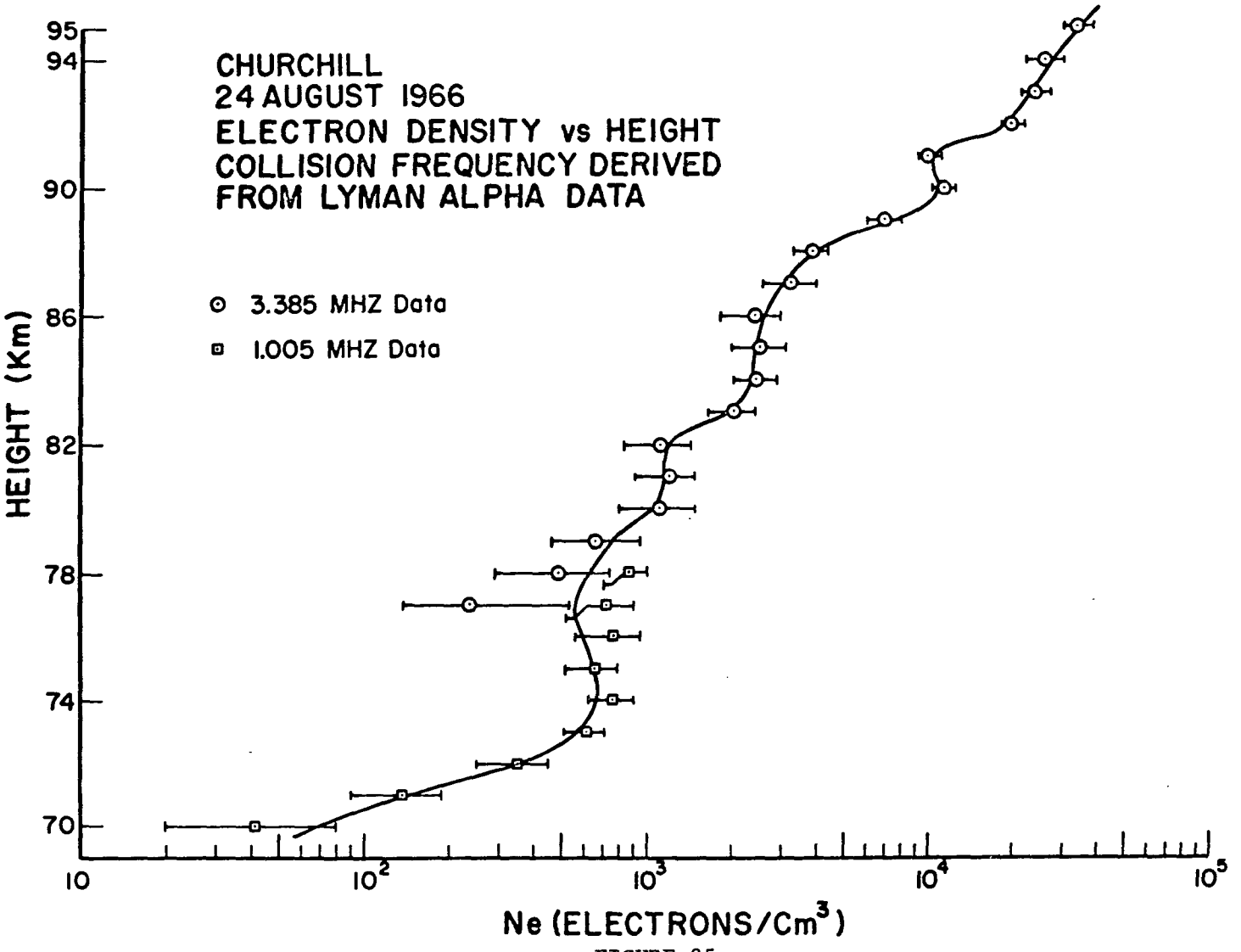
CHURCHILL
24 AUGUST 1966
ELECTRON DENSITY vs HEIGHT
COLLISION FREQUENCY DERIVED
FROM LYMAN ALPHA DATA
3.385 MHZ Data
1.005 MHZ Data
HEIGHT (Km)
95
94
90
86
82
78
74
70
10
10^2
10^3
10^4
10^5
Ne (ELECTRONS/Cm^3)

FIGURE 35

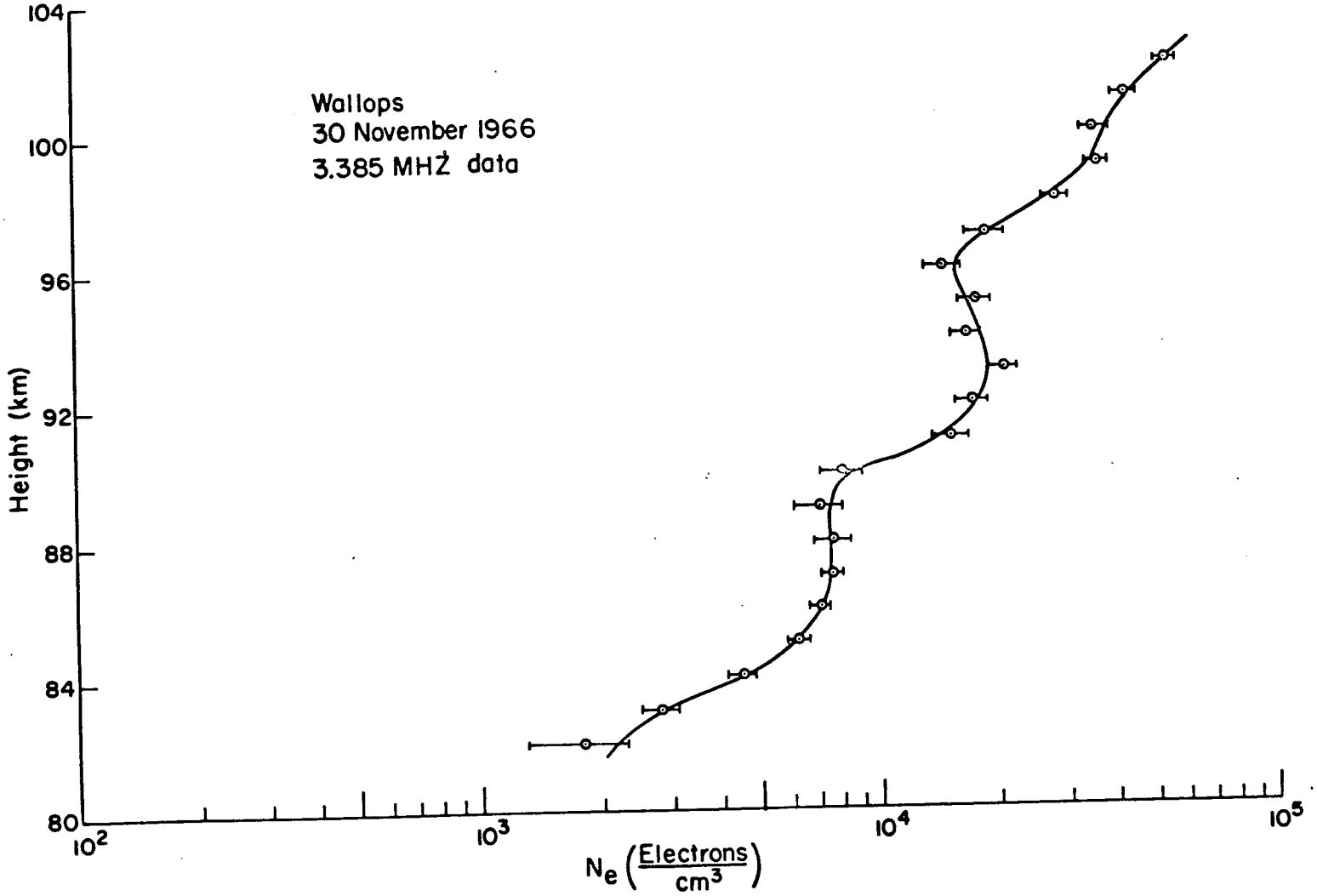
Wallops
30 November 1966
3.385 MHZ data
Height (km)
104
100
96
92
88
84
80
10^2
10^3
10^4
10^5
$N_e \left(\frac{\text{Electrons}}{cm^3}\right)$

FIGURE 36

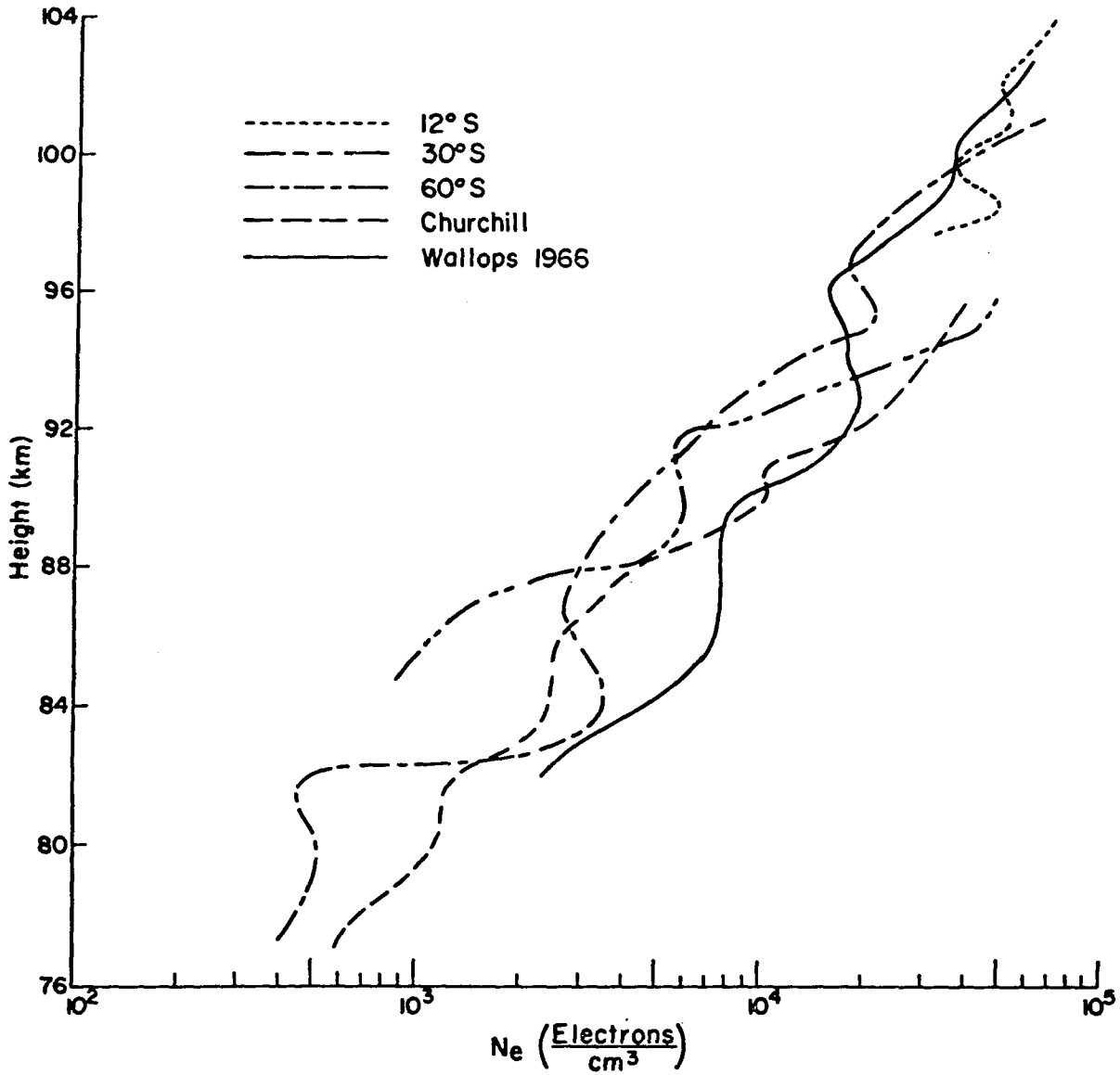
12° S
30° S
60° S
Churchill
Wallops 1966
Height (km)
104
100
96
92
88
84
80
76
10^2
10^3
10^4
10^5
Ne $\left(\frac{\text{Electrons}}{\text{cm}^3}\right)$

FIGURE 37

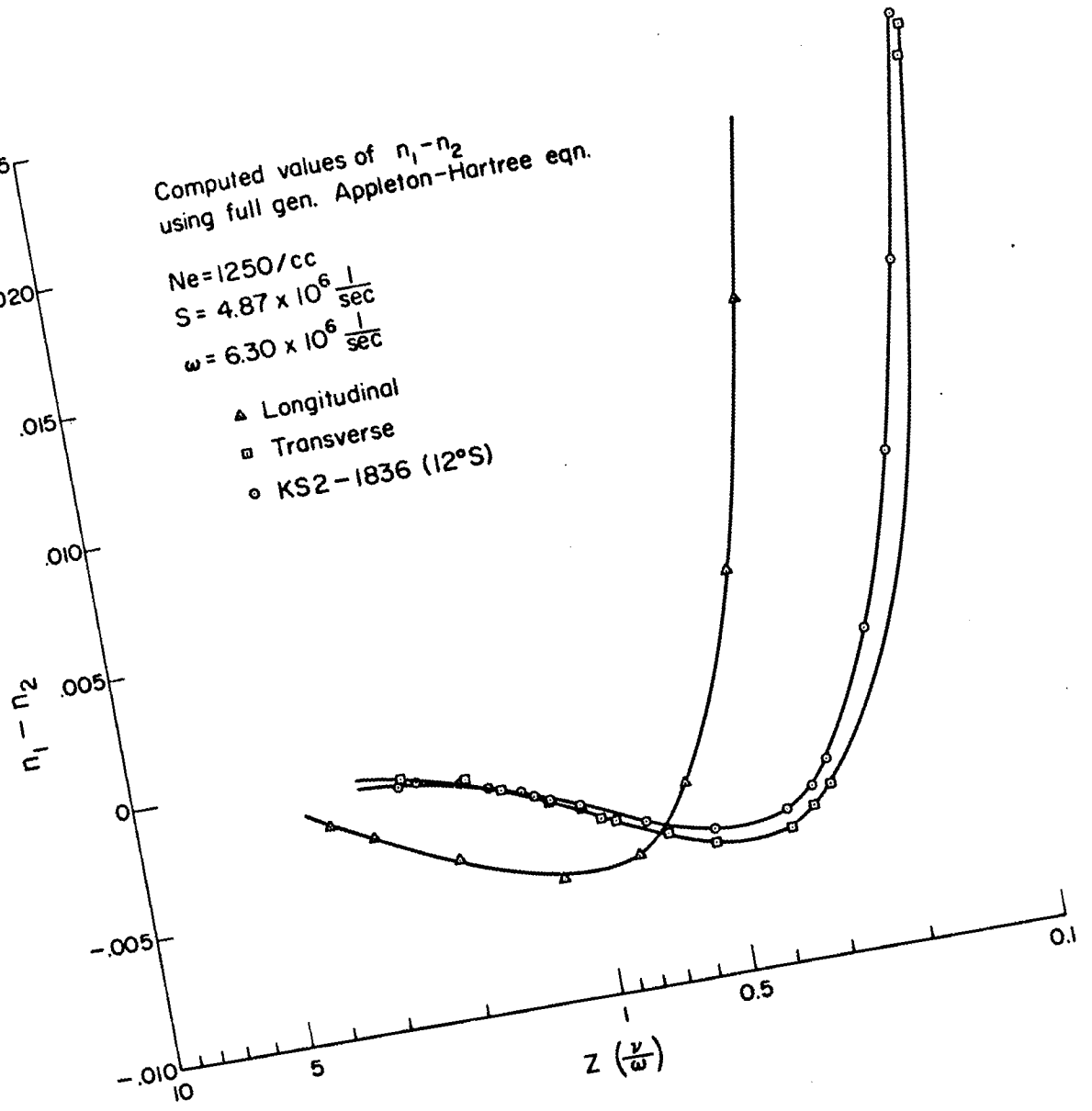
Computed values of $n_1 - n_2$
using full gen. Appleton-Hartree eqn.
Ne=1250/cc
S = 4.87 x 10^6 1/sec
ω = 6.30 x 10^6 1/sec
▲ Longitudinal
▫ Transverse
○ KS2-1836 (12°S)
.025
.020
.015
.010
.005
0
-.005
-.010
$n_1 - n_2$
10
5
1
0.5
0.1
Z (ν/ω)

FIGURE 38

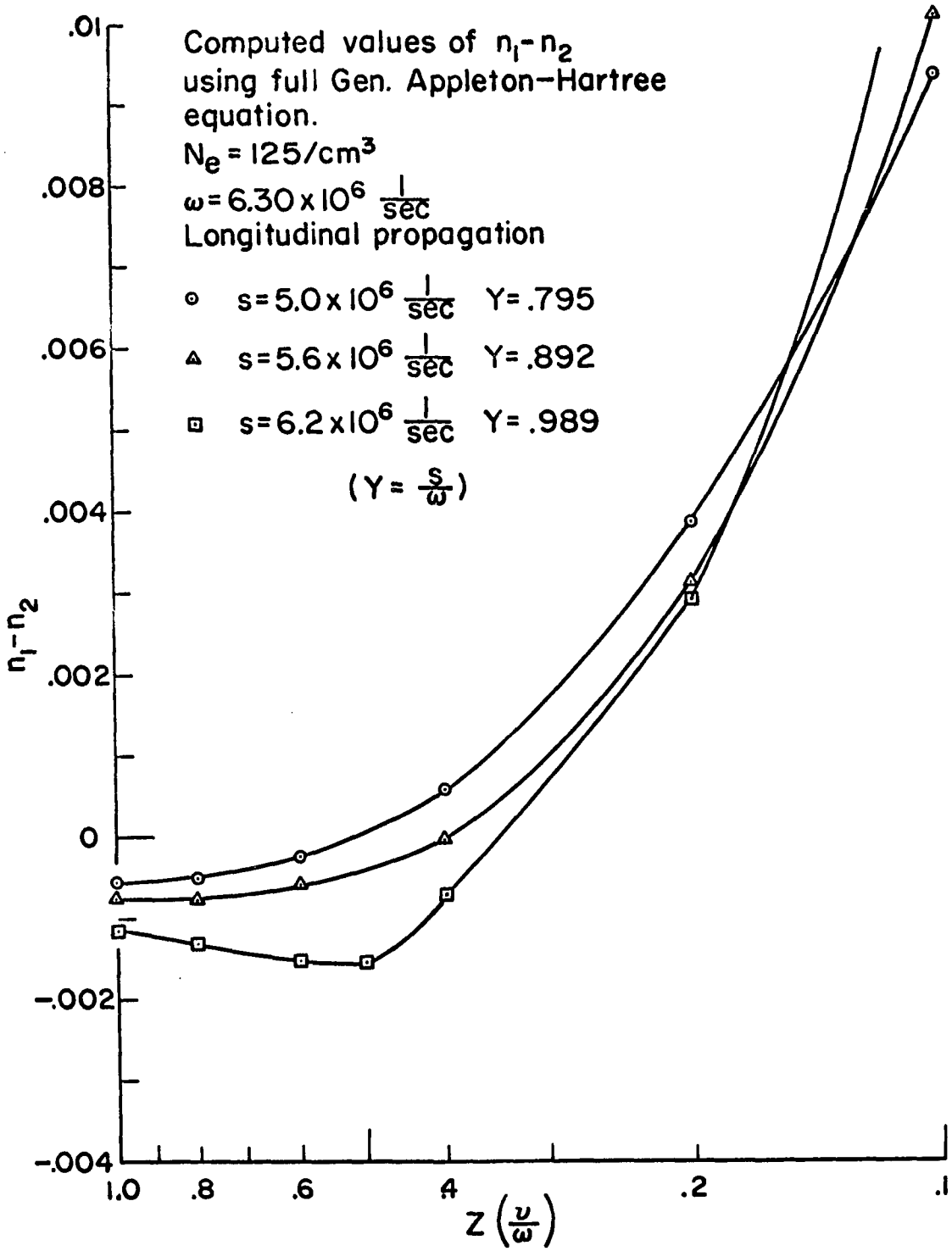
Computed values of $n_1 - n_2$
using full Gen. Appleton–Hartree
equation.
$N_e = 125/cm^3$
$\omega = 6.30 \times 10^6 \frac{1}{sec}$
Longitudinal propagation
$s = 5.0 \times 10^6 \frac{1}{sec}$ Y = .795
$s = 5.6 \times 10^6 \frac{1}{sec}$ Y = .892
$s = 6.2 \times 10^6 \frac{1}{sec}$ Y = .989
$(Y = \frac{s}{\omega})$
.01
.008
.006
.004
.002
0
-.002
-.004
$n_1 - n_2$
1.0
.8
.6
.4
.2
.1
$Z\left(\frac{\nu}{\omega}\right)$

FIGURE 39

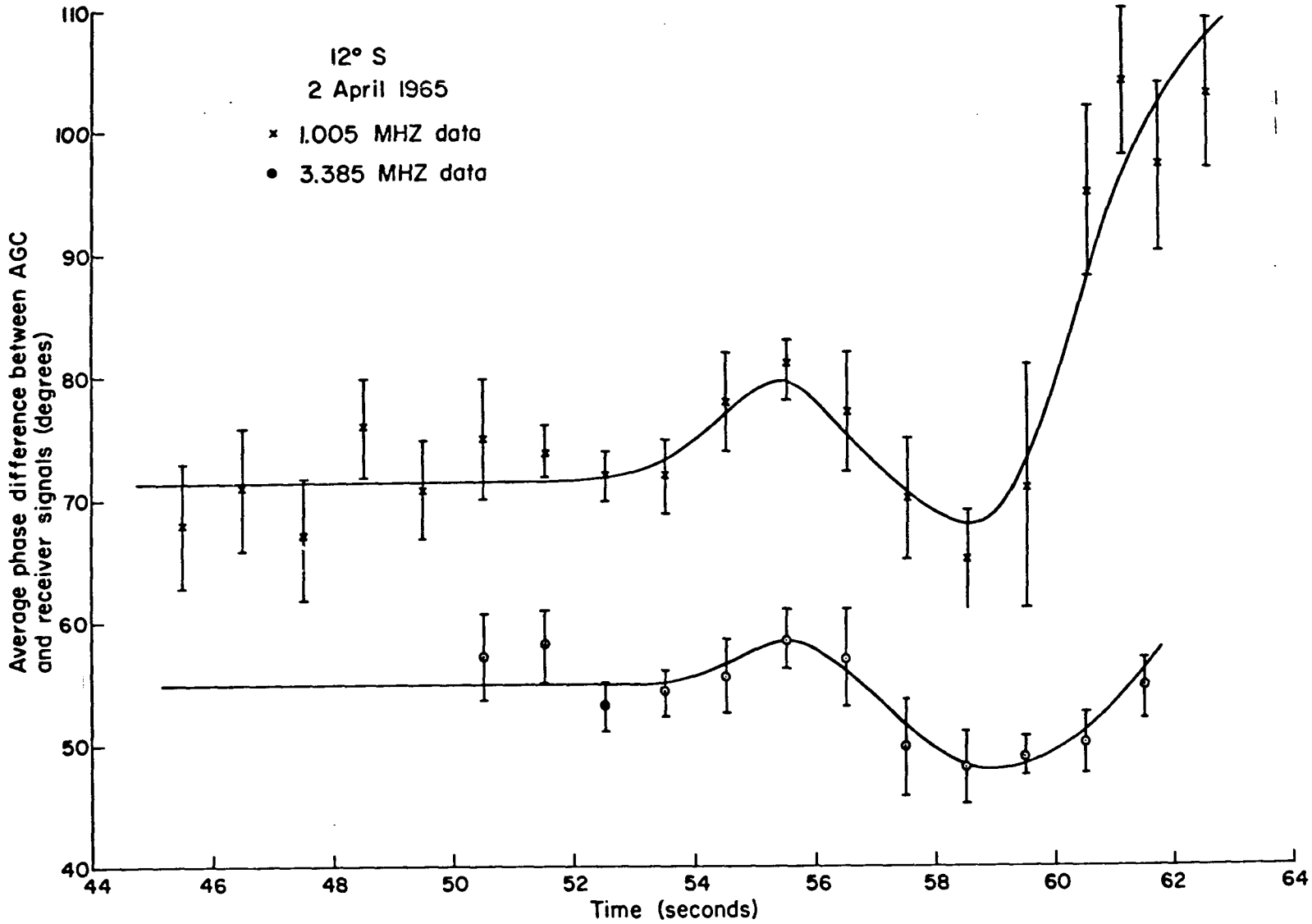
12° S
2 April 1965
× 1.005 MHZ data
• 3.385 MHZ data
Average phase difference between AGC and receiver signals (degrees)
110
100
90
80
70
60
50
40
44
46
48
50
52
54
56
58
60
62
64
Time (seconds)

FIGURE 40

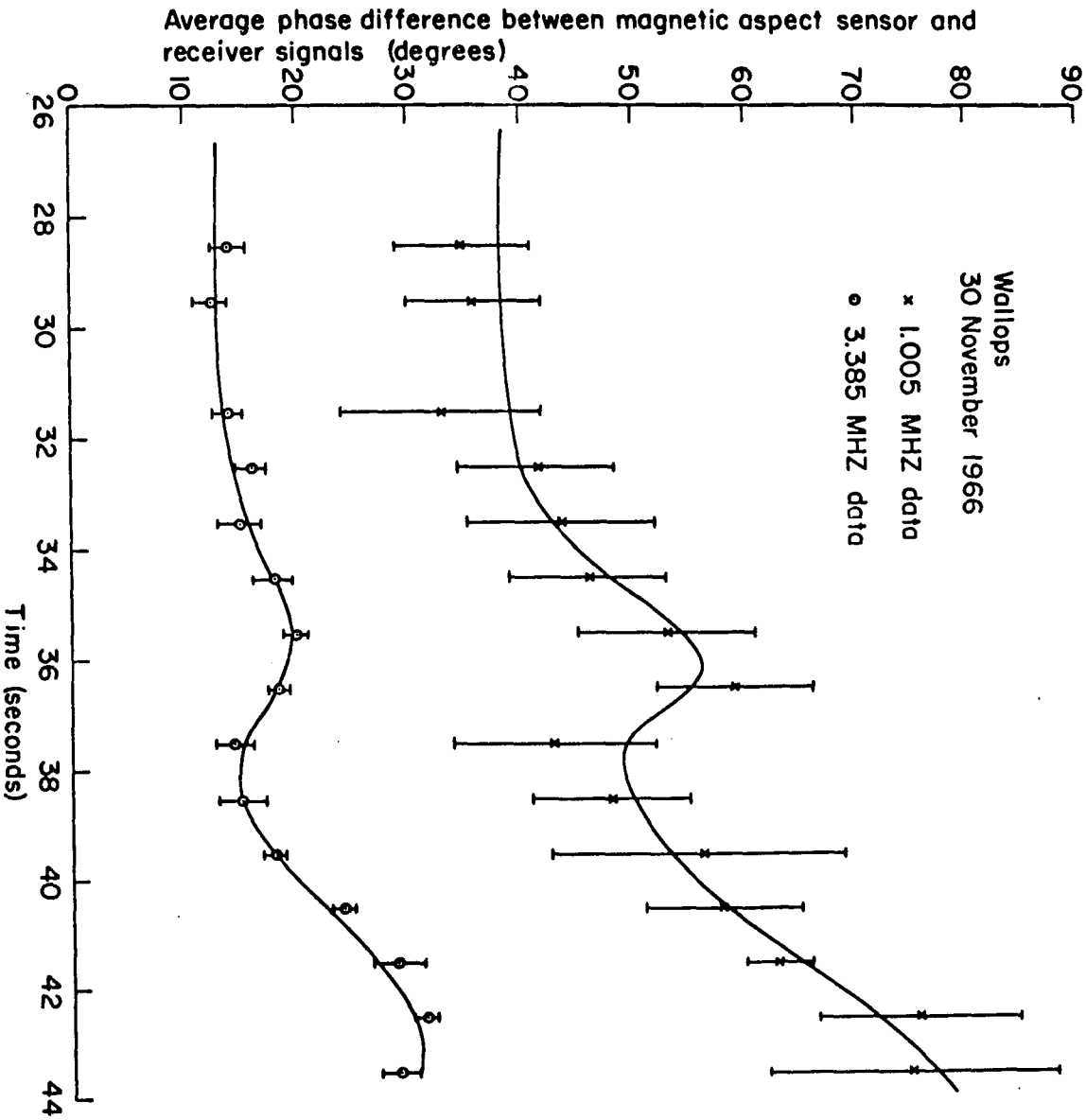
Average phase difference between magnetic aspect sensor and receiver signals (degrees)
0
10
20
30
40
50
60
70
80
90
26
28
30
32
34
36
38
40
42
44
Time (seconds)
Wallops
30 November 1966
× 1.005 MHZ data
• 3.385 MHZ data

FIGURE 41

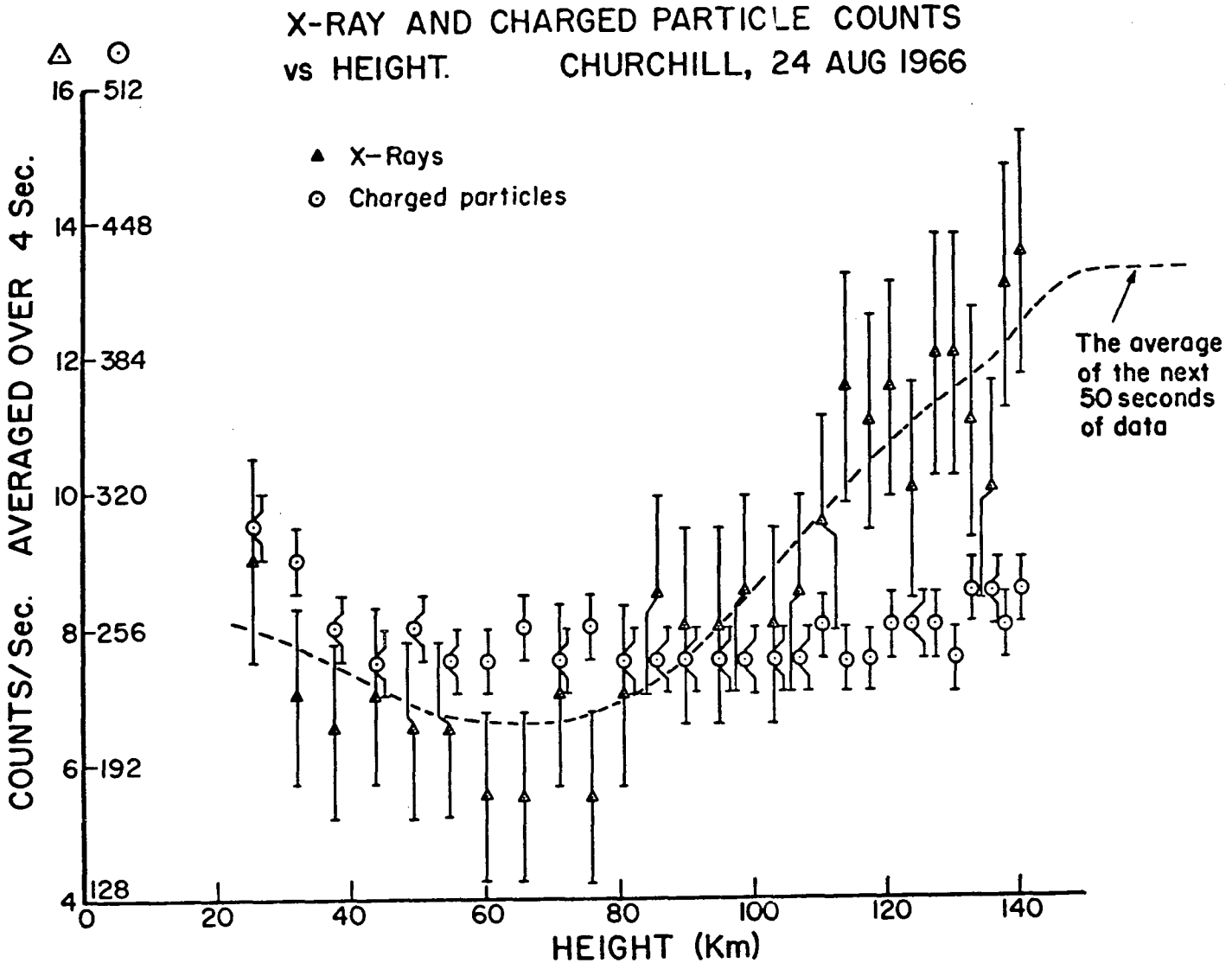
X-RAY AND CHARGED PARTICLE COUNTS
vs HEIGHT. CHURCHILL, 24 AUG 1966
▲ X-Rays
⊙ Charged particles
The average of the next 50 seconds of data
COUNTS/Sec. AVERAGED OVER 4 Sec.
△ ⊙
16 512
14 448
12 384
10 320
8 256
6 192
4 128
0 20 40 60 80 100 120 140
HEIGHT (Km)

FIGURE 42

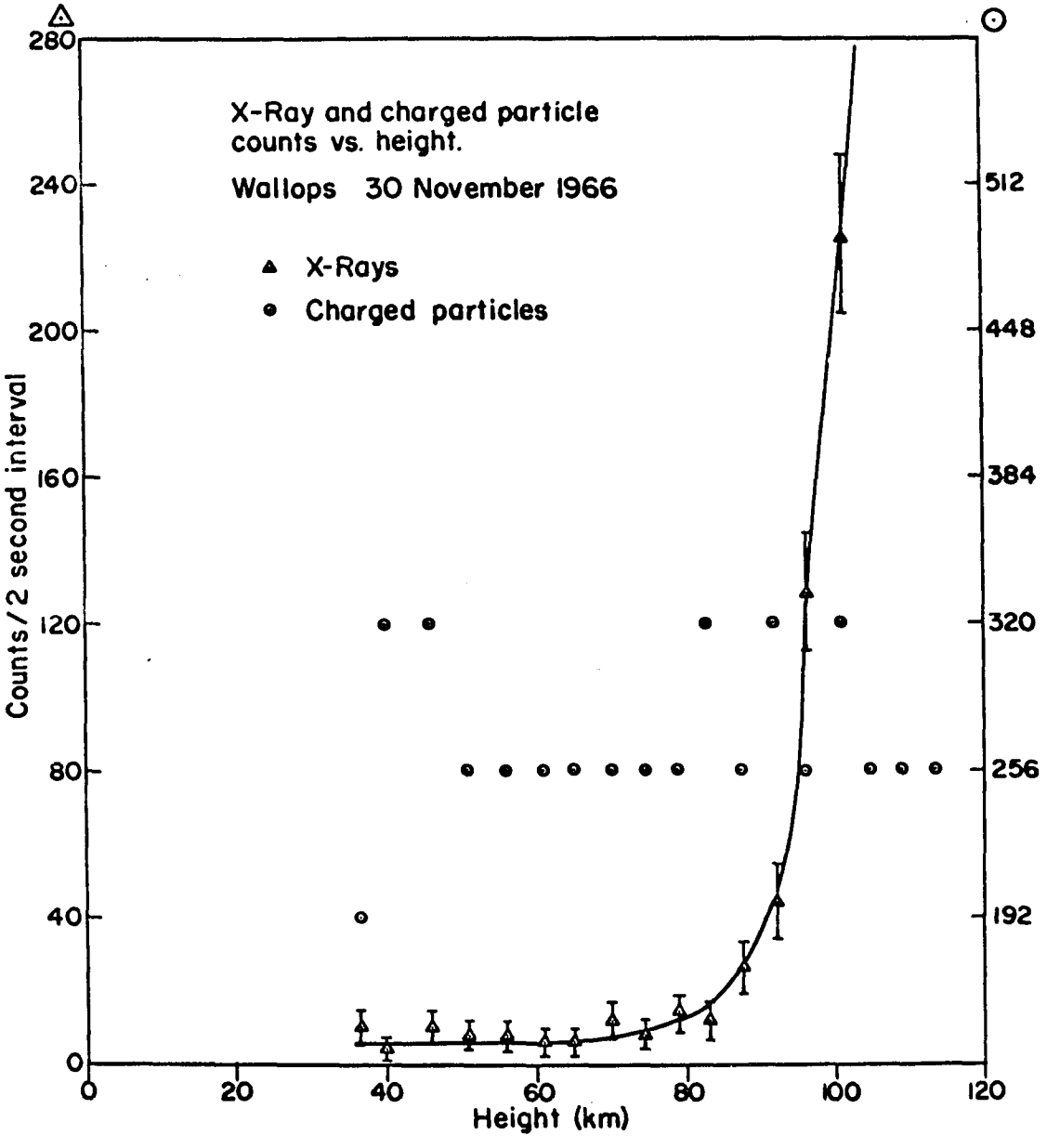
X-Ray and charged particle
counts vs. height.
Wallops 30 November 1966
X-Rays
Charged particles
Counts/2 second interval
Height (km)
0
40
80
120
160
200
240
280
192
256
320
384
448
512
0
20
40
60
80
100
120

FIGURE 43

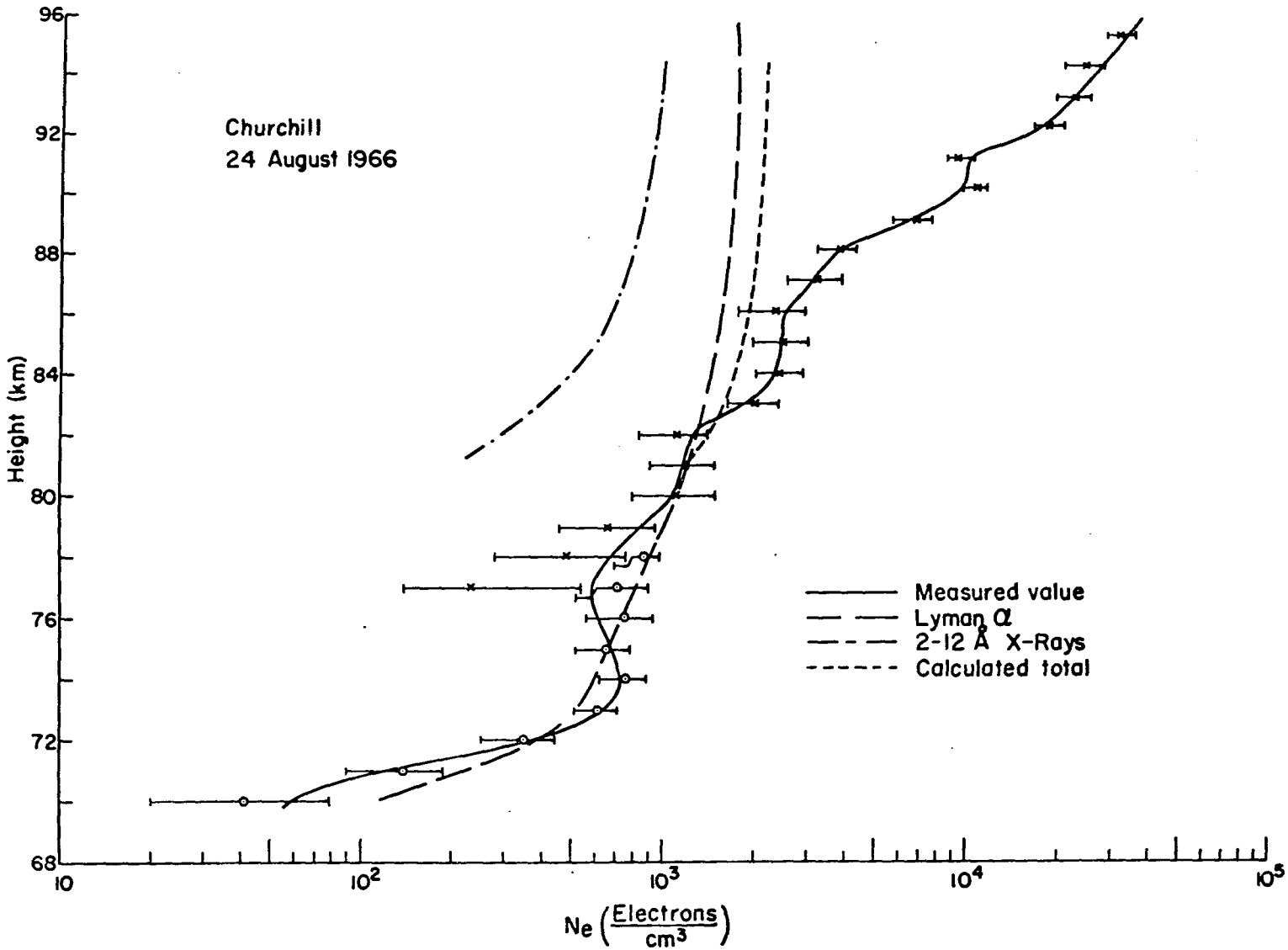
Churchill
24 August 1966
Height (km)
96
92
88
84
80
76
72
68
10
10^2
10^3
10^4
10^5
Ne $\left(\frac{\text{Electrons}}{\text{cm}^3}\right)$
Measured value
Lyman α
2-12 Å X-Rays
Calculated total

FIGURE 44

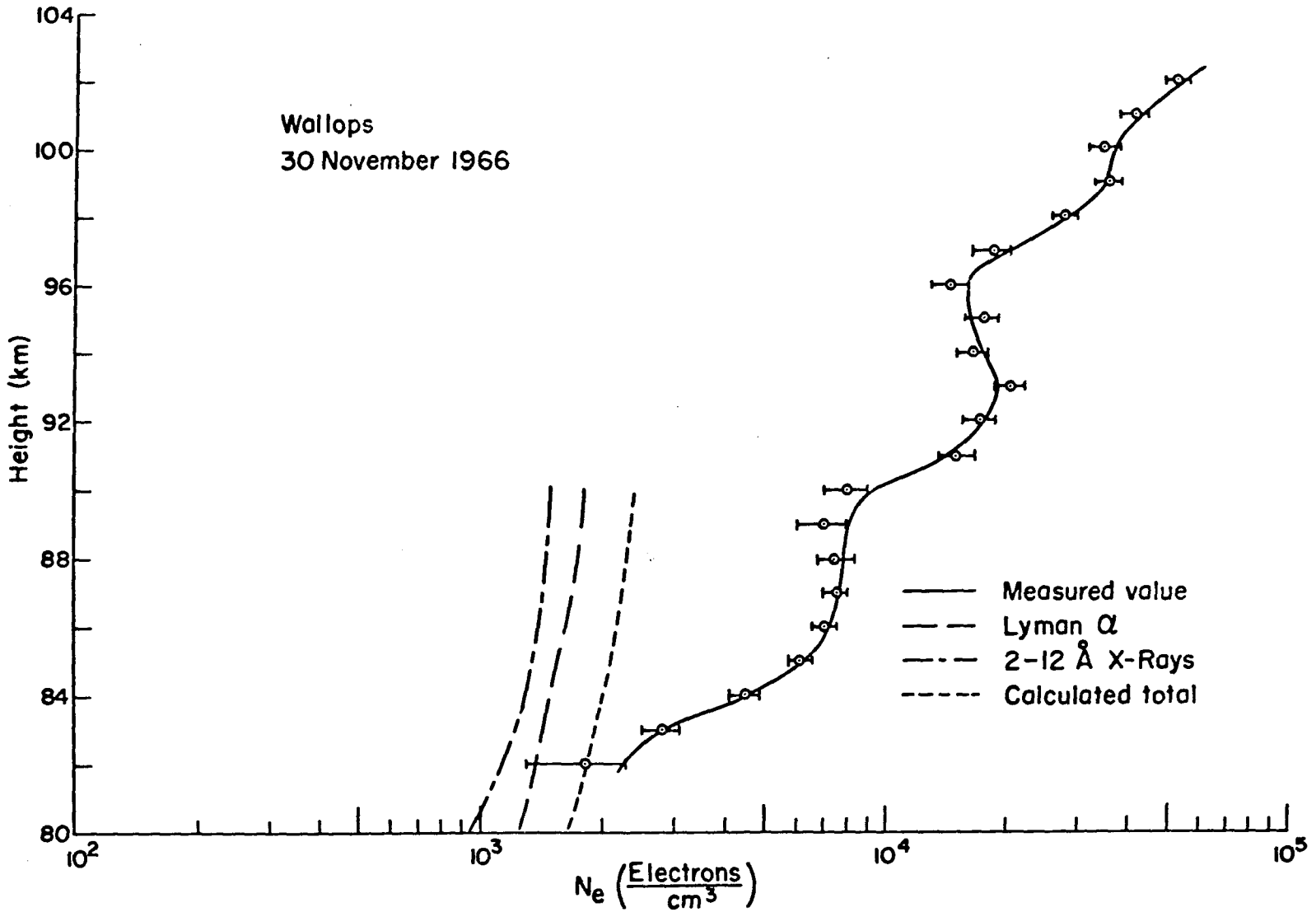
Wallops
30 November 1966
Height (km)
104
100
96
92
88
84
80
10^2
10^3
10^4
10^5
N_e (Electrons / cm^3)
Measured value
Lyman α
2-12 Å X-Rays
Calculated total

FIGURE 45

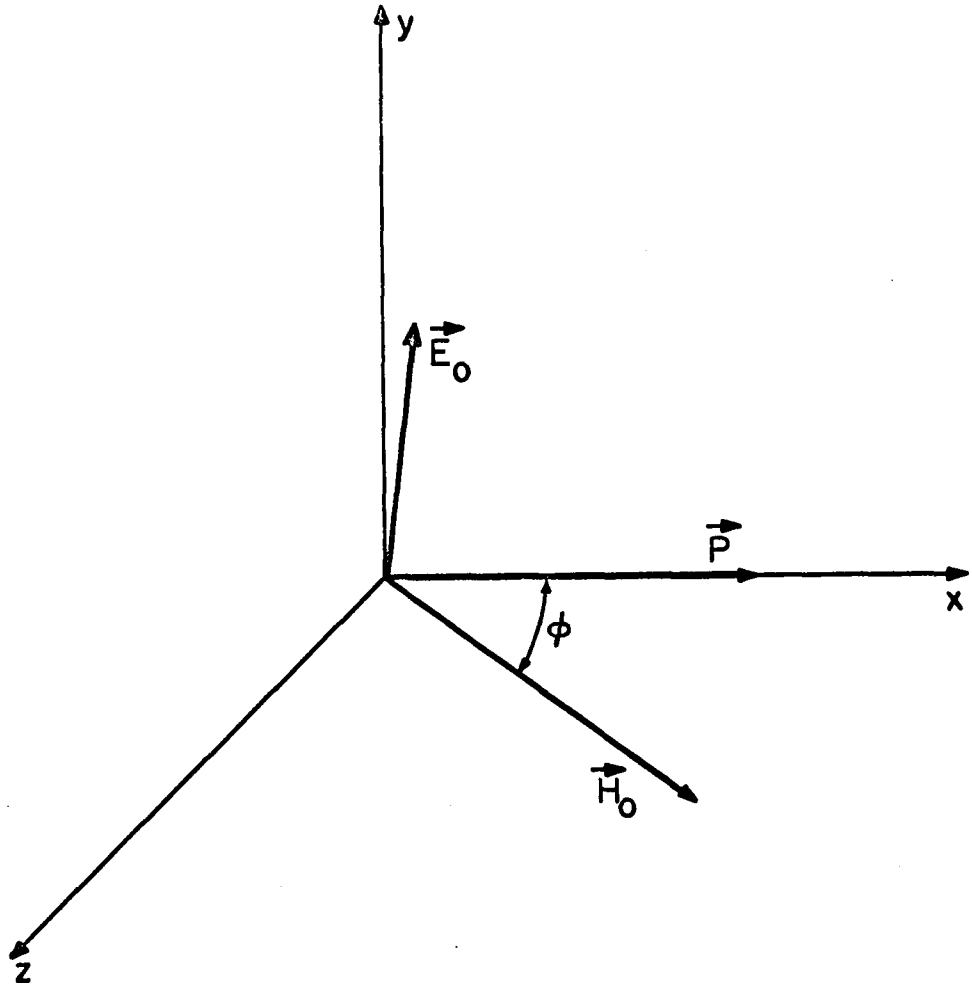

FIGURE 46